

This article is a companion to Addison et al. (2021), <https://doi.org/10.1029/2020JA029087>.

Key Points:

- Magnetic field-line draping partially protects Europa's upstream hemisphere from ion erosion, but causes substantial sputtering downstream
- If Europa's oxygen-bearing surface layer is thin compared to the ion penetration depth, maximum sputtering occurs near the upstream apex
- For a thick oxygen-bearing layer, two oxygen sputtering maxima form: one near the sub-solar point, and a weaker one near the upstream apex

Correspondence to:

P. Addison,
paddison6@gatech.edu

Citation:

Addison, P., Liuzzo, L., & Simon, S. (2022). Effect of the magnetospheric plasma interaction and solar illumination on ion sputtering of Europa's surface ice. *Journal of Geophysical Research: Space Physics*, 127, e2021JA030136. <https://doi.org/10.1029/2021JA030136>

Received 1 DEC 2021
Accepted 16 JAN 2022

Effect of the Magnetospheric Plasma Interaction and Solar Illumination on Ion Sputtering of Europa's Surface Ice

Peter Addison¹ , Lucas Liuzzo² , and Sven Simon¹ 

¹School of Earth and Atmospheric Sciences, Georgia Institute of Technology, Atlanta, GA, USA, ²Space Sciences Laboratory, University of California, Berkeley, CA, USA

Abstract For the entire ion energy range observed at Europa, we calculate spatially resolved maps of the surface sputtering rates of H₂O, O₂, and H₂ from impacts by magnetospheric ions. We use the perturbed electromagnetic fields from a hybrid model of Europa's plasma interaction, along with a particle-tracing tool, to calculate the trajectories of magnetospheric ions impinging onto the surface and their resultant sputtering yields. We examine how the distribution of the sputtering rates depends on the electromagnetic field perturbations, the angle between the solar radiation and the corotating plasma flow, and the thickness of the oxygen-bearing layer within Europa's surface. Our major findings are: (a) Magnetic field-line draping partially diverts the impinging ions around Europa, reducing the sputtering rates on the upstream hemisphere, but allowing for substantial sputtering from the downstream hemisphere. In contrast, zero sputtering occurs in much of the downstream hemisphere with uniform electromagnetic fields. (b) If the oxygen-bearing surface layer is thin compared to the penetration depth of magnetospheric ions, thermal ions dominate the O₂ sputtering rates, and the region of strongest sputtering is persistently located near the upstream apex. However, if the oxygen-bearing layer is thick compared to the penetration depth, energetic ions sputter the most O₂, and the location of maximum sputtering follows the sub-solar point as Europa orbits Jupiter. (c) The global production rate of O₂ from Europa's surface varies by a factor of 3 depending upon the Moon's orbital position, with the maximum particle release occurring when Europa's Sun-lit and upstream hemispheres coincide.

1. Introduction

The icy moon Europa (radius $R_E = 1,560.8$ km) is the smallest of the four Galilean moons of Jupiter, and possesses one of the youngest surfaces of any solar system object (about 50 million years, e.g., Bierhaus et al., 2009). The youth of Europa's surface is the result of continuous resurfacing processes, such as past tectonic activity (e.g., Kattenhorn & Hurford, 2009), meteorite impacts (e.g., Schenk et al., 2004), and sputtering by magnetospheric particles (e.g., Johnson et al., 2009). Neutral particles ejected from Europa's surface via sputtering form a dilute exosphere surrounding the Moon (e.g., Hall et al., 1995; Johnson et al., 2009; Plainaki et al., 2018). Radiolysis via charged particle impacts is also hypothesized to be the source of the non-uniform coloration and brightness patterns across the Moon's surface ice (Hendrix et al., 2011; McEwen, 1986). Europa's differentiated structure includes a subsurface liquid water ocean (Kivelson et al., 2000), which may interact with the surface through plume activity (Arnold et al., 2019; Jia et al., 2018; Paganini et al., 2020; Roth et al., 2014).

Europa's orbital distance of $9.4 R_J$ (Jupiter radius $R_J = 71,492$ km) places the Moon in the giant planet's inner magnetosphere. As such, it is exposed to a dynamic environment of strong electromagnetic fields and dense magnetospheric plasma. The 9.6° tilt between Jupiter's rotational and magnetic axes causes periodic variations in the strength and direction of the Jovian magnetic field as well as the plasma density at Europa's orbit (e.g., Bagenal & Dols, 2020; Kivelson et al., 1999; Seufert et al., 2011). This oscillation induces currents in Europa's conducting subsurface ocean, which in turn generate a secondary, quasi-dipolar magnetic field outside the Moon (Kivelson et al., 2000; Vance et al., 2021; Zimmer et al., 2000). Such an induction signal has been detected by the Galileo spacecraft during several targeted flybys of Europa (e.g., Kivelson et al., 2000).

Europa's location within the inner magnetosphere also portends that the Moon is exposed to a diverse range of plasma species. Neutral matter emitted by Europa's volcanically active neighbor, Io, is ionized via electron impacts and photoionization (Saur et al., 2003), and transported radially outward to Europa's orbit, forming a plasma sheet centered near the Jovian magnetic equator (e.g., Bagenal et al., 2016; Pensionerov et al., 2019). The thermal ion population in this sheet consists mainly of hydrogen, oxygen, and sulfur ions with energies of ~ 1 keV, and

follows a Maxwellian distribution (Bagenal & Delamere, 2011; Bagenal & Dols, 2020; Kim et al., 2020). Since Jupiter's rotation period is only one-eighth of Europa's orbital period, the sub-Alfvénic, (partially) corotating plasma overtakes the Moon with a relative velocity of $\approx 100 \text{ km s}^{-1}$ (Kivelson et al., 2009). As the magnetospheric plasma impinges onto Europa, electrons ionize neutral gas in the exosphere, creating an ionosphere that envelops the Moon (Saur et al., 1998). The injection of slow-moving, newly generated ionospheric ions into the magnetospheric flow drains momentum from the upstream plasma, causing it to slow and accumulate above the Moon's upstream face. The magnetic field, which is frozen into the plasma, piles up in this region of enhanced plasma density and drapes around the Moon (e.g., Arnold, Liuzzo, & Simon, 2020; Rubin et al., 2015).

The ion population near Europa also features a high-energy component, containing ions with energies E from several keV to tens of MeV (e.g., Clark et al., 2020; Cooper et al., 2001; Mauk et al., 2004; Paranicas et al., 2009). The high energies of these ions allow them to travel along Jupiter's magnetic field lines all the way to the planet's poles, where they are mirrored back toward Europa's orbital plane. As such, energetic ions continually intercept the Moon's orbit. Europa does not possess a sufficiently dense gas envelope for collisions to protect its surface from ion irradiation (Coustenis et al., 2010; Shematovich et al., 2005). Most magnetospheric ions can penetrate directly to the surface without encountering an exospheric molecule, although recent studies by Huybrighs et al. (2020) and Addison et al. (2021) suggest that charge exchange with exospheric neutrals may partially shield the Moon's surface from low energy ($E \leq 200 \text{ keV}$) proton bombardment. However, charge exchange reactions produce energetic neutral atoms (ENAs), which may still impact and erode the surface. As such, Europa's surface ice is continually abraded by corotating thermal ions ($E \approx 1 \text{ keV}$), fast-moving energetic ions ($5 \text{ keV} < E < 10 \text{ MeV}$), and (to a minor extent) ENAs. Slow-moving ionospheric ions weather the surface, however their contribution to erosion is several orders of magnitude weaker than that of magnetospheric ions (Saur et al., 1998). The surface also faces irradiation by galactic cosmic rays, but their influx is dwarfed by magnetospheric ions in the upper reaches of the ice (first \sim tens of centimeters, Nordheim et al., 2019), the realm typically sampled by optical instruments. In addition, thermal and energetic electrons contribute to surface modification (e.g., Davis et al., 2021; Vorbürger & Würz, 2018). However, this study focuses on the irradiation of the surface by magnetospheric ions only.

Magnetospheric ion irradiation has been identified as a critical agent in the weathering of Europa's surface (Addison et al., 2021; Breer et al., 2019; Cassidy et al., 2013; Dalton et al., 2013). The photopolarimeter-radiometer (PPR) aboard Galileo observed the upstream/orbital trailing hemisphere of Europa to be noticeably dark, with a bolometric albedo roughly 30% lower than that of the downstream hemisphere (Rathbun et al., 2010). Several studies have hypothesized that this hemispheric darkening is due to the presence of sulfur-containing compounds, which are formed when magnetospheric sulfur ions implant into surface ice (Dalton et al., 2013; Hendrix et al., 2011; McEwen, 1986). Measurements by the Galileo Near-Infrared Mapping Spectrometer (NIMS) also indicate a "bullseye" distribution of the sulfuric acid concentration on the surface, that is, the sulfuric acid concentration maximizes near the upstream apex, and decreases with distance away from it (Carlson et al., 2005). Such a bullseye-like pattern is consistent with the spatial distribution of sulfur ion flux predicted by some models (Cassidy et al., 2013; Dalton et al., 2013), reinforcing the idea that ion influx is the mechanism behind surface darkening.

Magnetospheric ions that impact Europa's surface may directly eject H_2O from the ice, or radiolytically dissociate H_2O into H_2 , O_2 , and a number of other trace species, which can then be ejected by further particle impacts (Plainaki et al., 2013; Teolis et al., 2017; Vorbürger & Würz, 2018). The Jeans parameter, that is, the ratio between a particle's gravitational potential energy and its kinetic energy, is 0.25 for sputtered H_2 (Roth et al., 2017), while for sputtered O_2 and H_2O it is ~ 10 (Saur et al., 1998). Therefore, O_2 and H_2O remain gravitationally bound to Europa, while a large fraction of the sputtered H_2 molecules are transported outward and escape Europa's Hill sphere, populating the neutral torus along Europa's orbit (see, e.g., Kollmann et al., 2016; Lagg et al., 2003). This escaping hydrogen has been detected by both the Hubble Space Telescope (HST) in the form of a global H_2 corona (Roth et al., 2017) and by the Galileo energetic particles detector (EPD, see Nénon & André, 2019). Since both O_2 and H_2O remain gravitationally bound to Europa, molecules of both types may re-encounter Europa's surface. The sticking coefficient (the likelihood that a molecule will re-freeze to Europa's surface upon contact) of H_2O is ~ 1 , while for O_2 it is $\sim 10^{-3}$ (Eviatar et al., 1985). Refreezing therefore removes much of the sputtered H_2O from the exosphere, but does not constitute a significant loss mechanism for O_2 . Despite this, a persistent, highly localized H_2O exosphere has recently been detected above Europa's upstream apex (Roth, 2021), suggesting that

H₂O is not entirely lost to refreezing. Molecular oxygen is removed from the exosphere mainly through ionization, with a minor contribution from plasma-neutral collisions that eject molecules (Saur et al., 1998). These two loss processes, along with O₂ production via ion impacts and radiolysis, allow O₂ to maintain mass balance within a near-surface exosphere ~300 km in height (e.g., Vorburger & Wurz, 2018). Sputtering of neutral ice particles is therefore the main source of Europa's predominantly O₂ exosphere (Plainaki et al., 2013; Teolis et al., 2017), with an additional, minor contribution from sublimation.

The amount of neutral matter produced per area and time via ion sputtering at a given surface location is dependent upon two factors: the differential ion surface flux $j(E, \theta)$ reaching that location, that is, how many ions of a specific energy E and incidence angle θ hit a given surface area per unit time, and the sputtering yield $Y(E, \theta, T)$, that is, how many neutral particles are released from a surface element of temperature T by each impinging ion. The total sputtering rate of a given ion species, R , is the number of surface particles ejected at that location per unit area per unit time. The sputtering rate is determined by multiplying the differential ion flux $j(E, \theta)$ with the sputtering yield $Y(E, \theta, T)$ at each incident ion energy and impact angle, and integrating over the entire energy range and all impact angles. In Sections 1.1 and 1.2, the current state of knowledge on the ion surface fluxes at Europa and sputtering yields is discussed.

1.1. Ion Surface Fluxes

The spatial distribution of the ion flux incident on Europa's surface has been investigated by a number of previous studies. Pospieszalska and Johnson (1989) modeled the trajectories of 30–140 keV sulfur ions near Europa and found that the surface flux of these ions maximizes near the Moon's orbital trailing (upstream to the plasma flow) apex. These authors also found that sulfur ions at higher energies ($E \geq 140$ keV), which possess a gyroradius of roughly $0.25 R_E$, can reach almost all locations on Europa's surface. Therefore, even the Moon's downstream hemisphere is not entirely protected from ion irradiation at energies above ~100 keV. Cassidy et al. (2013) calculated the surface fluxes of hydrogen, oxygen, and sulfur ions from 1 keV to 10 MeV, thereby covering the energy range where Galileo detected significant ion fluxes outside of Europa's interaction region (e.g., Paranicas et al., 2009). Cassidy et al. (2013) found that the total ion flux onto Europa (taking into account all species and energies) is distributed in a bullseye-like pattern centered at the trailing hemisphere apex, consistent with the distribution of surface sulfuric acid concentration measured by the NIMS instrument (Carlson et al., 2005). Ions with energies above 100 keV were found to impact primarily Europa's polar regions, a result of high field-aligned (i.e., north-south) velocities relative to the corotation velocity. However, both Pospieszalska and Johnson (1989) and Cassidy et al. (2013) treated the electromagnetic fields near Europa as uniform, that is, the perturbations to the fields introduced by the induced dipole and the sub-Alfvénic plasma interaction were not taken into account. We note that the presence of the induced field was not known at the time of the Pospieszalska and Johnson (1989) study.

All eight targeted flybys of Europa performed by the Galileo spacecraft showed perturbations to the local magnetic field components of up to 100% of their background values (see review by Kivelson et al., 2009). Magnetometer data from several flybys (most notably E4 and E11) even revealed a local reversal in the sign of the horizontal (i.e., parallel to Europa's orbital plane) field components compared to their measured upstream values. Investigations of induction at Europa (e.g., Vance et al., 2021; Zimmer et al., 2000) have shown that the induced field alone may reach a strength near the Moon's surface of approximately half (≈ 210 nT) of the Jovian background field (≈ 400 – 450 nT). Numerous modeling studies (e.g., Arnold et al., 2019; Arnold, Liuzzo, & Simon, 2020; Harris et al., 2021; Rubin et al., 2015) have reproduced the observed magnetic signatures by simulating the interaction between the upstream magnetospheric plasma, Europa's exosphere, and the Moon's induced field. The draping and pileup of the magnetospheric field, as well as the non-linear coupling of the induced field to the sub-Alfvénic interaction (Neubauer, 1999), significantly modify ion trajectories in Europa's vicinity (Addison et al., 2021; Breer et al., 2019). Accurate modeling of the ion fluxes incident upon Europa's surface therefore requires inclusion of the field perturbations generated by the plasma interaction with Europa's exosphere and induced field.

Several recent studies have modeled the spatial distribution ion flux onto Europa while including the deformation of the local electromagnetic fields by magnetospheric plasma deflection and induction. Breer et al. (2019) used the AIKEF hybrid model (kinetic ions and fluid electrons) to compute the perturbations to the electromagnetic fields near Europa. They then calculated spatially resolved maps of the accessibility—defined as the percentage of upstream ions that reach a given surface location—of Europa's surface to upstream magnetospheric ions. On

the basis of Galileo measurements of the ion species and energies present near Europa, these authors traced H^+ , O^{2+} , and S^{3+} ions at discrete energies ranging from 1 keV to 5 MeV. To establish a “baseline” for the identification of modifications in the accessibility patterns caused by the field perturbations, they also calculated maps of the ion irradiation of Europa’s surface for uniform fields (similar to Cassidy et al., 2013; Pospieszalska & Johnson, 1989). For the case of uniform fields, Breer et al. (2019) showed that Europa’s surface is highly accessible to upstream ions of all energies, with accessibilities near 90% in all regions except for a narrow “belt” near the Moon’s equator, where the accessibility drops to 0%–40% for ion energies below 1 MeV. This equatorial depletion belt results from the tendency of ions following magnetic field lines near Europa to gyrate into the Moon’s surface at high northern and southern latitudes before reaching the equatorial region. At millielectron-volt energies, even the protection of Europa’s equatorial region from magnetospheric ions was found to largely disappear, since millielectron-volt ions possess gyroradii of roughly $1 R_E$, and can therefore gyrate around Europa and impact any point on the surface.

However, Breer et al. (2019) also found that the draping and pileup of the magnetic field near Europa deflect a significant portion of the impinging ions around the Moon, reducing the accessibility by up nearly a factor of 2 at almost all surface locations. At ion energies below 100 keV, only several small “islands,” located mainly on the anti-Jovian hemisphere, were found to remain accessible to more than 80% of upstream ions. Only at millielectron-volt energies does the pattern of surface accessibility become qualitatively similar to that produced with uniform electromagnetic fields, although the accessibility was still five times smaller. Even the inclusion of the induced dipole field alone was found to make the surface accessibilities five to 10 times smaller at most energies. Thus, Breer et al. (2019) found the perturbations to the electromagnetic fields near Europa to be critical in modifying ion dynamics near the Moon at all energies. Therefore, the plasma interaction must be taken into account by any reasonable model of ion surface fluxes.

A synodic rotation period of Jupiter at Europa is ~ 10 hr, and on this time scale both the Jovian magnetic equator and the magnetospheric plasma sheet continuously sweep over the Moon. Therefore, both the Jovian background field and the ambient plasma density near Europa periodically vary. Not only does this variation affect the strength and orientation of the Moon’s induced secondary field, but it also continually changes the Alfvénic Mach number M_A of the upstream flow, altering the tilt of the Alfvén wings and the strength of the plasma interaction (Neubauer, 1980, 1998). This oscillation results in drastically different magnitudes and spatial distributions of ion flux onto Europa’s surface at different locations along a synodic rotation, as magnetospheric ions navigate starkly different electromagnetic field configurations. Breer et al. (2019) calculated the accessibility of Europa’s surface to magnetospheric ions for a few select sets of ambient electromagnetic field conditions, placing emphasis on the role of water vapor plumes in locally protecting the surface from ion irradiation. However, these authors did not systematically examine the evolution of these accessibility patterns as Jupiter completes a synodic rotation; only several “snapshots” along a rotation were investigated. Furthermore, their study did not quantify ion surface fluxes based on the energy-dependent upstream ion distributions measured by the Galileo spacecraft, but only the accessibility of Europa’s surface to upstream ions. In other words, the ion macroparticles—conglomerate particles, representative of many actual ions, but with the same mass-to-charge ratio—in the model of Breer et al. (2019) were all weighted equally, regardless of their energy. Their approach did not take into account that, for the energetic ion distributions measured near Europa by Galileo (Paranicas et al., 2009), modeled ion macroparticles at energies in the kiloelectron-volt regime represent *several orders of magnitude* more real-world particles than in the MeV regime. Converting surface accessibilities into realistic ion surface flux maps requires taking into account the dependence of the upstream ion distribution on ion energy and pitch angle, as observed by the Galileo EPD (Néron & André, 2019; Paranicas et al., 2002). The surface fluxes from such an approach may then be applied to inform studies of surface modification and sputtering.

Building upon the model of Breer et al. (2019) and Addison et al. (2021) recently constrained the magnitude and spatial distribution of ion surface flux at Europa for different sets of magnetospheric conditions encompassing an entire synodic rotation of Jupiter: namely when Europa is located at the center of the Jovian plasma sheet, as well as at maximum elongation north or south of the sheet. At each location, the AIKEF hybrid code was used to calculate the Moon’s perturbed electromagnetic environment. Addison et al. (2021) then combined a particle-tracing tool with the upstream energy and pitch angle distributions of the ions, as measured by Galileo, to calculate ion surface fluxes. Their model incorporated upstream plasma densities and temperatures derived from Galileo observations (Bagenal & Delamere, 2011; Kivelson et al., 2009; Paranicas et al., 2002), as well

as the latest information on energetic ion charge states obtained by the Juno spacecraft (Clark et al., 2020; Kim et al., 2020). By averaging the flux maps obtained for the three distances between Europa and the center of the Jovian plasma sheet, Addison et al. (2021) then obtained average surface flux maps of magnetospheric oxygen, sulfur and hydrogen ions over an entire synodic rotation. Their averaged flux maps consider contributions of ions from the entire energy range (5 keV up to 10 MeV) where significant ambient fluxes were observed near Europa.

The study of Addison et al. (2021) found that inclusion of the plasma interaction results in drastically different patterns of ion surface flux compared to the case of uniform electromagnetic fields. Although the total ion flux in their model still maximizes near the upstream apex, deflection of thermal ions around Europa's Alfvén wings was shown to reduce ion flux onto the upstream hemisphere by two orders of magnitude compared to predictions for uniform fields. Most surprisingly, the draped field geometry near the Moon was found to divert thermal ions from the “edges” of the Maxwellian distribution onto Europa's polar regions, as well as onto its *downstream* hemisphere, resulting in a flux there of only one order of magnitude less than in the upstream hemisphere. Using a fluid model and considering the forces generated by local pressure gradients, Harris et al. (2021) identified a similar flow pattern in the thermal ion population near Europa. In contrast to this, without plasma currents the thermal ion fluxes are zero in large segments of the downstream hemisphere.

Addison et al. (2021) showed the surface flux pattern of energetic ions ($E \geq 5$ keV) to be considerably modified by the plasma interaction. A large, quasi-elliptical depletion region was found to form around the upstream apex and extend approximately $\pm 60^\circ$ in both latitude and longitude. The field draping enhances the distance that an ion traveling along a magnetic field line is within one gyroradius of the Moon's surface. This mechanism causes a significant fraction of the incoming energetic ions to gyrate into the Moon's surface at high latitudes before they can reach the upstream apex, resulting in this elliptical depletion region. This “inverted bullseye” feature is not predicted by a model that treats the fields as uniform. The results of Addison et al. (2021) therefore show that the inclusion of the sub-Alfvénic plasma interaction is imperative to explain a number of observations from both in situ spacecraft and ground-based telescope observations, such as the non-uniform surface distribution of sulfuric acid concentrations (Ligier et al., 2016), and a drop in the upstream ion flux seen during several close Galileo flybys of Europa (Paranicas et al., 2000).

1.2. Sputtering Yields

Once a magnetospheric ion impacts Europa's surface, the amount of neutral matter ejected is determined by the ion's sputtering yield $Y(E, \theta, T)$. Many laboratory experiments have measured sputtering yields from water ice (see reviews by Johnson, 1996; Johnson et al., 2009 and references therein). Surface particles may be released from the ice at any depth to which an impinging ion penetrates ($\approx 10^1 - 10^7$ Å, e.g., Teolis et al., 2017). However, the greater the depth at which a neutral particle is ejected, the larger the chance that it will stick to another surface grain before escaping into the exosphere (Cassidy & Johnson, 2005).

For projectile ion energies below ~ 100 keV, molecules are directly ejected from the surface ice via momentum transfer (elastic) collisions (Sigmund, 1969). At higher projectile energies, incident ions excite electrons in surface molecules, breaking covalent bonds and causing the dissociation of constituent species, thereby facilitating neutral matter release from the surface (Brown et al., 1978; Sieger et al., 1998). Laboratory data has shown that sputtering yields from water ice increase with energy in the momentum-transfer regime, then rapidly grow in the electronic excitation regime, before dropping off at extremely high projectile energies (Johnson et al., 2009). The sputtering yields of the dominant ion species at Europa (hydrogen, oxygen, and sulfur ions) therefore reach a maximum in the $E \approx 100$ keV–5 MeV range (depending upon the projectile species), and then drop precipitously at higher energies. This non-monotonic energy dependence of the sputtering yield seen in laboratory experiments has been fit with analytical forms by, for example, Famá et al. (2008). Their fits have shown that, due to their large masses and atomic numbers, oxygen and sulfur ions possess the greatest sputtering yields: up to 5,000 neutral particles are released per incident projectile. The analysis of laboratory data by Famá et al. (2008) also revealed that ions which impact the surface at grazing angles $\theta \approx 90^\circ$ against the surface normal sputter up to 100 times more neutral particles than ions which impact normal to the surface ($\theta \approx 0^\circ$), since grazing projectiles deposit more energy at shallower depths.

In addition to projectile properties, sputtering yields also depend on the properties of the surface that is impacted. The porosity of Europa's surface regolith may limit sputtering yields to 25% of their values measured in the

laboratory using “smooth” surfaces, as particles that are initially ejected may hit and stick to other grains rather than escape into the exosphere (Cassidy & Johnson, 2005). Furthermore, sputtering yields increase monotonically with temperature (Brown et al., 1982) in the range of surface temperatures observed at Europa (≈ 60 – 140 K, Spencer et al., 1999). This temperature dependence mainly affects the sputtering yields of O_2 , which is radiolytically dissociated from ice within the first ≈ 28 Å of the surface (Teolis et al., 2005, 2017). Increased surface temperature facilitates the transformation of dissociated oxygen radicals into stable O_2 (Teolis et al., 2017), which may be sputtered by subsequent projectile impacts. The surface temperature profile at Europa is determined by its orientation with respect to the Sun, as well as the thermal inertia of its surface ice. Therefore, sputtering rates may vary over the course of an European rotation as the sub-solar point moves along the equator relative to the upstream apex, where the influx of magnetospheric ions peaks (Addison et al., 2021).

The effect of solar orientation relative to the plasma flow direction on sputtering rates at Europa has been studied by Plainaki et al. (2013), who modeled the generation of the exosphere at four different locations of the Moon relative to the Sun: with the sub-solar point located at the sub-Jovian, downstream, anti-Jovian, and upstream apices (0:00, 6:00, 12:00, and 18:00 local time [LT], respectively). These authors characterized the ion influx pattern with an analytical profile, which combined a spatially homogeneous component—representing an assumed isotropic influx of energetic ions—with a bullseye-like enhancement centered at the upstream apex and suggested to be representative of the thermal ion contribution. They then modeled the sputtering rates and subsequent exospheric dynamics for different orientations between the incoming solar radiation and the corotational plasma flow. Plainaki et al. (2013) found that the exospheric column density is greater by a factor of 3 when the sub-solar point and upstream apex are colocated, compared to when the sub-solar point is located at the downstream apex. These authors also suggested that the region where the largest amount of neutral matter is sputtered follows the sub-solar point as it moves across Europa’s surface, and does not remain fixed at the upstream apex. However, laboratory measurements indicate that O_2 sputtering from an icy surface has a delayed response to changes in surface temperature (Teolis et al., 2005) as surface radicals require time to accumulate into O_2 . Since this delay is potentially comparable to an European day, the sputtering rate of O_2 may not have time to adjust to changes in surface temperature following Europa’s orbital motion (Teolis et al., 2017).

In contrast to Plainaki et al. (2013)—who used an analytical profile to describe ion surface flux—the study of Cassidy et al. (2013) combined modeled ion surface fluxes, fits to laboratory data of sputtering yields, and a thermophysical surface temperature model (Spencer et al., 1989) to calculate the spatial distribution of ion sputtering rates at Europa. Adopting the notion of a delayed O_2 sputtering response to changes in surface temperature (Teolis et al., 2005), Cassidy et al. (2013) applied a diurnally averaged (i.e., averaged over a full orbit) profile of Europa’s surface temperature. These authors found that Europa’s surface is preferentially sputtered on the upstream hemisphere, with the neutral production in that region exceeding that of the downstream hemisphere by a factor of 3. Neutral particles ejected by thermal oxygen ions and energetic sulfur ions were found to dominate the sputtering rate. The strong contribution of the thermal oxygen ions in the model of Cassidy et al. (2013) arose from their high surface flux, which was found to exceed that of any other species by roughly an order of magnitude. We note that the modeled surface fluxes of Cassidy et al. (2013) are not consistent with those of Addison et al. (2021), who found that—when field line draping is taken into account—magnetospheric hydrogen (*not* oxygen) makes the largest contribution of any ion species to surface flux. The large contribution of energetic sulfur ions to the sputtering rate calculated by Cassidy et al. (2013) arose mainly from their respective sputtering yield, which is roughly a factor of 5 greater than that of oxygen in the energetic regime, and orders of magnitude greater than the sputtering yield of hydrogen at all energies. Cassidy et al. (2013) found that nearly zero O_2 is produced on the downstream hemisphere, since in their model O_2 is sputtered almost entirely by the thermal heavy ions. Under the assumption of uniform fields, these ions only precipitate onto the upstream hemisphere. Vorburger and Wurz (2018) utilized a spatially homogeneous magnetospheric ion flux across Europa’s surface in their calculation of sputtering rates, although they did approximate the deflection of thermal upstream ions in the perturbed fields near Europa by uniformly reducing their respective flux by a factor of 5. These authors confirmed that thermal oxygen and energetic sulfur ions are the most significant contributors to ion sputtering at Europa.

Although Plainaki et al. (2013), Cassidy et al. (2013), and Vorburger and Wurz (2018) have modeled neutral production via magnetospheric ion sputtering at Europa, no study to date has investigated how the spatial distribution of surface sputtering is modified when a realistic model of incident ion deflection in the draped electromagnetic fields is taken into account. The ion-tracing model of Cassidy et al. (2013) assumed the fields to be spatially

uniform, an assumption also implicit in the ion influx pattern utilized by Plainaki et al. (2013). Vorburger and Wurz (2018) treated the ion influx as uniform at all points on Europa's surface.

However, Addison et al. (2021) found not only that the shielding of Europa's upstream hemisphere from magnetospheric ion impacts due to field line draping is orders of magnitude stronger than assumed by Vorburger and Wurz (2018), but that it varies strongly with surface latitude and longitude. In addition, Addison et al. (2021) demonstrated that the downstream hemisphere of Europa receives only an order of magnitude less thermal ion flux than the upstream hemisphere. They also showed that, in draped fields, the influx of energetic ions *minimizes* near the upstream apex, exactly opposite to what is predicted for uniform fields. None of the available sputtering rate models take into account these important aspects of ion precipitation onto Europa. Therefore, ion sputtering rates at Europa must be reexamined with the influence of the field perturbations included.

This study is the first to model the sputtering of Europa's surface ice via magnetospheric ion impacts while incorporating a realistic picture of the field perturbations generated by the Moon's sub-Alfvénic plasma interaction. We use the AIKEF hybrid model (e.g., Arnold et al., 2019; Arnold, Liuzzo, & Simon, 2020; Arnold, Simon, & Liuzzo, 2020) to calculate the perturbations to Europa's local electromagnetic environment. The electromagnetic fields from AIKEF are combined with the GENTOO particle-tracing tool (e.g., Addison et al., 2021) to calculate the trajectories of magnetospheric ions in Europa's perturbed electromagnetic environment, from the thermal energy regime up to 10 MeV. We then use established fits to laboratory data of ion sputtering yields to obtain spatially resolved maps of ion sputtering rates across Europa's surface. We examine the influence of projectile species, energy, incidence angle, as well as the orientation of the Sun relative to the plasma flow direction and the electromagnetic field perturbations on surface sputtering rates.

A description of the AIKEF and GENTOO models, as well as all input parameters, is provided in Section 2. The modeled electromagnetic field configuration, as calculated by the AIKEF model, is presented in Section 3.1. The corresponding modeled ion surface fluxes from GENTOO along with our modeled H₂O sputtering rate maps for uniform and perturbed fields are presented in Section 3.2. In Section 3.3 we calculate maps of the O₂ and H₂ sputtering rates, while examining the role of Europa's orbital position and the thickness of the oxygen-bearing surface layer in modifying O₂ sputtering. This article concludes with a summary of our main findings in Section 4.

2. Model Description

We use a multifaceted approach in order to calculate maps of the magnetospheric ion sputtering rates at Europa. First, we model the perturbed electromagnetic environment near the Moon using the AIKEF hybrid code. The AIKEF model has been extensively applied to Europa in five preceding publications (Addison et al., 2021; Arnold et al., 2019; Arnold, Liuzzo, & Simon, 2020; Arnold, Simon, & Liuzzo, 2020; Breer et al., 2019), as well as the Jovian Moon Callisto (Liuzzo et al., 2015, 2016, 2017, 2018, 2019a, 2019b). In addition, AIKEF has been used to study plasma interactions at the terrestrial moon (Liuzzo, Poppe, et al., 2021; Wiehle et al., 2011), the Saturnian Moons Titan (e.g., Feyerabend et al., 2015, 2016; Regoli et al., 2016), Tethys (Simon et al., 2009), Rhea (Simon et al., 2012), and Dione (Krupp et al., 2020), as well as Neptune's Moon Triton (Liuzzo, Paty, et al., 2021; Simon et al., 2022).

Second, we calculate the spatial distribution of ion flux onto Europa's surface with the GENTOO particle tracing code, which solves the equations of motion for ions moving through the draped fields near Europa. GENTOO has been applied to Europa in two preceding studies (Addison et al., 2021; Breer et al., 2019), as well as to Callisto (Liuzzo et al., 2019a, 2019b), and Ganymede (Liuzzo et al., 2020). Finally, we combine our modeled ion surface flux patterns with empirical models of the sputtering yields from water ice (Famá et al., 2008; Johnson et al., 2004; Teolis et al., 2017), along with a thermophysical model for Europa's surface temperature profile (Spencer et al., 1989, 1999). In this way, we calculate spatially resolved maps of the surface sputtering rate at Europa. The AIKEF and GENTOO models have been extensively described in our previous publications. We therefore provide only a brief discussion of these two models here, and refer the reader to these prior publications for more information.

2.1. Model of Europa's Electromagnetic Environment

To calculate the three-dimensional structure of the perturbed magnetospheric environment near Europa, we apply the AIKEF hybrid model (kinetic ions and fluid electrons) originally developed by Müller et al. (2011). Unlike a single-fluid MHD model (e.g., Kabin et al., 1999), the hybrid approach is able to capture the dynamics of individual ion macroparticles, some of which possess velocity vectors far from the peak of the Maxwellian upstream distribution. Such ions impinge onto Europa along highly inclined trajectories (with respect to the corotation direction) and substantially contribute to the irradiation of the Moon's polar caps and downstream hemisphere (Addison et al., 2021). AIKEF has achieved excellent quantitative agreement with the magnetic field signatures measured near Europa during the E26 flyby of Galileo (Arnold et al., 2019), as well as plasma and magnetic field observations from several Callisto flybys (Liuzzo et al., 2015, 2016, 2017). Thus, AIKEF is highly suited for our study of magnetospheric ion sputtering of Europa's surface.

Throughout this article we will use the Cartesian, Europa-centered "EPhiO" coordinate system. In this system, the x -axis points in the direction of corotation, the z -axis points northward (i.e., parallel to Jupiter's spin axis), and the y -axis completes the right-handed system, pointing toward the giant planet. The basis vectors along these three axes are denoted \hat{x} , \hat{y} , and \hat{z} , respectively. In agreement with Galileo plasma observations (e.g., Bagenal & Dols, 2020; Bagenal et al., 2015; Kivelson et al., 2009), for the AIKEF model we assume the corotating, thermal plasma to consist of a singly charged, composite species of mass $m_0 = 18.5$ amu, with ion and electron temperatures $k_B T_0 = 100$ eV, and bulk velocity $\mathbf{u}_0 = 100$ km s⁻¹ \hat{x} . Galileo Plasma Subsystem (PLS) measurements have also shown the bulk plasma velocity to have radial (i.e., in the $\pm y$ direction) and polar (i.e., in the $\pm z$ direction) components near Europa's orbit (Bagenal et al., 2016). However, these components are, at most, $\approx 5\%$ of the azimuthal (corotational, i.e., along $+x$) component. The radial and polar components also have been observed to have different directions during different crossings of Europa's orbit, revealing that there is no consistent behavior of the radial or polar flow components near Europa (see Figure 7b of Bagenal et al., 2016). However, such weak radial and polar plasma velocity components would only cause a very subtle rotation of our surface flux patterns around the z and y axes, respectively, and as such we do not consider them here.

Europa's exosphere is treated as consisting entirely of O₂ (Plainaki et al., 2018), with a scale height of 100 km (Arnold et al., 2019; Arnold, Liuzzo, & Simon, 2020). Similar to Rubin et al. (2015), Arnold et al. (2019), and Harris et al. (2021), the exosphere in our model possesses an upstream-downstream asymmetry. In the Moon's orbital leading (downstream) hemisphere ($x > 0$), the exospheric density depends only on the radial distance to the surface and includes no latitudinal or longitudinal variations. Above the Moon's orbital trailing (upstream) hemisphere, the exospheric density profile is axisymmetric around the x axis and decreases with radial distance to the surface. However, it also drops with angular distance from the Moon's upstream apex (see Equation 2 of Arnold, Liuzzo, & Simon, 2020). The exosphere is mainly ionized through electron impacts, which dominate the ionization rate at Europa by over an order of magnitude compared to photoionization (Saur et al., 1998). The AIKEF simulation domain covers the volume bounded by $-9 R_E \leq x \leq 21 R_E$, $-10 R_E \leq y \leq 10 R_E$, and $-30 R_E \leq z \leq 30 R_E$. In order to achieve a high resolution near the Moon, AIKEF uses a hierarchical Cartesian grid, with a cell size of $0.02 R_E$ for the domain $|x|, |y|, |z| \leq 1.5 R_E$, $0.04 R_E$ for $1.5 R_E < |x|, |y|, |z| \leq 3 R_E$, and $0.08 R_E$ for $|x|, |y|, |z| > 3 R_E$.

While the southward ($B_{0,z} < 0$) component of the Jovian background magnetic field \mathbf{B}_0 near Europa remains nearly constant as the plasma sheet sweeps over the Moon (Kivelson et al., 1999), the $B_{0,x}$ and $B_{0,y}$ components exhibit oscillations in their strength and orientation on the scales of 20% and 50% of the background field magnitude, respectively (e.g., Schilling et al., 2007). Sweepback of the magnetic field lines within the plasma sheet causes the magnetic field to bulge toward upstream (Khurana & Kivelson, 1993). Therefore, the $B_{0,x}$ component oscillates near Europa as the center of the sheet passes above and below the Moon. The oscillation in the $B_{0,y}$ component arises from Europa's excursions away from Jupiter's magnetic equator. North of the magnetic equator, the Jovian magnetic field lines point away from Jupiter (i.e., in the $-y$ direction), whereas south of the magnetic equator the field lines point toward Jupiter ($+y$ direction). Since the plasma number density within the sheet follows a Gaussian profile with distance to the sheet's center (Bagenal & Delamere, 2011; Hill & Michel, 1976), the thermal plasma impinging onto Europa periodically varies in density over a synodic rotation. The plasma density is maximized at the center of the sheet, while at maximum elongation north or south the plasma is more dilute by a factor of ~ 5 (Bagenal & Delamere, 2011; Roth et al., 2014). Data from the Galileo PLS show no significant variation in plasma sheet density at Europa's orbit with local time (see Figure 1 of Bagenal & Delamere, 2011).

The magnetopause of Jupiter is located more than $40 R_J$ outside of Europa's orbit, so the plasma density at Europa is not significantly affected by the Moon's orbital position with respect to the magnetopause. For this reason, the empirical models of the plasma density along Europa's orbit provided by, for example, Bagenal et al. (2015), include only dependencies on the radial distance to Jupiter and vertical distance to the center of the sheet, but not on local time. The number density of the thermal plasma within the sheet does exhibit a local time dependence. However, this dependence becomes important only at radial distances far outside the orbit of Europa (Bagenal et al., 2016).

Addison et al. (2021) calculated the structure of the perturbed electromagnetic fields near Europa at three equally spaced points in time along a synodic rotation, namely when the Moon is located at (a) the center, (b) maximum elongation north, and (c) maximum elongation south of the plasma sheet. They then determined the spatial distribution of magnetospheric ion flux onto Europa's surface at each of these three locations. Finally, Addison et al. (2021) averaged these three flux maps across a synodic rotation, and compared the resulting map to the spatial distribution of ion flux calculated at the center of the plasma sheet (case (a)). These authors showed that the surface flux patterns from both scenarios possessed significant similarities. In both cases, the distribution of the total flux onto the surface was dominated by the contribution of the thermal ions, which were able to reach nearly every location on the surface, with the highest irradiation occurring near the upstream apex (see Figures 4g and 8f of Addison et al., 2021). Only in a narrow band near Europa's geographic equator was the thermal ion flux reduced by three to four orders of magnitude compared to the poles or the upstream apex. The surface flux pattern of energetic ions was also nearly identical in both scenarios (Figures 4h and 8e of Addison et al., 2021). While the spatial distribution of energetic ion influx was more uniform across the surface than that of the thermal ions, the energetic ions were found to preferentially impact Europa's high-latitude regions. In both cases, a circular depletion in the energetic ion flux by roughly an order of magnitude was identified near Europa's upstream apex. At no location on Europa's surface was the ion flux averaged over an entire synodic rotation different by more than a factor of 5 from the ion flux calculated near the center of the plasma sheet. Addison et al. (2021) therefore concluded that the distribution of ion surface flux onto Europa near the center of the plasma sheet is an excellent approximation of the averaged ion flux pattern onto the Moon over an entire synodic rotation.

Therefore, our study of surface sputtering is based on a single configuration of the ambient environment near Europa, namely one that is representative of the magnetospheric conditions near the center of the plasma sheet. The Jovian background magnetic field \mathbf{B}_0 for this model setup is determined by averaging the time-dependent magnetospheric field at Europa's position (given in Equation 17 of Schilling et al., 2007) over an entire synodic period, which yields a background magnetic field of $\mathbf{B}_0 = 410 \text{ nT } \hat{\mathbf{z}}$. We note that, with such a purely southward magnetic field, the induced dipole moment at Europa disappears (Zimmer et al., 2000). We set the upstream plasma density to $n_0 = 200 \text{ cm}^{-3}$, the same value utilized by Addison et al. (2021) to simulate Europa's conditions near the center of the plasma sheet. This value is in agreement with the upstream plasma density near the center of the plasma sheet as measured by the Galileo Plasma Wave Subsystem (PWS), see Roth et al. (2014). Such a density is also approximately in the middle of the range of densities derived by Bagenal et al. (2015), based upon comprehensive analysis of PWS data from Europa's orbit. The Alfvén speed $v_{A,0} = \frac{|\mathbf{B}_0|}{\sqrt{\mu_0 n_0 m_0}}$ in this configuration is 147 km s^{-1} , and the Alfvénic Mach number of the upstream plasma $M_{A,0} = \frac{u_{0l}}{v_{A,0}}$ is ~ 0.68 . The choice of this single electromagnetic field configuration facilitates the analysis of the influence of other important variables on surface sputtering rates. The role of factors, such as the impact angles of impinging ions and the time-varying surface temperature profile can be studied in isolation from the changing electromagnetic fields.

2.2. Model of Magnetospheric Ion Surface Flux

To calculate the spatial distribution of the magnetospheric ion flux onto Europa's surface, we use the GENTOO particle-tracing code (Addison et al., 2021; Liuzzo et al., 2019a, 2019b). GENTOO calculates the trajectories of individual macroparticles when moving through the perturbed electromagnetic fields from AIKEF. The GENTOO model utilizes a backtracing approach, that is, ion macroparticles are initialized on a grid across Europa's surface (which is equidistant in latitude and longitude) and traced *backwards* in time (model time step $\Delta t < 0$). At each grid point on the surface, particles are launched at equal angular increments across a half-sphere in velocity space, thereby encompassing all possible incident velocity vectors. Backtraced macroparticles whose trajectories re-intersect Europa's surface after launch are deleted from the simulation. In a forward-tracing approach, such an ion would have to pass through Europa's solid body in order to reach its starting location on the Moon's surface.

Macroparticles whose trajectories do not re-encounter Europa's surface, but reach the unperturbed magnetospheric environment, are considered to have "allowed" trajectories. Since the bounce times of magnetospheric ions are larger than the convection time of the plasma through Europa's interaction region, an ion with an allowed trajectory cannot make a second attempt to impact Europa's surface and become forbidden (Addison et al., 2021; Breer et al., 2019). In the forward-tracing picture, allowed particles are able to precipitate from Jupiter's magnetosphere onto Europa's surface, and thus contribute to surface flux.

We initialize ions on Europa's surface at discrete energies ranging from $E = \frac{1}{2}m(u_0 - v_{th})^2$ to $E = 10$ MeV. Here m is the mass of each ion, $u_0 = |\mathbf{u}_0|$ denotes the corotation speed, and $v_{th} = \sqrt{2k_B T/m}$ (where $k_B T$: ion temperature) is the thermal speed of the respective ion species. We choose intermediate energies at $E = \frac{1}{2}mu_0^2, \frac{1}{2}m(u_0 + v_{th})^2, 5$ keV, 10 keV, 50 keV, 100 keV, 500 keV, 1 MeV, and 5 MeV. The three lowest energies allow adequate coverage of the thermal ion regime, where the upstream distribution changes rapidly as a function of energy (see Figure 2 of Addison et al., 2021). In agreement with, for example, Mauk et al. (2004), ions traced by the GENTOO model are considered test particles, that is, they do not alter their local electromagnetic environment.

We calculate the trajectories of thermal and energetic sulfur, oxygen, and hydrogen ions, the dominant ion species near Europa as measured by the Galileo and Juno spacecraft (Clark et al., 2020; Cooper et al., 2001; Kim et al., 2020; Mauk et al., 2004). While the surface flux of the thermal plasma could in principle be calculated with the AIKEF hybrid code, this approach would yield maps with a four times lower resolution than the GENTOO model. The currents carried by the thermal ions (and their influence on the electromagnetic fields) are already taken into account in the AIKEF model and in the resulting field cubes provided to GENTOO. Therefore, the feedback of the thermal ions onto the fields does not need to be taken into account (a second time) in GENTOO. Each ion with an allowed trajectory in GENTOO possesses a counterpart within the framework of the hybrid model. Similar to Addison et al. (2021), the thermal plasma is modeled as consisting of $H^+, O^+,$ and S^{2+} , while the energetic plasma is modeled as consisting of $H^+, O^{2+},$ and S^{3+} . This approach is in agreement with data on charge states gathered by the Juno spacecraft (Clark et al., 2020; Kim et al., 2020). The thermal hydrogen has a temperature $k_B T_H = 20$ eV (Bagenal et al., 2015; Paterson et al., 1999), while the thermal oxygen and sulfur ions have a temperature of $k_B T_{O,S} = 100$ eV (Bagenal et al., 2015; Kivelson et al., 2009). Thus, the thermal velocities of the three ion species read $v_{th,H^+} = 63$ km/s, $v_{th,O^+} = 34$ km/s, and $v_{th,S^{2+}} = 24$ km/s for hydrogen, oxygen, and sulfur ions, respectively. The total thermal plasma density of $n_0 = 200$ cm⁻³ is divided amongst the three species (hydrogen, oxygen, and sulfur) using mixing ratios derived by Bagenal et al. (2015). The resulting densities of thermal sulfur, oxygen, and hydrogen ions are 112, 60, and 28 cm⁻³, respectively (Addison et al., 2021).

Once a backtraced ion macroparticle of a given energy with an "allowed" trajectory escapes into the ambient magnetospheric plasma, its contribution to the surface flux is calculated from measured upstream distributions. To do this, GENTOO invokes Liouville's Theorem, which states that, in the absence of collisions or other loss/production processes, the phase space density is conserved along each ion's trajectory. This allows the flux represented by an ion macroparticle in the upstream plasma to be related to the flux it carries onto Europa's surface. The energetic ion distributions outside of Europa's local interaction region are shaped by a multitude of magnetospheric processes, such as radial transport of charged particles within the Jovian magnetosphere and dissociation of sulfur dioxide from Io's volcanoes. To calculate the surface flux represented by each backtraced particle in GENTOO, we apply the ion distributions observed by Galileo in the vicinity of Europa's interaction region. In this way, we ensure that all of the above processes are properly accounted for when modeling ion precipitation onto Europa. Details of this procedure are discussed in Section 2.2 of Addison et al. (2021). A detailed justification for the applicability of Liouville's Theorem at Europa is also provided in Section 2.2 of Addison et al. (2021).

We utilize a drifting Maxwellian upstream distribution to calculate the surface flux of the (thermal) corotating plasma. The upstream energy distributions of energetic ions used in our model are a fit to EPD data taken during the E12 flyby of Galileo (Paranicas et al., 2002), which occurred when the Moon was located near the center of the Jovian plasma sheet (see Figure 2 of Addison et al., 2021). The energetic ion distributions measured by the Galileo spacecraft changed by less than an order of magnitude as a result of Europa's variable proximity to the center of the plasma sheet. Thus, applying the E12 distribution in our model setups does not introduce any significant uncertainties into our results. While Mauk et al. (2004) suggest the pitch angle distribution (PAD) of energetic ions near Europa to be isotropic to within 25%, subsequent analysis by Kollmann et al. (2016) and Nénon and André (2019) has revealed that the energetic ion PAD may in fact be "pancake-shaped," with a depletion of particles possessing pitch angles near 0°. However, for this study we assume the PAD of the energetic ions near

Europa to be isotropic, as Addison et al. (2021) found that the inclusion of an anisotropic PAD has only a minimal, quantitative effect on the surface flux pattern. These authors showed that inclusion of a pancake-shaped PAD causes a discernible reduction of the surface fluxes only in the MeV regime, where the energetic ion upstream distribution is only sparsely populated (see Figure 2 of Addison et al., 2021). At each latitude λ and longitude ϕ point on the GENTOO grid, the differential flux $dJ(E, \lambda, \phi)$ is calculated by summing the flux contributions of each macroparticle of a given energy with an allowed trajectory which was launched from that point.

We do not consider charge exchange reactions between magnetospheric ions and exospheric neutrals. Addison et al. (2021) found that these reactions only affect the surface flux of protons with energies below ~ 50 keV, which have negligible sputtering yields (Johnson et al., 2009, Section 2.3).

2.3. Sputtering Yields of Magnetospheric Ions

Based upon laboratory experiments, several empirical models have been developed for the sputtering yields Y of ions impinging onto water ice (e.g., Famá et al., 2008; Johnson et al., 2009; Teolis et al., 2017). Sputtering yields depend upon projectile species, energy, and impact angle, as well as the temperature and composition of the surface. Different surface species may be sputtered in varying amounts based upon the extent to which dissociative chemical processes have caused different molecules to accumulate in layers close to the surface. Each of the available sputtering yield models (e.g., Famá et al., 2008; Johnson et al., 2009; Teolis et al., 2017) matches laboratory data best only in a specific projectile energy window, or for a certain sputtered species. Therefore, calculation of sputtering rates across the range of incident magnetospheric ion energies observed at Europa requires a combination of yields from several models. Sputtering yields are expressed in units of molecules released per incident particle. In Sections 2.3.1 and 2.3.2 we describe our approach to calculate the surface sputtering rates of H_2O , O_2 , and H_2 at Europa from the surface flux maps of magnetospheric ions provided by GENTOO.

2.3.1. Sputtering Yields of H_2O

Europa's surface consists primarily of water ice, which may be chemically decomposed into constituent atoms via ion and electron impacts (Bar-Nun et al., 1985; Johnson et al., 2005). However, intact H_2O may be directly sputtered from the surface prior to any chemical decomposition. Data on sputtering yields generated by laboratory experiments has been fit with analytical forms by both Famá et al. (2008) and Johnson et al. (2009). Cassidy et al. (2013) showed that the model of Famá et al. (2008) matches the laboratory data for projectile energies below $E \approx 100$ keV, while that of Johnson et al. (2009) matches the data more closely above 100 keV. Since Europa's regolith is ~ 1 m deep (Carlson et al., 2009), water ice is present well beyond the depth to which a magnetospheric ion may penetrate (≈ 1 mm at most, Teolis et al., 2017). As such, the source of sputterable H_2O may be considered unlimited on short time scales. Over geologic timescales, sputtering may locally lead to lowered water ice concentrations (e.g., Ligier et al., 2016), gradually reducing H_2O yields from areas of consistently high bombardment. However, quantitative constraints on this thinning of the ice layer are yet to be determined through observations or modeling.

The sputtering yields of H_2O molecules are independent of surface temperature below 140 K (Baragiola et al., 2003), which is approximately the maximum surface temperature at Europa (Spencer et al., 1999). Hence, for the calculation of H_2O sputtering yields, we can omit the temperature-dependent term in the yield expressions of both Famá et al. (2008) and Johnson et al. (2009). The H_2O sputtering yields in our model are therefore given by

$$Y_{\text{H}_2\text{O}}(m, Z, E, \theta) = \begin{cases} \{A(m) S_n(m, Z, E) + B(Z) S_e^2(m, Z, E)\} \cos^{-f(m)}(\theta) & ; \quad E \leq E_T(m, Z) \\ \left\{ \left[C_1 \left(\frac{v}{Z^{1/3}} \right)^{C_2} \right]^{-1} + \left[D_1 \left(\frac{v}{Z^{1/3}} \right)^{D_2} \right]^{-1} \right\} \cos^{-f(m)}(\theta) & ; \quad E > E_T(m, Z) \end{cases} \quad (1)$$

where the top equation is that of Famá et al. (2008), the bottom equation is from Johnson et al. (2009), and $E_T(m, Z)$ is a "transition energy" at which we switch between the two models (see discussion below). The mass, atomic

number, and incidence angle (measured against the local surface normal) of the projectile ion are given by m , Z , and θ , respectively, while v is the velocity of the particle divided by $2.19 \times 10^6 \text{ m s}^{-1}$ (Johnson et al., 2009). The factors $A(m)$, $B(Z)$, and $f(m)$ are functions of projectile mass and atomic number and are given by Famá et al. (2008), while the constants $C_1 = 4.2$, $C_2 = 2.16$, $D_1 = 11.22$, and $D_2 = -2.24$ do *not* depend on projectile species and are provided by Johnson et al. (2009). The factor $f(m)$ controls the sensitivity of Y for each species to varying incidence angles, and reads $f(m) = 1.3$, $f(m) = 1.66$, and $f(m) = 1.75$ for hydrogen, oxygen, and sulfur ions, respectively. In addition, the yields calculated from Equation 1 are subsequently multiplied by a factor of 0.3 to account for the sticking of ejected H_2O within Europa's surface regolith (Cassidy et al., 2008; Cassidy & Johnson, 2005; Teolis et al., 2017). A similar combination of sputtering yield models has been implemented by, for example, Cassidy et al. (2013) and Vorburger and Wurz (2018) in order to study exospheric generation at Europa.

Cassidy et al. (2013) suggested that a suitable fit to laboratory data on sputtering yields can be accomplished by transitioning from the model of Famá et al. (2008) to that of Johnson et al. (2009) at $E \approx 100 \text{ keV}$. However, such a procedure results in discontinuities of the sputtering yield profiles of all three ion species. Attempting to avoid such jumps in the sputtering yield profiles, we define a transition energy, $E_T(m, Z)$, for each species at which we switch from the yield profiles of Famá et al. (2008) at $E \leq E_T(m, Z)$ to Johnson et al. (2009) at $E > E_T(m, Z)$. We set the transition energy of hydrogen and sulfur ions to the energy at which yield curves from the two models intersect, roughly $E_T = 30$ and 50 keV , respectively. Not only does this choice ensure continuity of the sputtering yield profiles for these two species, but the values of E_T are also close to the value of $E_T \approx 100 \text{ keV}$ suggested by Cassidy et al. (2013). Since the starting energies of the ions modeled here are discrete, the shift of the transition energy from the 100 keV value suggested by Cassidy et al. (2013) to our proposed values only affects the calculation of sputtering yields at two energies (50 and 100 keV) for sulfur, and one energy (100 keV) for hydrogen. At these energy values, the yields from the empirical models of Johnson et al. (2009) and Famá et al. (2008) do not differ by more than a factor of 3. As such, the shift of the transition energy from 100 to 50 keV (hydrogen) and 30 keV (sulfur) does not substantially affect our results. The models of the sputtering yields from oxygen ions presented by Famá et al. (2008) and Johnson et al. (2009) do not intersect, thus the occurrence of a discontinuity in the yield curve for oxygen cannot be avoided. We therefore set the transition energy for sputtering by oxygen ions to $E_T = 100 \text{ keV}$, in agreement with the method of Cassidy et al. (2013). This approach results in a jump in the sputtering yields by a factor of ~ 1.5 at $E_T = 100 \text{ keV}$.

The expression presented by Famá et al. (2008) for the H_2O sputtering yield is written in terms of the nuclear and electronic stopping powers of incident ions ($S_n(m, Z, E)$ and $S_e(m, Z, E)$, respectively), for which those authors provide empirical fits. These stopping powers represent the rate at which an incident ion loses its energy with depth in the surface, either by nuclear/momentum transfer (elastic) collisions ($S_1(m, Z, E)$) or electronic excitation of surface molecules ($S_2(m, Z, E)$). Nuclear collisions dominate the yields at projectile energies below $\approx 50 \text{ keV}$, while electronic excitation reactions become predominant at higher energies. The expression provided by Johnson et al. (2009) is a fit to laboratory data gathered in the electronic regime. Therefore, while this expression is not written in terms of the electronic stopping power S_e , it still describes yields Y associated with electronic sputtering.

Figure 1a displays the sputtering yields of H_2O as a function of projectile energy from 10 eV (approximately the corotation energy of protons) to 10 MeV , calculated from Equation 1. We do not consider “secondary” sputtering of the surface by ionospheric pickup ions ($E \ll 10 \text{ eV}$), as the contribution of this process to atmospheric generation has been found to be a factor of 100 weaker than sputtering by magnetospheric ions (Saur et al., 1998). We note that sputtering by ionospheric ions may play an important role at Ganymede (Carnielli et al., 2020). In Figure 1a we discriminate between the three projectile ion species most prevalent along Europa's orbit, with the yields from hydrogen, oxygen, and sulfur impacts shown in red, blue, and green, respectively. The transition energy E_T for each species is marked with a vertical, dashed line of corresponding color. Due to their similar atomic numbers, the H_2O sputtering yields of incident oxygen and sulfur ions (blue and green curves) have very similar values over a wide range of energies; only at the very top of the energy range considered ($E \approx 10 \text{ MeV}$) do they differ by over an order of magnitude. The yield of incident hydrogen ions (red) is consistently smaller than that of the two heavy ion species, due to their small mass and atomic number. This difference in the H_2O sputtering yields between hydrogen and oxygen/sulfur varies from a factor of ~ 3 at 10 eV to almost six orders of magnitude at 10 MeV (see Figure 1a). In general, the sputtering yields increase gradually with energy in the nuclear collision

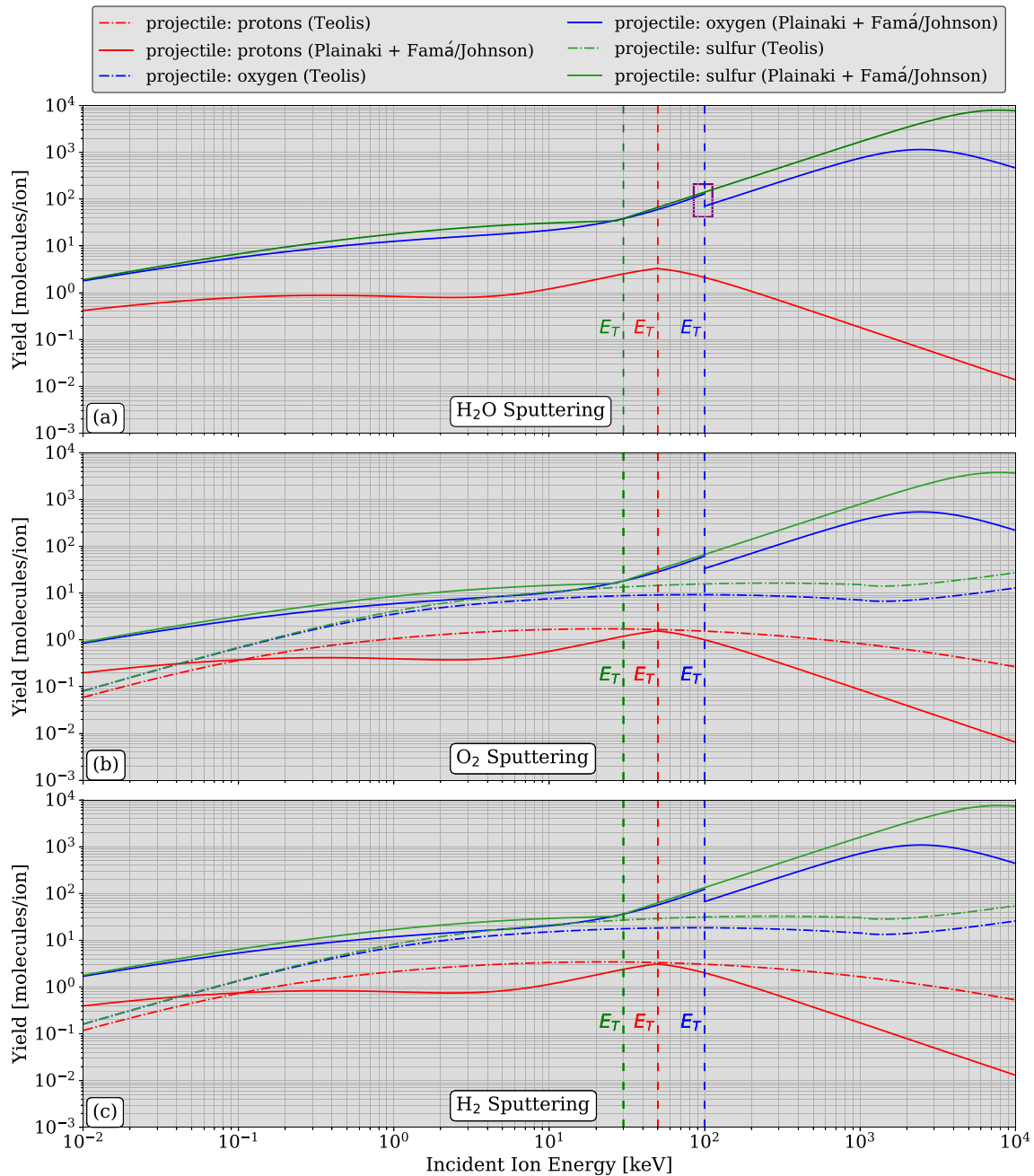


Figure 1. Sputtering yields in molecules/ion of H₂O (a), O₂ (b), and H₂ (c) via impacts by normally incident ($\theta = 0^\circ$) hydrogen (red), oxygen (blue), and sulfur (green) ions with energies from 10 eV to 10 MeV onto water ice at 100 K. Yields derived via the models of Plainaki et al. (2013), Famá et al. (2008), and Johnson et al. (2009) are shown as solid lines, while yields from Teolis et al. (2017) are shown as dash-dotted lines. The transition energy E_T is denoted with a vertical dashed line in the color corresponding to each species. The model of Famá et al. (2008) is applied for energies below the transition energy E_T , while the model Johnson et al. (2009) is used above E_T . The purple box near 100 keV in (a) highlights the unavoidable jump between the sputtering yields from oxygen ions of the two models. Yields derived with the model of Teolis et al. (2017) are valid across the entire energy range considered, that is, we do not have to switch between different models at the transition energy.

regime (below ≈ 50 keV), before growing rapidly above this energy due to the onset of electronic excitations. The sputtering yields of heavy ions maximize in the MeV regime, while the yields of protons maximize near 50 keV.

Laboratory experiments by Gibbs et al. (1988) and Vidal et al. (2005) revealed that sputtering yields follow a $\cos^{-f(m)}(\theta)$ dependence on incidence angle in the electronic sputtering regime. Standard linear cascade theory predicts a similar dependence on incidence angle for nuclear sputtering yields (Famá et al., 2008). The form of $f(m)$

for H₂O sputtering is provided by Famá et al. (2008) based upon laboratory data, and ranges from $f(m) \approx 1.3$ –1.8 depending upon the projectile species. Therefore, sputtering yields can grow sharply with increasing incidence angle. For example, an impinging sulfur ion with an incidence angle of $\theta = 80^\circ$ sputters up to 20 times more H₂O than a sulfur ion with $\theta = 0^\circ$. This form of the angular dependence exhibits a singularity at $\theta = 90^\circ$, which would inflate the modeled sputtering yield to infinity. To avoid this, GENTOO does not initialize backtraced macroparticles exactly tangential to the surface, rather, only at angles of $\theta \leq 87^\circ$.

Previous studies of magnetospheric ion sputtering at Jupiter's icy moons have typically assumed that all impinging ions hit the surface at the same incidence angle θ . This assumption accounts for the fact that, in the absence of a detailed, high-resolution topographical surface map (down to centimeter-scale), it is not feasible to precisely determine the incidence angle of an impinging ion. An ion may impact a crack or crevice on the Moon's surface and therefore impinge at a completely different angle than if it had hit a perfectly smooth sphere. Therefore, particle-tracing models often assume that the incidence angles of impacting ions average to a certain value within each cell of the grid used to discretize the surface. Cassidy et al. (2013) assumed a normal angle of incidence ($\theta = 0^\circ$) for all impinging ions at Europa, while Carnielli et al. (2020) modeled ion sputtering at Ganymede with $\theta = 45^\circ$. So far, only Plainaki et al. (2015) studied ion sputtering at Ganymede without assuming a single, average incidence angle: their model considers the actual incidence angles of the ions onto a smooth sphere. Therefore, in order to constrain the uncertainties associated with the treatment of the incidence angle we will calculate H₂O sputtering rates with (a) all ions treated as impacting normally (similar to Cassidy et al., 2013) and (b) using the actual incidence angles onto a perfectly smooth sphere as obtained from GENTOO.

2.3.2. Sputtering Yields of O₂ and H₂

Sputtering of O₂ and H₂ from Europa's surface is the result of radiolysis and subsequent buildup of each type of molecule in the upper layers of the ice (e.g., Teolis et al., 2005, 2017). The sputtering of O₂ at Europa is of particular interest, as this process constitutes the main source of the Moon's near-surface (altitude <300 km) exosphere. Within much of this region O₂ dominates the number density by up to two orders of magnitude, compared to H₂O, H₂, or other trace species (Plainaki et al., 2018; Vorbürger & Wurz, 2018). However, the abundance of H₂O has been found to exceed that of O₂ by an order of magnitude in a localized region above the central trailing hemisphere (Roth, 2021).

At the time of this study, two conceptually different models of O₂ sputtering have been applied in order to calculate the source rate of O₂ via magnetospheric ion sputtering at Europa. Plainaki et al. (2013) modeled the O₂ sputtering yield by using the temperature-dependent term in the equation for Y provided by Famá et al. (2008). They judged this approach to be accurate to within one order of magnitude. The sputtering yield of O₂ in this formulation (see, e.g., Plainaki et al., 2015) is given by

$$Y_{O_2}(m, Z, E, \theta, T) = \frac{1}{2} Y_{H_2O}(m, Z, E, \theta) \Phi(T), \quad (2)$$

where T is the temperature of the surface element from which material is sputtered, and Y_{H_2O} is given in Equation 1. The temperature dependence of the sputtering yield

$$\Phi(T) = q_0 \exp \left[-\frac{E_A}{k_B T} \right], \quad (3)$$

resembles that of a Maxwell-Boltzmann distribution (Famá et al., 2008; Johnson et al., 2009; Teolis et al., 2017). In Equation 3, $q_0 = 1,000$ is a scaling factor and $E_A = 0.06$ eV is the activation energy required for breakdown of surface constituents (Johnson et al., 2009). The factor of $\frac{1}{2}$ in Equation 2 arises from the fact that two H₂O molecules must be decomposed in order for one O₂ to form (Cassidy et al., 2010). The sputtering yield of H₂ is therefore always twice that of O₂, that is,

$$Y_{H_2}(m, Z, E, \theta, T) = 2 Y_{O_2}(m, Z, E, \theta, T), \quad (4)$$

which holds regardless of the formulation for $Y_{O_2}(m, Z, E, \theta, T)$. Figures 1b and 1c display the sputtering yields at $T = 100$ K (roughly the mean temperature of Europa's surface, e.g., Spencer et al., 1999) of O₂ and H₂, respectively. The factor $\Phi(T)$ ranges from a value of 10^{-2} at 60 K to a value of 7 at 140 K, the approximate minimum and maximum surface temperatures at Europa (e.g., Oza et al., 2019; Spencer et al., 1999). Therefore, the O₂ and H₂

yields calculated via the model of Plainaki et al. (2013) follow from the H₂O yields (Equation 1) by multiplication with $\frac{1}{3}\Phi(T)$ for oxygen and $\frac{2}{3}\Phi(T)$ for hydrogen. In Figure 1, we calculate the yield curves assuming a constant surface temperature of $T = 100$ K.

The O₂ sputtering yield model of Plainaki et al. (2013) is based upon available sputtering models of H₂O. As such, it assumes that, like H₂O, substantial amounts of O₂ are present at any depth to which a magnetospheric ion may penetrate. Hence, their sputtering yield grows with energy, since higher energy ions penetrate deeper into the surface (up to 10^7 Å for 10 MeV protons, see, e.g., Teolis et al., 2017) and interact with more material than their lower energy counterparts.

An alternative method for calculating the sputtering yields of O₂ and H₂ is presented by Teolis et al. (2010, 2017). Based upon the findings of Petrik et al. (2006) and Teolis et al. (2005, 2009), these authors suggested that O₂ and H₂ molecules are mainly concentrated within the first ≈ 28 Å of Europa's surface, while their densities decrease sharply below this thin upper layer. Thus, penetration of projectile ions beyond this thin layer makes only a very minor additional contribution to the release of O₂ or H₂. Teolis et al. (2010, 2017) formulate a novel method of calculating O₂ sputtering yields which considers this decreasing density of sputterable molecules at ion penetration depths greater than ≈ 28 Å. Their expression for O₂ sputtering yields reads

$$Y_{O_2}(E, \theta, T) = E g_{O_2}^0 x_0 \left[1 - \exp\left(\frac{-r_0(E)\cos(\theta)}{x_0}\right) \right] \frac{1}{r_0(E)\cos(\theta)} (1 + \Phi(T)), \quad (5)$$

where $g_{O_2}^0 = 5 \times 10^{-3} \text{ eV}^{-1}$ is the (constant) sputtering yield per energy when the surface temperature is below ≈ 80 K, $x_0 = 28$ Å is the thickness of the concentrated layer of O₂ and H₂ molecules directly beneath the surface, and $r_0(E)$ is the energy-dependent penetration range of the projectile (Teolis et al., 2017; Ziegler & Manoyan, 1988). The sputtering yields of H₂ are again twice the O₂ yields (Equation 4). The form of $\Phi(T)$ is the same as in Equation 2. Values of $r_0(E)$ in our model are taken from a fit to the curve provided by Teolis et al. (2017, Figure 4). When the penetration depth $r_0(E)\cos(\theta)$ of the projectile, that is, the penetration range $r_0(E)$ projected onto the local surface normal, greatly exceeds the O₂ layer depth x_0 , the exponential term in Equation 3 approaches zero. The sputtering yield of O₂ then becomes inversely proportional to the energy-dependent penetration depth. Note that the angular dependence of Equation 5 is limited to the two occurrences of the penetration depth of the projectile, $r_0(E)\cos(\theta)$. At high penetration depths ($r_0(E)\cos(\theta) \gg x_0$), the yield becomes proportional to $\cos^{-1}(\theta)$, similar to the angle dependence of Equations 1 and 2 with $f(m) = 1$. Due to the negligible sticking coefficient of O₂ (Saur et al., 1998), it is not necessary to include a reduction factor in the O₂ yields to account for sticking within the regolith (as is done for H₂O).

Yields derived at $T = 100$ K with the formulation of Teolis et al. (2010, 2017) are shown in Figure 1b for O₂ and Figure 1c for H₂ as dash-dotted lines. Only for oxygen and sulfur impacts between 1 and 30 keV do the O₂ yields calculated with the model of Teolis et al. (2017) approximately match those of Plainaki et al. (2012). The yields from the two models differ by up to an order of magnitude below this energy range, and by over two orders of magnitude above this range. For hydrogen impacts, sputtering yields calculated with the methods of Plainaki et al. (2012) and Teolis et al. (2017) are different by one to two orders of magnitude across the entire energy range considered, except in very narrow windows near 4×10^{-2} and 100 keV (see Figure 1a). The yields from the model of Teolis et al. (2017) initially grow with energy (and associated penetration depth), but level off near 10 keV as the ions pass deeper into surface layers where little O₂ or H₂ is present.

Observed sputtering yields of O₂ and H₂ increase exponentially with temperature above ~ 70 K, while below 70 K they are roughly constant with temperature (Baragiola et al., 2003). The models of Plainaki et al. (2012) and Teolis et al. (2017) each utilize a slightly different form to emulate this temperature dependence: $Y \propto \Phi(T)$ and $Y \propto [1 + \Phi(T)]$, respectively (see Equations 2 and 5). Therefore, while the O₂ sputtering yields of Plainaki et al. (2012) approach a value of zero when the surface temperature decreases below 70 K, the yields of Teolis et al. (2017) level off at nonzero values in this temperature regime, which more closely matches laboratory measurements (see Figure 5 of that article).

In addition, Teolis et al. (2005, 2010, 2017) suggest that a water ice surface requires a minimum irradiation dosage of 10^{15} cm^{-2} before the O₂ sputtering yield displays a response to changes in the surface temperature. At Europa, such a dosage from impinging magnetospheric ions alone requires ~ 3 orbits around Jupiter to accumulate (Addison et al., 2021). Considering only magnetospheric ion bombardment, a discernible reaction of the O₂

sputtering rate at Europa to varying solar orientation (Plainaki et al., 2013) would therefore only occur on time scales far greater than the Moon's orbital period. In other words, the surface temperature profile would be "reset" before the ice has adjusted to the change in temperature encountered along Europa's orbit. In this picture, the sputtering yields can be calculated by considering a diurnally averaged temperature profile (i.e., averaged over an entire orbit).

However, magnetospheric electrons also impart a significant irradiation dosage onto Europa's surface (e.g., Dalton et al., 2013; Paranicas et al., 2001, 2007). Indeed, recent analysis by Davis et al. (2021) suggests that electrons may irradiate Europa's surface at even higher levels than the ions, although their study did not take into account shielding of the surface by the Moon's plasma interaction. Such shielding has been found to sharply reduce the precipitation of magnetospheric electrons onto Callisto (Liuzzo et al., 2019a). Therefore, the magnetospheric electron fluxes onto Europa's surface calculated by, for example, Paranicas et al. (2001, 2007), Dalton et al. (2013), and Nordheim et al. (2018) for uniform fields can be considered only an upper limit to electron surface irradiation. However, modeling of magnetospheric electron bombardment at Europa is a non-trivial task, requiring extensive modifications to the GENTOO framework. Electrons with energies >50 keV display significant relativistic mass growth, changing the equation of motion that must be solved in order to determine their trajectories. Furthermore, the bounce times of magnetospheric electrons can be smaller than the convection time of the plasma through Europa's interaction region (Paranicas et al., 2009). Modeling of electron bombardment therefore requires the implementation of a global model of Jupiter's magnetosphere, and is beyond the scope of this study. However, if electrons contribute to surface irradiation to the same extent (or greater) as the ions, the 10^{15} cm⁻² irradiation dose required for the ice to adapt to surface temperature changes (Teolis et al., 2017) may be reached in far less than a European day. In that case, variations of the surface temperature profile generated by Europa's changing orientation with respect to the Sun need to be considered.

Our study will take into account the availability of two conceptually different models of O₂ and H₂ sputtering at Europa. In addition, we consider the uncertainty regarding the response of surface sputtering to changes in the incident solar flux which results from the Moon's orbital motion. We shall compare maps of the O₂ and H₂ sputtering rates utilizing the approaches of both Plainaki et al. (2013) and Teolis et al. (2017). In addition, we will model the spatial distribution of O₂ and H₂ sputtering rates for four different orientations of the Sun relative to the incident plasma flow, as well as for a temperature profile averaged over a full European day. Specifically, we examine the O₂ and H₂ sputtering rates at Europa while the Moon is located at 06:00, 12:00, 18:00, and 23:30 LT. We do not consider the scenario of exactly 00:00 LT, as in this configuration Europa is in eclipse (see, e.g., Cassidy et al., 2008; Oza et al., 2019). The Moon only spends $\sim 3\%$ of its orbit in eclipse, and the surface temperature quickly recovers (after ~ 6 hr, compared to an orbital period of 80 hr, see, e.g., Oza et al., 2019). Since our priority is to systematically assess the role of changing solar orientation along a full orbital period (rather than the special case of eclipse), we calculate maps of the O₂ and H₂ surface sputtering rate at 23:30 LT, just prior to Europa entering Jupiter's optical shadow. In this case, the sub-solar point is located only 6° east of where it would be in the (hypothetical) case of a Sun-illuminated Europa at 00:00 LT.

A global illustration of Europa's orbit showing each of these four cases, along with maps of the resultant surface temperature profiles, is displayed in Figure 2. Maps of the surface temperature are displayed in the West Longitude system, where longitude ϕ increases in a clockwise direction when viewed from the north ($z > 0$). In this system, Europa's sub-Jovian, downstream, anti-Jovian, and upstream apices are located at $\phi = 0^\circ, 90^\circ, 180^\circ,$ and 270° , respectively. These maps range in latitude from $\lambda = -90^\circ$ (denoting the south pole) to $\lambda = 90^\circ$ (north pole).

For each of these four orbital positions, a map of the surface temperature profile is calculated using the thermophysical model THERMPROJRS (Spencer et al., 1989, 1999). The THERMPROJRS model solves the conductive heat flow equation for a surface layer of a given thermal inertia and bolometric albedo. A steady-state surface temperature is then calculated assuming equilibrium between solar heat influx and thermal emission from the Moon. For our simulations, we utilize values of the emissivity and thermal inertia at Europa of 0.9 and 7×10^4 erg m⁻² s^{-1/2} K⁻¹, in agreement with Spencer et al. (1999). Their thermophysical model assumes the albedo to be uniform across Europa's surface. However, analysis of Galileo PPR data by Rathbun et al. (2010) and Oza et al. (2019) has demonstrated that Europa's surface albedo varies linearly with longitude from a minimum of 0.45 near the upstream apex to a maximum of 0.65 near the downstream apex. In order to capture this upstream-downstream asymmetry in Europa's surface brightness, we set the albedo to 0.45 at 18:00 LT (where the Moon's dayside and upstream hemispheres coincide), and to 0.65 at 06:00 LT (where the dayside and downstream

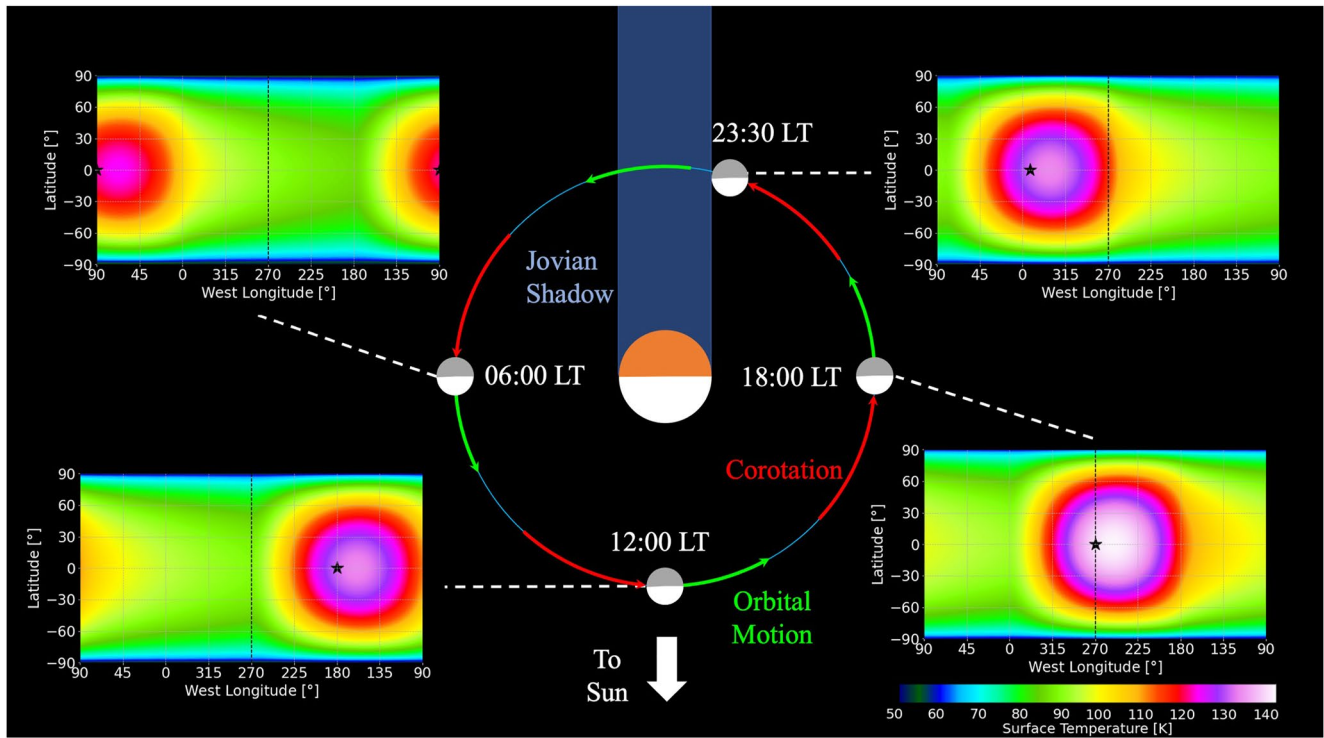


Figure 2. Orientation of Europa relative to Jupiter and the Sun for 06:00, 12:00, 18:00, and 23:30 LT, as described in Section 2.3.2. Jupiter (orange nightside and white dayside) is located in the center of the figure. Red arrows indicate the direction of the corotating plasma flow, while green arrows indicate the direction of Europa’s orbital motion. For each orbital position, Europa’s nightside hemisphere is shown in gray, while the Sun-lit/dayside hemisphere is colored white. Next to each of the four orbital positions is a plot of the surface temperature profile in West Longitude coordinates, with Europa’s sub-Jovian, downstream, anti-Jovian, and upstream apices located at longitudes of 0°, 90°, 180°, and 270°, respectively. The sub-solar point is marked with a black star, and a vertical dashed line marks a semi-meridian through the upstream apex. *Note.* That at 06:00 LT, the black star is split between the left and right sides of the temperature map.

hemispheres coincide). At 12:00 and 23:30 LT, when Europa’s terminator plane is approximately aligned with the corotation direction, the albedo is set to 0.55, that is, we use the average of the upstream and downstream hemisphere values. The lower albedo at 18:00 LT in our model results in a slightly higher surface temperature by ~15% compared to 06:00 LT, and 8% compared to 12:00 and 23:30 LT (Figure 2). The temperature maps in Figure 2 each display a bullseye-like enhancement around the apex of the dayside hemisphere, as well as a “tail” of increased temperature extending eastward. This tail is a result of the thermal inertia of the surface material, which partially retains the heat after a surface element has rotated out of daylight.

The four surface temperature profiles shown in Figure 2 are averaged in order to produce a map of the average temperature profile over a complete orbit (“diurnal-average,” see Figure 3). The diurnally averaged temperature profile is *not* uniform in longitude, since the Sun-lit hemisphere heats to higher temperatures at 18:00 than at 06:00 LT. Averaging the surface temperature over a full European orbit therefore results in a profile which is hotter upstream and cooler downstream, albeit with a weaker upstream-downstream discrepancy compared to 18:00 LT (≈ 45 K vs. ≈ 60 K, see Figures 2 and 3). In reality, the diurnally averaged temperature profile may be slightly cooler, since our model does not consider the drop in surface temperature during and after eclipse. In each scenario (the four local times and the diurnal average), the O_2 and H_2 sputtering yields are calculated with the respective temperature profile and the temperature dependence $\Phi(T)$, as given in Equations 2 and 5.

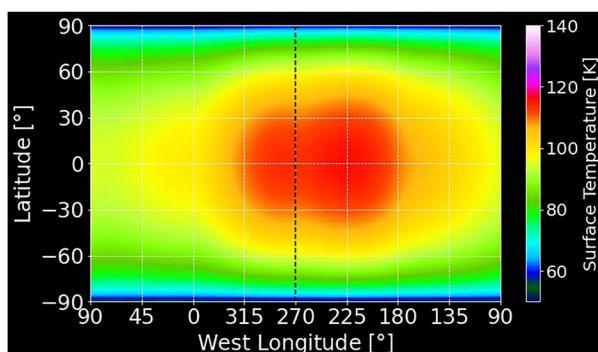


Figure 3. Diurnally averaged surface temperature profile at Europa, calculated using the four temperature profiles shown in Figure 2.

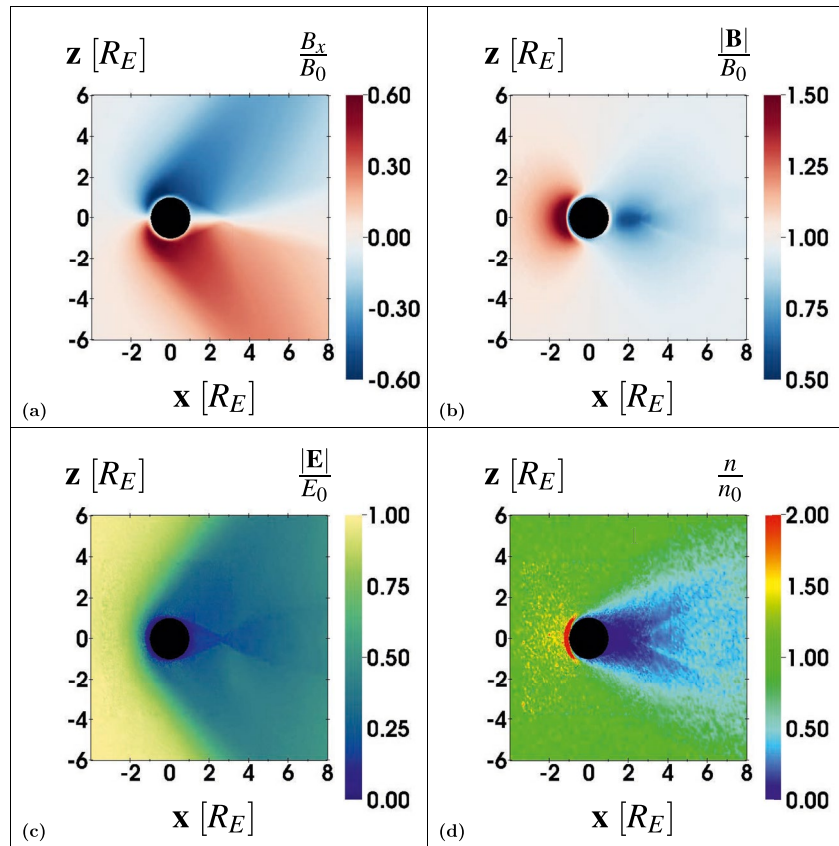


Figure 4. Electromagnetic and plasma environment near Europa, as calculated by the AIKEF model. All quantities are shown in cuts through the (x, z) plane, which contains the upstream flow velocity \mathbf{u}_0 , the background magnetic field \mathbf{B}_0 , and the center of Europa. (a) and (b) Displays the B_x component and magnitude of the magnetic field, respectively, as a fraction of the background field magnitude $|\mathbf{B}_0| = B_0 = 410$ nT. (c) Displays the electric field magnitude, normalized to the background convective electric field strength $E_0 = u_0 B_0 = 41$ mV m⁻¹. (d) Displays the number density of the magnetospheric plasma, as a fraction of the upstream density $n_0 = 200$ cm⁻³.

3. Results

3.1. Hybrid Simulation of Europa's Electromagnetic Environment

Figure 4 displays the structure of Europa's perturbed electromagnetic and plasma environment, as calculated by the AIKEF model. All quantities in Figure 4 are presented in cuts through the three-dimensional simulation domain at $y = 0$, that is, in the plane that contains the corotational flow velocity \mathbf{u}_0 , the background magnetic field \mathbf{B}_0 , and the center of the Moon. The first row (Figures 4a and 4b) displays the flow-aligned component of the magnetic field, B_x , and the magnitude of the magnetic field, $|\mathbf{B}|$, respectively. The magnitude of the electric field, $|\mathbf{E}|$, is shown in Figure 4c. Finally, the number density of the corotating plasma, n , is presented in Figure 4d.

Ionization of Europa's exosphere drains momentum from the upstream plasma, causing the magnetospheric ion number density to grow to over twice the background value $n_0 = 200$ cm⁻³ above the Moon's upstream hemisphere (Figure 4d). Ionospheric ions are convected downstream, refilling the Moon's magnetospheric plasma wake and maintaining pressure balance with the adjacent flow (see Figure 3 of Addison et al., 2021). The frozen-in magnetospheric field lines pile up above Europa's orbital trailing hemisphere, leading to an enhancement in the magnetic field magnitude by 50% compared to the background value (red region in Figure 4b). This upstream pileup is accompanied by a weakening of the magnetic field magnitude by 50% immediately downstream of the Moon (blue region in Figure 4b). The plasma interaction also generates a system of Alfvén wings which extend north and south from Europa to Jupiter's polar ionosphere (Neubauer, 1980, 1998). The Alfvén wings are tilted against the z -axis by an angle of $\arctan(M_A) = 34^\circ$, where $M_A = 0.68$ is the Alfvénic Mach number. Inside of the Alfvén wing tubes the field possesses a flow-aligned component south of the Moon ($B_x > 0$, red region

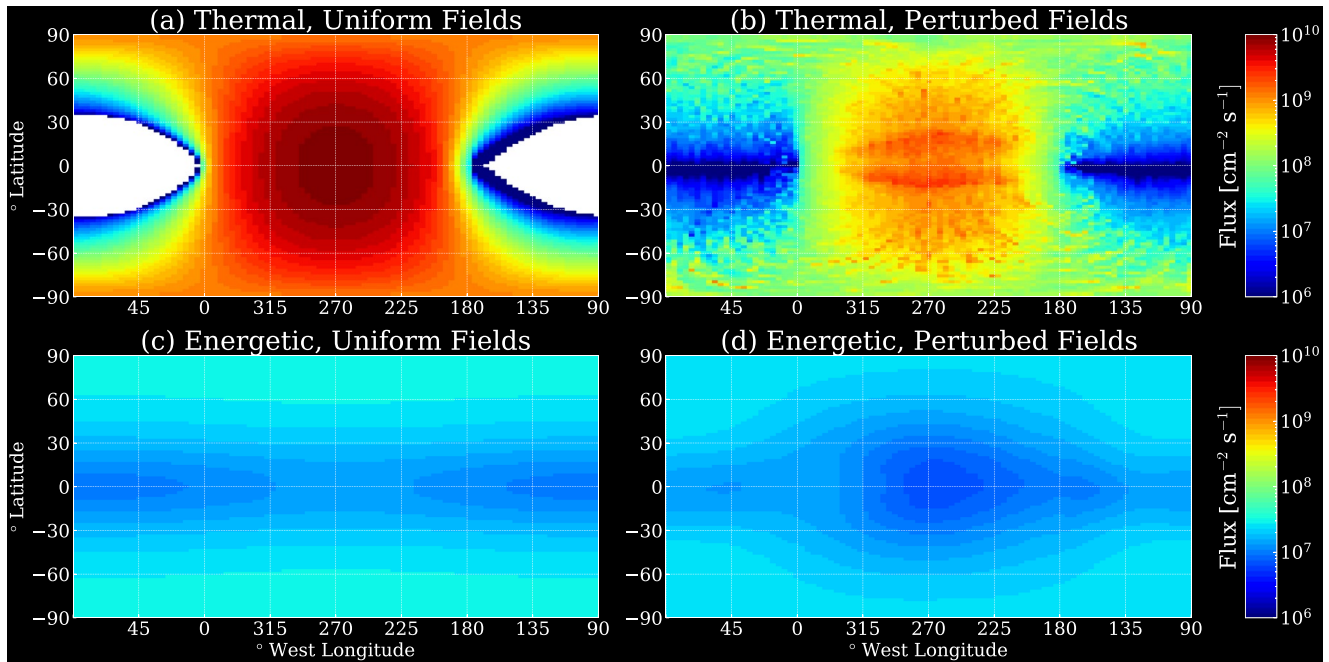


Figure 5. Surface flux maps of magnetospheric ions (hydrogen, oxygen, and sulfur) at Europa, calculated with the GENTOO model. The first row (a) and (b) Displays the surface flux of the thermal ion population, while the second row. (c) and (d) Shows the flux from the energetic ion population (energies $5 \text{ keV} \leq E \leq 10 \text{ MeV}$). The left column (a) and (c) shows fluxes calculated with the uniform electromagnetic fields \mathbf{B}_0 and \mathbf{E}_0 , while the right column (b) and (d) shows fluxes calculated with the perturbed fields determined by AIKEF. Each map is shown in the West Longitude system. The white region in (a) indicates areas in Europa’s downstream hemisphere where the thermal ion surface flux is exactly zero.

in Figure 4a), and a component antiparallel to the flow direction north of the Moon ($B_x < 0$, blue region in Figure 4a). The magnetospheric plasma slows within and downstream of the Alfvén wings, causing the downstream reduction in the electric field seen in Figure 4c.

For a more detailed discussion of the electromagnetic field perturbations near Europa, the reader is referred to our numerous preceding publications that applied the same model to this Moon (Addison et al., 2021; Arnold et al., 2019; Arnold, Liuzzo, & Simon, 2020; Arnold, Simon, & Liuzzo, 2020; Breer et al., 2019).

3.2. Magnetospheric Ion Surface Fluxes and Sputtering Rates of H_2O

In Figure 5 we present maps of the magnetospheric ion surface fluxes onto Europa for both the thermal (Figures 5a and 5b) and energetic (Figures 5c and 5d) regime, as calculated by the GENTOO model. The left column (Figures 5a and 5c) displays flux maps calculated with only the uniform Jovian magnetic field \mathbf{B}_0 and the undisturbed convective electric field \mathbf{E}_0 , while the right column displays flux maps determined with the perturbed electromagnetic fields from AIKEF (see Figure 4). Figure 6 features maps of the H_2O sputtering rates across Europa’s surface from thermal ions (Figures 6a–6c), energetic ions (Figures 6d–6f), and magnetospheric ions of all energies and species considered in this study (Figures 6g–6i). The first column (Figures 6a, 6d, and 6g) displays H_2O sputtering rates calculated with a uniform field configuration, as well as with the modeled incidence angles from GENTOO used in Equation 1. Sputtering rates calculated with the perturbed fields from AIKEF and the incidence angles from GENTOO are presented in the second column (Figures 6b, 6e, and 6h).

Finally, to isolate the influence of non-uniform ion incidence angles on the H_2O sputtering rate, the third column (Figures 6c, 6f, and 6i) displays H_2O sputtering rates determined with perturbed fields, but with the incidence angle of all impinging ions set to a constant value ($\theta = 0^\circ$) in Equation 1. This specific choice of incidence angle is consistent with the approach of Cassidy et al. (2013), but still somewhat arbitrary. Regarding the angle dependence of the sputtering yields, the choice of $\theta = 0^\circ$ gives equal weight to all three ion species ($\cos^{-f(m)}(0) = 1$), while a value of $\theta > 0^\circ$ weights the three species differently (due to the mass dependence of $f(m)$). However, choosing a value of, for example, $\theta = 45^\circ$, as done at Ganymede by Carnielli et al. (2020), results in (at maximum)

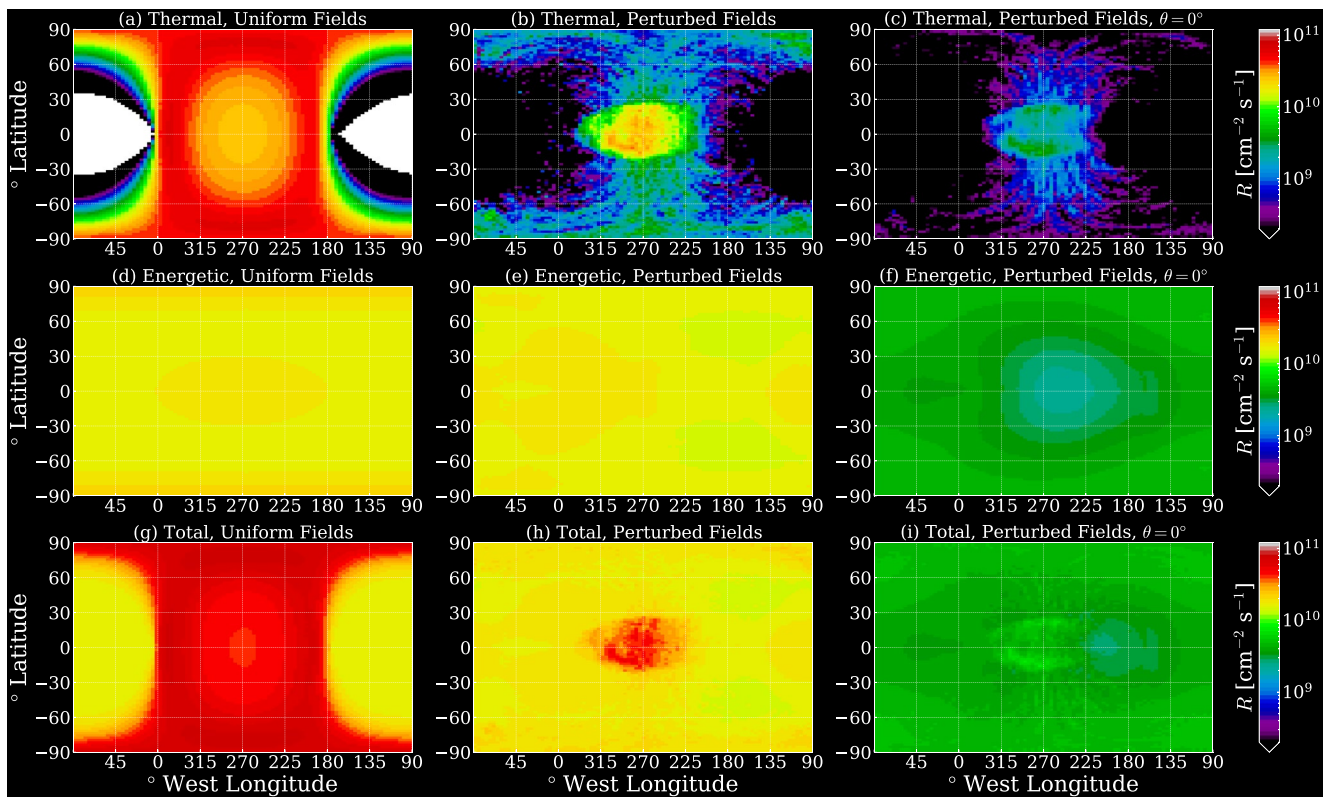


Figure 6. H₂O surface sputtering rates from impacts by all magnetospheric ion species (hydrogen, oxygen, and sulfur) considered in this study. Each map is displayed in the West Longitude system as described in the text. The first column (a), (d), and (g) shows H₂O sputtering rates calculated with only the uniform background electromagnetic fields \mathbf{B}_0 and \mathbf{E}_0 included, while the second column (b), (e), and (h) displays H₂O sputtering rates calculated using Europa’s perturbed electromagnetic environment from the AIKEF model. Both the first and second columns utilize the actual incidence angles θ of the incoming ions in their calculation of the sputtering yields (Equation 1). The third column (c), (f), and (i) displays H₂O sputtering rates calculated with perturbed electromagnetic fields (as in the second column), but with the incidence angles of all impinging ions set to $\theta = 0^\circ$ in Equation 1. From top to bottom, the rows display H₂O sputtering rates of thermal ions (a)–(c), energetic ions with energies $5 \text{ keV} \leq E \leq 10 \text{ MeV}$ (d)–(f), and the total sputtering rate of all magnetospheric ions (thermal and energetic, (g)–(i)). White regions in (a) indicate areas where the sputtering rate from thermal ion impacts is exactly zero.

a 14% enhancement of the H₂O sputtering yield of one ion species compared to another. Therefore, the choice of a constant incidence angle $\theta > 0^\circ$ would only cause a minor, quantitative enhancement of the H₂O sputtering rate compared to when $\theta = 0^\circ$, and would not appreciably alter the spatial distribution of our modeled rates.

When the electromagnetic fields near Europa are treated as uniform, the corotating thermal plasma can impinge unimpeded onto the Moon’s upstream hemisphere. In this case, the spatial distribution of the thermal ion surface flux onto Europa’s upstream hemisphere (180° – 360° west longitude, Figure 5a) is mainly determined by the cosine of the angle between the normal vector at each surface location and the corotation direction (+ x , see also Equation 8 in Addison et al., 2021). This angle grows from 0° at the upstream apex to 90° at surface locations in the $x = 0$ plane (0° and 180° W longitudes, at all latitudes), and is rotationally symmetric around the x -axis. The surface flux of the impinging thermal ions therefore drops with distance from the upstream apex, as the angle between the corotation direction and the surface normal vector grows. This results in a bullseye-like flux pattern in the upstream hemisphere, as also found by Cassidy et al. (2013) and Addison et al. (2021).

The downstream hemisphere between $\lambda = -30^\circ$ and 30° latitude is mainly devoid of thermal ion influx, as many of the thermal ions are prevented access to this region by the solid body of Europa (Figure 5a). However, the thermal velocity of the corotating magnetospheric ions can achieve values of over 60% of the bulk speed u_0 (see Section 2.2). Thus, the velocity vectors of a significant number of thermal ions near the Moon are strongly inclined against the corotation direction. These ions are able to reach the high-latitude regions on Europa’s downstream hemisphere without being intercepted by the Moon’s upstream surface.

The sputtering rates R of thermal ions in uniform fields (Figure 6a) achieve their peak values (up to $R = 6 \times 10^{10} \text{ cm}^{-2} \text{ s}^{-1}$) on the upstream hemisphere, but are zero on the downstream hemisphere equatorward of $\pm 30^\circ$ latitude. However, unlike the thermal ion surface flux, the H_2O sputtering rate of thermal ions (Figure 6a) does *not* maximize near the upstream apex. Rather, the H_2O sputtering rate from thermal ion impacts grows monotonically with distance from the upstream apex and maximizes in the region where the $x = 0$ plane intersects Europa (dark red in Figure 6a). To explain this behavior, we consider ions whose velocity vectors are nearly aligned with the corotation direction, that is, ions which originate from the region of velocity space where the Maxwellian distribution peaks and the bulk of the upstream thermal population is concentrated. For such an ion, the impact angle θ in Equation 1 is approximately given by the angle between the corotation direction and the surface normal vector. The contribution that such an ion makes to the surface flux is proportional to $\cos(\theta)$, whereas the ion's sputtering yield is proportional to $\cos^{-f(m)}(\theta)$. The ion's contribution to the sputtering rate, which is the product of these two quantities, is therefore proportional to $\cos^{1-f(m)}(\theta)$. Since $f(m) > 1$ for all ion species (Famá et al., 2008), the sputtering rate of ions that move (nearly) along the corotation direction and impact the upstream hemisphere increases with distance from the upstream apex, that is, as the angle between the ion's velocity vector and the surface normal grows. This increase in sputtering rates with distance from the upstream apex is opposite to the pattern predicted by Cassidy et al. (2013) for uniform fields, as those authors treated all thermal ions as impacting the surface with the same incidence angle ($\theta = 0^\circ$) when calculating sputtering yields.

Including the influence of Europa's plasma interaction on magnetospheric ion trajectories drastically alters the spatial distribution of the thermal ion surface flux (Figure 5b). In this scenario, thermal ions no longer have unimpeded access to the Moon's upstream hemisphere. Deflection of thermal ions in the magnetic pileup region is too weak to appreciably reduce ion flux onto Europa's upstream hemisphere (Addison et al., 2021). Deflection of thermal ions away from the Moon is caused almost entirely by the Alfvén wings, which encapsulate Europa and its exosphere. The bulk of the thermal ions which enter Europa's interaction region are diverted around the Alfvén wing tubes, and pass by the Moon's sub-Jovian and anti-Jovian flanks (see also Figure 2 of Simon et al., 2021). Deflection of thermal ions around Europa's Alfvén wings reduces the ion surface flux by over an order of magnitude at nearly all locations on the upstream hemisphere (Addison et al., 2021). As shown by Simon et al. (2021), the small number of ions which penetrate the wing tubes move almost completely in the corotation direction, since the ionospheric Hall Effect is too weak at Europa to drastically break the symmetry of the ion flow pattern between the sub-Jovian and anti-Jovian hemispheres. In analogy to the case of uniform fields, the influx pattern of these ions onto the upstream hemisphere is therefore determined by the cosine of the angle between the corotation direction and the local surface normal. Hence, even when the field perturbations are taken into account, the spatial distribution of the thermal ion flux onto the upstream hemisphere retains something of the bullseye-like distribution seen in the case of uniform fields (Figure 5a). We note that the model of Simon et al. (2021) applies a fluid approach to describe ion dynamics. Hence, their model does not capture individual ions from the "edges" of the Maxwellian upstream distribution that impinge onto Europa at large angles against the corotation direction.

Although the bulk of the thermal ions move along the corotation direction, a non-negligible fraction of the upstream ions have velocity vectors which are significantly inclined against the corotation direction. These ions are deflected by the draped magnetic fields onto Europa's downstream and polar regions (Addison et al., 2021). The thermal ion flux onto the polar caps is therefore similar in magnitude to that at lower latitudes of the upstream hemisphere, except near the upstream apex where the thermal ion surface flux is higher by two orders of magnitude. The deflection of ions with highly inclined trajectories against the corotation direction onto the high-latitude regions leaves an equatorial depletion in flux by up to three orders of magnitude compared to the polar and low-latitude upstream regions (dark blue region in Figure 5b). This is in contrast to a uniform field geometry, where *no* thermal ions can reach the downstream hemisphere between approximately -30° and 30° latitude (white regions in Figure 5a).

The alterations to the thermal ion flux pattern brought on by the field perturbations carry over into the H_2O sputtering rates (Figure 6b). For perturbed fields, the spatial distribution of the rates from thermal ions sputtering is remarkably similar to the pattern seen in the thermal ion flux (Figure 5). Unlike in the case of uniform electromagnetic fields (Figure 6a), the H_2O sputtering rate for perturbed fields (Figure 6b) does indeed maximize near the trailing apex (270°W) in an elliptically shaped region which extends $\sim 45^\circ$ east and west of the upstream apex and 30° north and south. This elliptical region of enhanced H_2O sputtering corresponds to the ion surface flux enhancement centered near the upstream apex (Figure 5b). This enhancement possesses a minor east-west

asymmetry, which results from the (small) rotation of the electric field against the $-\hat{y}$ axis by the ionospheric Hall Effect. Simon et al. (2021) estimated that this angle of rotation may reach about 16° , consistent with the rather subtle east-west asymmetry in Figure 6b. The draping of the magnetic field lines allows thermal ions with a greater range of incidence angles to impinge upon each surface location on the upstream hemisphere, compared to when the fields are uniform. In particular, ions with grazing trajectories may impinge onto the surface near the upstream apex, while ions with trajectories normal to the surface may impact far from the upstream apex (see Figure 5 of Addison et al., 2021). As such, the increase in the H_2O sputtering rate with distance from the upstream apex seen in uniform fields (Figure 6a) does not occur when the field perturbations are included. In draped fields, the H_2O sputtering rate from thermal ions decreases with distance from the upstream apex, and falls off sharply upon entering the downstream hemisphere. The H_2O sputtering rate is two to three orders of magnitude lower on the downstream hemisphere than it is near the upstream apex. The near-equatorial depletion in thermal ion surface flux onto the downstream hemisphere (Figure 5b) causes a similar depletion in the H_2O sputtering rate at low latitudes. However, even near the downstream equator the sputtering rate obtained for perturbed fields still reaches $R \approx 10^6 \text{ cm}^{-2} \text{ s}^{-1}$. This is in contrast to a uniform field configuration, where the sputtering rate in this region is exactly zero (Figure 6a). Setting $\theta = 0^\circ$ in Equation 1 further reduces the H_2O sputtering rate from thermal ions by up to an order of magnitude (Figure 6c) to the minimum possible value. However, the spatial distribution largely remains unaffected compared to the rates obtained with the actual incidence angles (Figure 6b).

In a uniform field configuration, the surface flux of energetic ($5 \text{ keV} \leq E \leq 10 \text{ MeV}$) ions is nearly uniform across Europa's surface, differing between any two locations by no more than one order of magnitude (Figure 5c). The large gyroradii of energetic ions ($\approx 0.5R_E$ for 1 MeV S^{3+}) allow them to impact every location on Europa's surface, including the downstream hemisphere between -30° and 30° latitude which is inaccessible to the thermal ions in a uniform field setup (Figure 6a; Addison et al., 2021). The high field-aligned velocities of many energetic ions cause them to most heavily irradiate Europa's polar caps (Addison et al., 2021; Breer et al., 2019; Cassidy et al., 2013). As a result, the energetic ion surface flux monotonically decreases in the direction of descending latitude (Figure 5c), achieving a value at the equator that is roughly one order of magnitude lower than at the poles. A latitudinal decrease can also be seen in the H_2O sputtering rates of energetic ions in uniform fields (Figure 6d). Convection of energetic ions toward downstream leads to a slight enhancement in the energetic ion influx by $\sim 20\%$ near the upstream apex (Figure 5c) compared to the downstream equator. Thus, in the upstream hemisphere, the equatorial reduction in H_2O sputtering rate is interrupted by an elliptical enhancement of $\sim 20\%$ compared to the downstream equator.

Magnetic field line draping leads to a large, quasi-elliptical region of reduced energetic ion flux centered at Europa's upstream apex and covering much of the upstream hemisphere (see Figure 5d, as well as Addison et al., 2021). The draping increases the latitudinal extent of the region near the Moon where ions traveling along the field lines are within one gyroradius of the surface. Impinging ions can therefore gyrate into the Moon at higher latitudes than in uniform fields (Addison et al., 2021), creating an influx depletion by approximately a factor of 2 near the upstream apex compared to the downstream equatorial region. Surprisingly, a similar depletion feature is *not* present in the energetic ion H_2O sputtering rate calculated with draped fields and the actual incidence angles from GENTOO (Figure 6e). Although the energetic ion flux is reduced near the upstream apex by a factor of 3 compared to the poles (Figure 5d), ions entering the interaction region along the draped field lines (mostly) encounter the near-equatorial surface with grazing trajectories, that is, with incidence angles well over $\theta = 45^\circ$ (Addison et al., 2021; Breer et al., 2019). Such grazing impacts result in substantial sputtering yields around the upstream apex (Equation 1), overcompensating the drop in incident ion flux and producing a slight enhancement of the H_2O sputtering rates in that region.

To further illustrate this mechanism, Figure 7 displays maps of the average incidence angles of impinging sulfur ions exposed to Europa's perturbed electromagnetic environment, with energies of 10 keV (Figure 7a), 100 keV (Figure 7b), and 1 MeV (Figure 7c). It can be seen that these sulfur ions impact the surface with high incidence angles exactly in the regions where the ion influx is low (Figure 5d). The resultant high sputtering yields of these ions are able to replenish the upstream flux depletion revealed by Figure 5d. The result is that the energetic ion H_2O sputtering rate in the upstream hemisphere is similar for uniform and perturbed fields. However, the mechanism behind this similarity is highly intricate. In the case of uniform fields, the drift motion of the energetic ions along the corotation direction causes the surface flux near the upstream apex to be roughly 20% higher than at the downstream equator, which leads to a sputtering rate around the upstream apex that is similarly enhanced. In

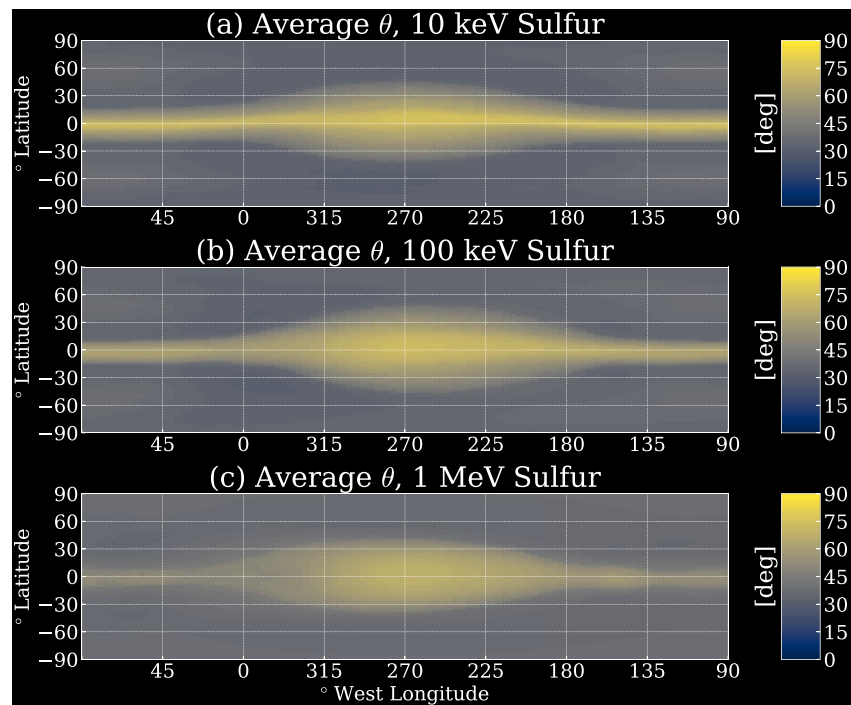


Figure 7. Maps of the average incidence angle $\langle \theta \rangle$ of (a) 10 keV, (b) 100 keV, and (c) 1 MeV S^{3+} ions with allowed trajectories, calculated with the perturbed electromagnetic fields from AIKEF.

contrast, field line draping *lowers* the flux near the upstream apex by a factor of 2. However, the grazing trajectories of energetic ions which impact these regions generate substantial sputtering yields and compensate for the low surface flux.

When a constant impact angle of $\theta = 0^\circ$ is used to calculate the H_2O sputtering yields (analogous to Cassidy et al., 2013), the depletion in energetic ion flux around the upstream apex (Figure 5d) maps into the H_2O sputtering rates (Figure 6f). In this case, the non-uniformity of ion incidence angles across Europa's surface is truncated, and the sputtering rates assume their minimum value (regarding the angle dependence) everywhere on the surface. Ions precipitating along grazing trajectories are thus not able to compensate for the upstream depletion in energetic ion flux. The result is an “inverted bullseye” distribution in the upstream hemisphere, where the sputtering rate grows with distance from the upstream apex (Figure 6f).

The H_2O sputtering rates of all ions and energies combined are shown in Figures 6g–6i. In the case of uniform electromagnetic fields (Figure 6g), the spatial distribution of the total H_2O sputtering rate is nearly rotationally symmetric about the x -axis, and maximizes near the $x = 0$ plane. The nearly homogeneous H_2O sputtering rate from energetic ions (second row of Figure 6) uniformly augments that from thermal ions at all locations. Without the field perturbations, energetic ions are the sole agents of H_2O sputtering on the downstream hemisphere between approximately -30° and 30° latitude (which is inaccessible to upstream thermal ions in the case of uniform fields, see Figure 5a). The H_2O sputtering rate on the downstream hemisphere is a factor of 2–3 less than the maximum value on the upstream hemisphere. When the fields are treated as uniform, H_2O sputtering from thermal ions dominates at every point on the surface except mid-to-low latitudes on the downstream hemisphere (first column in Figure 6).

However, with perturbed fields, the quasi-uniform H_2O sputtering rate from energetic ions exceeds that from thermal ions at nearly every surface location except near the upstream apex (Figures 6b and 6e). The map of the total H_2O sputtering rate from all ions and energies combined (Figure 6h) therefore closely resembles the nearly featureless pattern caused by energetic ion sputtering alone (Figure 6e). Comparison of Figures 6b and 6e reveals that the contribution of thermal ions to the total H_2O sputtering rate equals that of the energetic ions only near the upstream apex, effectively doubling the energetic H_2O sputtering rate there (red region in Figure 6h). This preferential emission of H_2O molecules near the upstream apex agrees well with a recent study by Roth (2021),

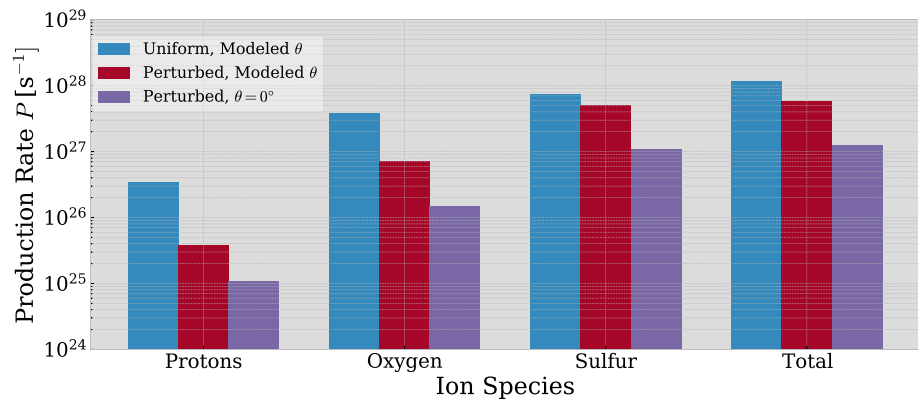


Figure 8. Total H₂O production rate P for all ion energies and species modeled in this study. From left to right, production rates of incident hydrogen, oxygen, sulfur, and the combined production rates of all ion species are shown. The production rates calculated with uniform and perturbed electromagnetic fields are displayed in blue and red, respectively, both with sputtering yields calculated using the actual incidence angles from GENTOO in Equation 1. Purple bars indicate production rates calculated with perturbed fields and the incidence angles of all impinging ions set to $\theta = 0^\circ$ in Equation 1.

who used observed emission rates from HST to surmise the presence of a stable, localized H₂O component of the exosphere above Europa's central trailing hemisphere.

For each species, the total amount of H₂O sputtered from Europa's surface per time via magnetospheric ion impacts at all energies, P , is given by

$$P(m, Z) = R_E^2 \int_{-\pi/2}^{\pi/2} \int_0^{2\pi} R(m, Z, \lambda, \phi) \cos(\lambda) d\phi d\lambda, \quad (6)$$

where $R(m, Z, \lambda, \phi)$ is the H₂O sputtering rate of a given species at a particular surface location (λ, ϕ) . The resulting production rates from protons, oxygen ions, sulfur ions, and all ion species combined are displayed in Figure 8. Blue bars indicate production rates calculated with uniform electromagnetic fields and the incidence angles obtained from GENTOO, red bars indicate production rates calculated with perturbed fields and incidence angles from GENTOO, and purple bars show production rates calculated with perturbed fields and θ set to 0° in Equation 1 for all precipitating ions.

In all three setups presented in Figure 8, sulfur ions sputter the most H₂O per second, while oxygen ions and protons sputter successively less. This trend follows the hierarchy of the sputtering yield curves shown in Figure 1a, revealing that the yields (not the surface fluxes) are the most important factor in determining the relative H₂O sputtering rate contributions between ion species. As shown by Addison et al. (2021), the surface fluxes of hydrogen ions exceed those of the two heavy ion species by up to an order of magnitude. However, due to their low mass, hydrogen ions play a negligible role in the sputtering of H₂O from Europa's surface (see Figure 1a). The surface fluxes of sulfur and oxygen ions differ by no more than a factor of 5 (Addison et al., 2021). However, since the sputtering yields of sulfur ions may exceed those of oxygen ions by over an order of magnitude (see Figure 1a), sulfur makes the largest contribution to the total H₂O production rate. In the case of uniform fields (blue bars in Figure 8), sulfur ions sputter roughly twice as much H₂O per second as oxygen ions ($P \approx 7 \times 10^{27} \text{ s}^{-1}$ vs. $P \approx 4 \times 10^{27} \text{ s}^{-1}$, respectively). Hydrogen ions sputter an order of magnitude less H₂O than either of the heavy ion species. We calculate a total H₂O production rate (from all three species) of $P_T = 1.16 \times 10^{28} \text{ s}^{-1}$ in a uniform field configuration. Energetic sulfur ions generate the most H₂O per second (42% of P_T), while thermal oxygen ions generate the second most (31%). Cassidy et al. (2013) found the same hierarchy of sputtering agents from their calculation of the total sputtering rates in uniform fields and with $\theta = 0^\circ$ for all impinging ions (63% from energetic sulfur, 19% from thermal oxygen).

The H₂O production rate from sulfur ion impacts is reduced by only 10% when the field perturbations are considered, while the production rates associated with oxygen and hydrogen ions each fall by almost an order of magnitude (red bars, Figure 8). This discrepancy can be understood by isolating the contribution of the thermal and energetic regimes to each species' sputtering rate with perturbed fields. The high sputtering yields of sulfur

ions in the energetic regime (Figure 1a) allow the production rate from energetic sulfur ions ($P = 4.9 \times 10^{27} \text{ s}^{-1}$) to exceed that from the thermal sulfur ions ($P = 2.5 \times 10^{26} \text{ s}^{-1}$) by over an order of magnitude, despite the energetic sulfur ion surface flux being an order of magnitude lower (Addison et al., 2021). For oxygen, thermal ions produce 50% more H_2O per second than energetic ions ($P = 4.38 \times 10^{26} \text{ s}^{-1}$ vs. $P = 2.9 \times 10^{26} \text{ s}^{-1}$, respectively). The discrepancy for hydrogen ions is even more stark: thermal protons produce $P = 3.58 \times 10^{25} \text{ s}^{-1}$, while energetic protons produce only $P = 2.3 \times 10^{24} \text{ s}^{-1}$. In other words, sulfur is the only ion species that causes higher H_2O production rates in the energetic regime than in the thermal regime. Since the sputtering rates of energetic ions are much less affected by the perturbed fields (Figure 6), the sulfur ion contribution to the total production rate is much more “resilient” to the inclusion of the field perturbations than the contributions from hydrogen or oxygen, whose production rates are dominated by the thermal ions.

Of the thermal ion contribution to the total H_2O production rate P_T in perturbed fields, sulfur ions constitute 35%, oxygen ions constitute 60%, and protons add 5%. These values are in rough agreement with the 21%, 78%, and <1% contributions (for thermal sulfur, oxygen, and hydrogen ions, respectively), found by Cassidy et al. (2013) with uniform fields. The dominance of H_2O sputtering by thermal oxygen ions over the contribution from thermal sulfur stems from the slightly higher surface flux of oxygen (Addison et al., 2021). In the energetic regime, we find that sulfur ions contribute ~94% of H_2O production in perturbed fields, while oxygen ions and protons add 6% and <1%, respectively. The total production rate from all ions falls by about 50% to a value of $P_T \approx 5.9 \times 10^{27} \text{ s}^{-1}$ when the field perturbations are included (blue vs. red bars in the right-most block of Figure 8). Setting the incidence angles of all impinging ions to $\theta = 0^\circ$ in Equation 1 further reduces the H_2O production rate by a factor of 2–5, depending upon the ion species (purple bars in Figure 8). The total H_2O production rate from all ion species in the case of perturbed fields and $\theta = 0^\circ$ falls to $P_T = 1.27 \times 10^{27} \text{ s}^{-1}$, which is a factor of 5 smaller than the rate calculated with the actual incidence angles from GENTOO.

Thus, inclusion of the perturbed fields reduces the total H_2O production rate at Europa by at least a factor of 2 compared to uniform fields (rightmost block in Figure 8). In addition, the perturbed fields significantly modify the spatial distribution of the H_2O sputtering rates (Figure 6). When the electromagnetic fields near Europa are treated as uniform, the corotating thermal plasma is unable to sputter material from the Moon’s low-latitude downstream hemisphere, and the H_2O sputtering rate maximizes near the meridian through the Moon’s sub-Jovian and anti-Jovian apices. With the inclusion of the magnetospheric field perturbations, the distribution of the H_2O sputtering rate becomes much more homogeneous, besides a localized enhancement by up to an order of magnitude near the upstream apex. Except for this narrow region, the quasi-uniform H_2O sputtering rate of the energetic ions exceeds that of the thermal ions at every surface location. Therefore, in draped fields the energetic ions are able to “smear out” many of the non-uniformities in the thermal ion H_2O sputtering rate pattern.

3.3. Sputtering Rates of O_2 and H_2

We now investigate the temperature-dependent sputtering rates of O_2 and H_2 over the course of an European day (≈ 80 hr), that is, as the sub-solar point moves across the Moon’s surface. Maps of the H_2 sputtering rates will be qualitatively identical to those of O_2 , since H_2 sputtering rates are twice those of O_2 (Equation 4). Therefore, for most of this section we will restrict our discussion to O_2 sputtering rates. In Section 3.3.1 we present sputtering rates calculated with the O_2 sputtering yield model of Teolis et al. (2017), that is, with the assumption that the O_2 is concentrated in a “thin layer” $\sim 28 \text{ \AA}$ in depth (dash-dotted lines in Figures 1b and 1c). In Section 3.3.2 we investigate O_2 sputtering rates calculated with a “thick layer” model, that is, with the assumption that the O_2 -bearing layer within Europa’s surface extends to any depth to which a magnetospheric ion may penetrate. This model is shown as solid lines in Figures 1b and 1c, and is adopted from Plainaki et al. (2013). In Section 3.3.3 we compare the total production rates of O_2 from both models, and discuss their implications for the generation of Europa’s exosphere.

3.3.1. Contributions of Thermal and Energetic Ions in a “Thin Layer” Model

Figure 9 shows O_2 sputtering rates from thermal (first column) and energetic (second column) ions impinging upon a thin O_2 layer, that is, calculated with Equations 3 and 5. To isolate the effect of a non-uniform temperature profile on the O_2 sputtering rates, the first row in Figure 9a and 9b displays the spatial distribution of the O_2 sputtering rates calculated with a uniform surface temperature of $T = 93 \text{ K}$. This value of T was derived by averaging the diurnal temperature profile shown in Figure 3. In the case of a uniform surface temperature, $\Phi(T)$

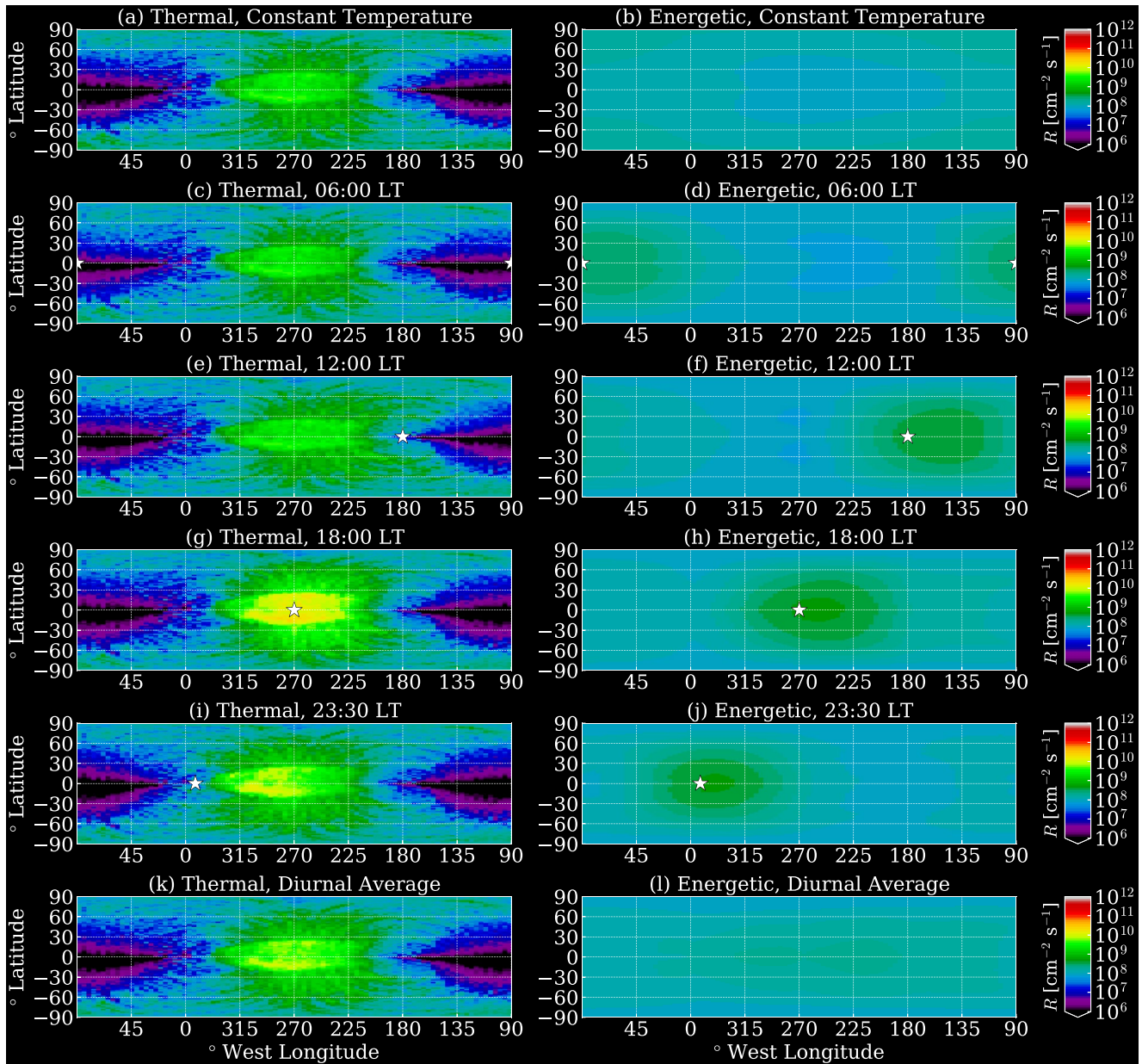


Figure 9. Maps of the O_2 sputtering rates from all ion species considered in this study, calculated with the perturbed electromagnetic fields from AIKEF and the actual incidence angles from GENTOO. The sputtering yields were calculated with a “thin layer” model of the oxygen-bearing surface layer (Teolis et al., 2017), that is, with Equation 5. The first column (a), (c), (e), (g), (i), and (k) displays the O_2 sputtering rates from thermal ion impacts, while the second column (b), (d), (f), (h), (j), and (l) shows O_2 sputtering rates from energetic ion impacts. To establish a “baseline” for our analysis, the first row (a) and (b) presents O_2 sputtering rates calculated with a uniform surface temperature of $T = 93$ K. The next four rows show maps of the sputtering rates for different orbital positions of Europa, as illustrated in Figure 2: 06:00 LT (c) and (d), 12:00 LT (e) and (f), 18:00 LT (g) and (h), and 23:30 LT (i) and (j). In the plots which depict a specific local time (c)–(j), a white star is shown to denote the sub-solar point on Europa’s surface. *Note.* That in (c) and (d), the star is divided between the leftmost and rightmost edges of the surface maps. The final row (k) and (l) presents maps of the O_2 sputtering rates calculated with a diurnally averaged temperature profile (see Figure 3).

in Equation 5 assumes the same constant value at all surface locations, that is, the temperature dependence of the sputtering yields does not generate any changes to the spatial distribution of the O_2 and H_2 sputtering rates. The middle four rows (Figure 9c–9j) present maps of the O_2 sputtering rates at the four local times for which temperature maps have been provided in Figure 2. The final row (Figure 9k and 9l) shows O_2 sputtering rates calculated with the diurnally averaged temperature profile presented in Figure 3.

All sputtering rates shown in Figure 9 were calculated with the perturbed fields from AIKEF: the necessity to include these perturbations has been demonstrated in Section 3.2 and numerous preceding publications. The angular dependence for O_2 in a thin layer model (Teolis et al., 2017) is given by $(1 - \exp[-r_0(E)\cos(\theta)/x_0]) \cos^{-1}(\theta)$, see Equation 5. Within the range of $r_0(E)$ values used in our study, this term always results in an increase in O_2 sputtering yields with increasing incidence angle, similar to H_2O . Therefore, in analogy to H_2O (middle vs. right columns of Figure 6), inclusion of the incidence angles from GENTOO (instead of a constant value) is expected to cause only subtle differences in the spatial distribution of the O_2 sputtering rates, and will not alter the relative contributions of thermal and energetic ions. Hence, for our calculation of O_2 sputtering rates we utilize the modeled incidence angles from GENTOO in Equation 5.

The first column of Figure 9 reveals that the O_2 sputtering rate from thermal ions peaks near the upstream apex, where the thermal ion flux is largest, and decreases with distance from the upstream apex as the surface influx drops (Figure 5b). The downstream hemisphere at low latitudes experiences substantially less O_2 sputtering from thermal ions, with a sputtering rate three to four orders of magnitude lower than on the upstream hemisphere. Since the sputtering yields of H_2O and O_2 both grow monotonically with increasing incidence angle, the O_2 sputtering rate pattern from thermal ions resembles that of H_2O (Figure 6).

Changes in the orientation between the incoming solar radiation (and thus the surface temperature profile) and the upstream plasma flow cause slight qualitative modifications to the spatial distribution of the O_2 sputtering rate from thermal ions (Figures 9c, 9e, 9g, and 9i), compared to the “baseline” case of a constant surface temperature (Figure 9a). Within the range of surface temperatures present at Europa (≈ 60 – 140 K, see Figure 2), the temperature-dependent term $\Phi(T)$ in Equation 5 ranges from $\sim 10^{-2}$ to 7. As such, variations in the surface temperature profile along Europa’s orbit can (at most) enhance the O_2 sputtering rate at a given point by a factor of 8. Since the thermal ion surface flux varies by more than three orders of magnitude between surface locations, the shifting of the surface temperature profile along Europa’s orbit is not sufficient to qualitatively alter the O_2 sputtering rate maps from thermal ions when the oxygen-bearing surface layer is thin.

For each of the orbital positions shown in Figure 9, the O_2 sputtering rates drop slightly with increasing latitude, since Europa’s polar caps are consistently cold (Figures 2 and 3). Movement of the sub-solar point (denoted by a star in the plots) across Europa’s surface quantitatively enhances the sputtering rate by a factor of 4–7, which is insufficient to noticeably alter the spatial distribution (left column of Figure 9). When the upstream apex and sub-solar point are coincident at 18:00 LT, the O_2 sputtering rate from thermal ions near the upstream apex maximizes, as the thermal plasma directly impinges upon the hottest region of the Moon’s surface (see also Figure 2). The surface near the sub-solar point in this configuration is hotter than at any other local time, since the low albedo at 18:00 LT causes it to heat to a maximum temperature that is roughly 15% higher than when the sub-solar point is located on the downstream hemisphere (06:00 LT). At 12:00 and 23:30 LT the sub-solar point is located near the Moon’s anti-Jovian and sub-Jovian apices, respectively (Figures 9e and 9i), and the upstream enhancement in O_2 sputtering rates is slightly “pulled” toward the sub-solar point, where the temperature and the resultant sputtering yields maximize. At these two orbital positions, the sub-solar enhancement in surface temperature, and therefore the enhancement in O_2 sputtering rates, is roughly a factor of 2 less than at 18:00 LT (Figure 9g).

Figure 9k displays the O_2 sputtering rate from thermal ions calculated with a diurnally averaged surface temperature profile (shown in Figure 3). The dichotomy in the surface temperatures between the upstream and downstream hemisphere in this case causes the map of the thermal ion O_2 sputtering rate to qualitatively resemble that at 18:00 LT (Figure 9g), although the upstream enhancement is a factor of 2 weaker. When the oxygen-bearing surface layer is thin, the chosen surface temperature profile does not significantly alter the map of the O_2 sputtering rate from thermal ions. Regardless of the temperature profile, the maps of the sputtering rates display similar patterns as the influx map for thermal magnetospheric ions (Figure 5b).

In contrast, the spatial distribution of the O_2 sputtering rate from energetic ion impacts is largely determined by the surface temperature profile, that is, by the orientation of the Sun relative to Europa. The energetic ion sputtering rate for a constant surface temperature (Figure 9b) is nearly homogeneous, never varying between any two surface locations by more than a factor of 2. A global minimum in the O_2 sputtering rate from energetic ions is present near the upstream apex, with the rate reduced by 35% compared to that near the poles (Figure 9b). Above incident ion energies of $E = 10$ keV, the penetration depths of the ions are greater than the O_2 layer depth ($x_0 = 28 \text{ \AA}$) even at an extreme grazing incidence of $\theta = 80^\circ$ (Teolis et al., 2017; Ziegler & Manoyan, 1988). The

angle-dependent exponential term in Equation 5 is therefore nearly zero, and the sputtering yield is proportional to $\cos^{-1}(\theta)$. Hence, the O_2 sputtering yields around the upstream apex are less amplified by high incidence angles compared to the H_2O yields, which are proportional to $\cos^{-f(m)}(\theta)$ with $f(m) > 1$ for all ion species. For example, the H_2O sputtering yield of a $\theta = 80^\circ$ incident sulfur ion is enhanced by a factor of ≈ 21 compared to normal incidence ($\theta = 0^\circ$), while the O_2 yield of the same projectile would only be enhanced by a factor of ≈ 6 . As a result, the sputtering yields due to grazing impacts of energetic ions near the upstream apex are no longer able to compensate for the upstream flux depletion (Figure 5d), resulting in a net drop of the sputtering rate around the upstream apex. However, this upstream drop in the energetic ion O_2 sputtering rates is much smaller than the variability associated with the range of European surface temperatures.

At all four local times considered (Figures 9d, 9f, 9h, and 9j), a quasi-elliptical enhancement in the O_2 sputtering rate forms near the sub-solar point. In each case, the maximum of the O_2 sputtering rate from energetic ions is displaced somewhat to the east of the sub-solar point, since the thermal inertia of Europa's surface slightly delays the surface heating. With a diurnally averaged temperature profile, the map of the O_2 sputtering rates from energetic ions (Figure 9l) is nearly homogeneous, since the temperature enhancement covers a wider range of surface longitudes on the upstream hemisphere (see Figure 3).

In contrast to the case of sputtered H_2O , thermal ions dominate the O_2 sputtering rate at almost every location on Europa's upstream hemisphere (180° – 360° W longitude), regardless of the surface temperature profile (Figure 9). While the H_2O sputtering yields of heavy ions grow by three to four orders of magnitude in the energetic regime compared to the thermal regime (Equation 1; Figure 1a), the respective O_2 yields increase by no more than two orders of magnitude. The energetic ions still penetrate more deeply into the surface than thermal ions. However, this increased penetration is largely ineffective at producing additional O_2 in the “thin layer” picture of Teolis et al. (2017), since the O_2 surface concentration quickly drops at greater depths. Thus, the O_2 sputtering yields of the energetic ions are insufficient for their sputtering rates to overcome those of the thermal ions on the upstream hemisphere, and the thermal ion O_2 sputtering rate dominates. This does not hold for the downstream hemisphere, however, where the thermal ion surface flux and the associated sputtering rates are several orders of magnitude lower than those of energetic ions. However, the energetic ion sputtering rate on the downstream hemisphere is still one to two orders of magnitude weaker than the upstream maximum.

3.3.2. Contributions of Thermal and Energetic Ions in a “Thick Layer” Model

Figure 10 displays O_2 sputtering rates calculated with a “thick layer” model of the sputtering yields (Plainaki et al., 2013), that is, with the assumption that the thickness of the O_2 -bearing layer within Europa's surface exceeds the penetration depth of any incident magnetospheric ion. The associated yields are given in Equation 2 and shown as solid lines in Figure 1b.

The assumption of a thick oxygen-bearing surface layer does not significantly alter the qualitative distribution of the O_2 sputtering rates from thermal (left column of Figure 10) or energetic (right column of Figure 10) ions compared to when a thin layer is assumed (Figure 9). Recall that O_2 yields in both a thick-layer model and a thin-layer model grow with incidence angle, similar to the yields of H_2O . Therefore, the quantitative behavior of the O_2 sputtering rates with respect to incidence angle is the same as for the H_2O rates, regardless of O_2 layer thickness.

The difference between the temperature-dependent terms of the two O_2 sputtering models (thin layer and thick layer) becomes significant in regions of low surface temperatures, especially the polar caps. With a thin oxygen-bearing layer (Teolis et al., 2017), the temperature dependence takes the form of $1 + \Phi(T)$, while with a thick layer (Plainaki et al., 2013) the dependence is given by only $\Phi(T)$. Thus, in both models the O_2 yields are independent of temperature below ~ 70 K, grow monotonically with temperature above 70 K, and eventually stagnate at very high temperatures. At the hottest regions of Europa's surface, the temperature dependencies of both models augment the sputtering yields by nearly the same factor. However, at low temperatures ($\Phi(T) \approx 0$), the O_2 sputtering yields of Plainaki et al. (2013) approach a value of zero, while those of Teolis et al. (2017) approach a nonzero value. This discrepancy at low temperatures causes the two models to produce vastly different sputtering rates in cold surface regions (below 70 K). Since Europa's surface temperature (Figures 2 and 3) drops by a factor of 2 from the equator (100–140 K) to the poles (≈ 60 K), the O_2 sputtering rates from thermal ions calculated with a thick oxygen-bearing layer fall by up to five orders of magnitude from the upstream equator to the poles (Figures 10c, 10e, 10g, 10i, and 10k). In contrast, with a thin oxygen-bearing layer (Figure 9) the difference between the O_2 sputtering rates of thermal ions at the equator and the poles at any local time is limited

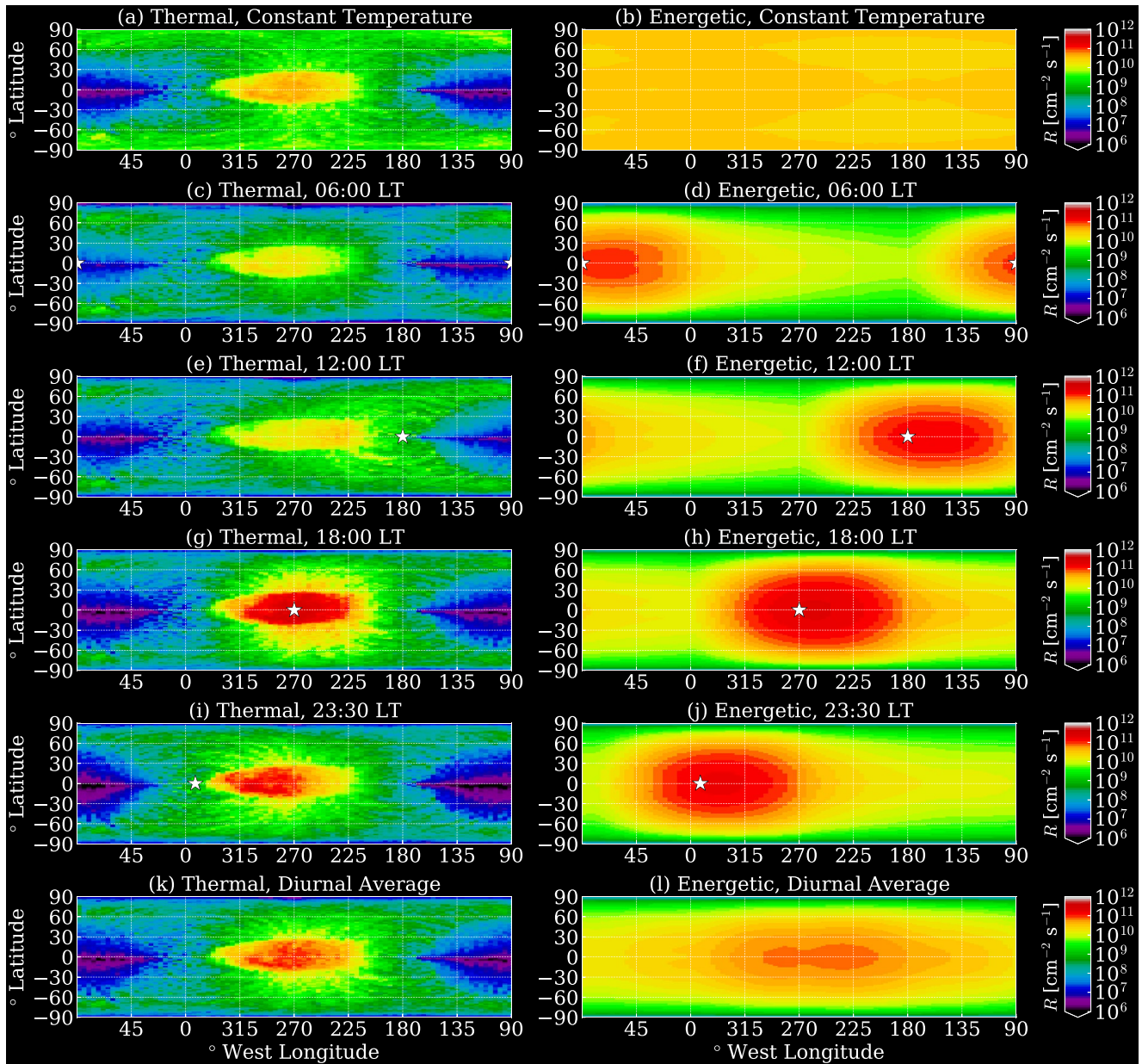


Figure 10. Maps of the O_2 sputtering rates from all ion species considered in this study, calculated with the perturbed electromagnetic fields from AIKEF and the actual incidence angles from GENTOO. The sputtering yields were calculated with a “thick layer” model of the surface oxygen (Plainaki et al., 2013), that is, with Equation 2, depicted as solid lines in Figure 1b. The layout of the panels is identical to Figure 9.

to around three orders of magnitude. In the (hypothetical) case of a constant, averaged surface temperature the O_2 sputtering rates of thermal ions fall by at most two orders of magnitude from the equator to the poles (Figure 10a), and this decrease is caused purely by non-uniformities in the ion influx pattern. O_2 sputtering rates from energetic ions feature a similar behavior, falling by up to four orders of magnitude from the equator to the poles when a non-uniform temperature profile is included (Figures 10d, 10f, 10h, 10j, and 10l). In contrast, the O_2 sputtering rates of energetic ions calculated with a constant temperature profile (Figure 10b) do not decrease with increasing latitude. The consistently low temperatures of Europa’s polar caps are therefore crucial to understanding exospheric generation at high latitudes.

In contrast to the thin layer model (Teolis et al., 2017), energetic ions in the thick layer model (Plainaki et al., 2013) can eject O_2 along their entire trajectory through the surface ice. As such, the O_2 sputtering yields of these ions

dwarf those of the thermal ions by up to three orders of magnitude (Figure 1b). Hence, the O₂ sputtering rates of energetic ions in the picture of Plainaki et al. (2013) exceed those of the thermal ions at nearly every surface location, regardless of the temperature profile (Figure 10). When the thick layer approach is used, the “roving” enhancement in energetic ion sputtering rates which follows the sub-solar point slightly exceeds that due to preferential thermal ion bombardment at the upstream apex.

The sputtering yields of thermal heavy ions in a thick layer approach exceed those in a thin layer approach by nearly an order of magnitude (solid vs. dash-dotted lines, Figure 1b). As can be seen from the left columns in Figures 9 and 10, this leads to the O₂ sputtering rates of thermal ions in a thick layer model surpassing those in a thin layer model by roughly an order of magnitude at almost every surface location. The deviation in the O₂ sputtering yields and rates of energetic ions between the two models is much more drastic, with the rates in a thick layer model typically exceeding those in a thin layer model by two to three orders of magnitude.

3.3.3. Total Sputtering and Neutral Gas Production Rates

Presented in Figure 11 are maps of the total O₂ sputtering rates from ions of all species and energies considered in this study. Rates calculated with the thin layer model of the O₂ sputtering yields (Teolis et al., 2017) are displayed in the first column, while results from the thick layer model (Plainaki et al., 2013) are shown in the second column. Similar to Figures 9 and 10, each row corresponds to a specific surface temperature profile, with the first row representing a constant, averaged temperature of $T = 93$ K at all surface points, the next four rows corresponding to specific local times, and the final row denoting rates calculated with a diurnally averaged temperature profile (Figure 3).

In the upstream hemisphere, the total O₂ sputtering rates calculated with a thin oxygen-bearing layer (left column of Figure 11) closely resemble the thermal ion rates (left column of Figure 9). The downstream depletion in the thermal ion sputtering rate is “filled in” by the energetic ion contribution (right column of Figure 9 and left column of Figure 11). Thus, the thermal ion contribution to O₂ sputtering dominates that of energetic ions on the upstream hemisphere, while the energetic ion contribution exceeds that of the thermal ions on much of the downstream hemisphere. This is in contrast to the H₂O sputtering rate pattern, where the nearly homogeneous energetic ion sputtering rate dominates the thermal ion contribution at all surface locations except for a narrow region near the upstream apex (Figure 6h), since for H₂O the energetic ion sputtering yields exceed those of thermal ions by several orders of magnitude.

The region of maximum O₂ generation in the thin layer approach is always located near the upstream apex, regardless of the solar orientation. Depending on the local time, the center of this enhancement is slightly displaced in longitude toward the sub-solar point (Figures 11e and 11i), as long as the sub-solar point is not located on the downstream side of the Moon (Figure 11c). The maximum O₂ sputtering rate in the upstream hemisphere calculated with a thin oxygen-bearing layer ranges from $R = 5.1 \times 10^9$ cm⁻² s⁻¹ at 06:00 LT to $R = 2.5 \times 10^{10}$ cm⁻² s⁻¹ at 18:00 LT.

For a thin layer model, the diurnally averaged temperature profile yields a maximum O₂ sputtering rate (reached near the upstream apex) of approximately $R = 1.1 \times 10^{10}$ cm⁻² s⁻¹, a factor of 4 lower than predicted for uniform fields by Cassidy et al. (2013). These authors also utilized a diurnally averaged temperature profile and a thin O₂-bearing layer. However, Cassidy et al. (2013) treated all impinging ions as impacting normal to the surface ($\theta = 0^\circ$). Therefore, these authors’ sputtering rates constitute the minimum value possible with their choice of magnetospheric parameters (see also Equation 5). If Cassidy et al. (2013) had utilized actual incidence angles instead, their sputtering rates would be higher, and the discrepancy between their rates for uniform fields and those calculated here for draped fields would be even greater. The low sputtering rates obtained for draped fields in our model are consistent with the idea that the perturbations to the electromagnetic fields partially shield Europa’s surface from magnetospheric ion bombardment (Addison et al., 2021; Breer et al., 2019; Harris et al., 2021; Simon et al., 2021).

Using a thin layer, our model predicts a minimum O₂ sputtering rate near the downstream apex (90°W) of $R \approx 10^8$ cm⁻² s⁻¹. While this value is roughly two orders of magnitude lower than the peak value near the upstream apex, the occurrence of such substantial surface erosion in Europa’s downstream hemisphere is in stark contrast to the results of Cassidy et al. (2013). Using uniform fields, these authors predicted a minimum sputtering rate of nearly zero on almost the *entire* downstream hemisphere (see Figure 9 of Cassidy et al., 2013). Therefore, if Europa’s electromagnetic environment were perfectly uniform, any O₂ gas located above the downstream

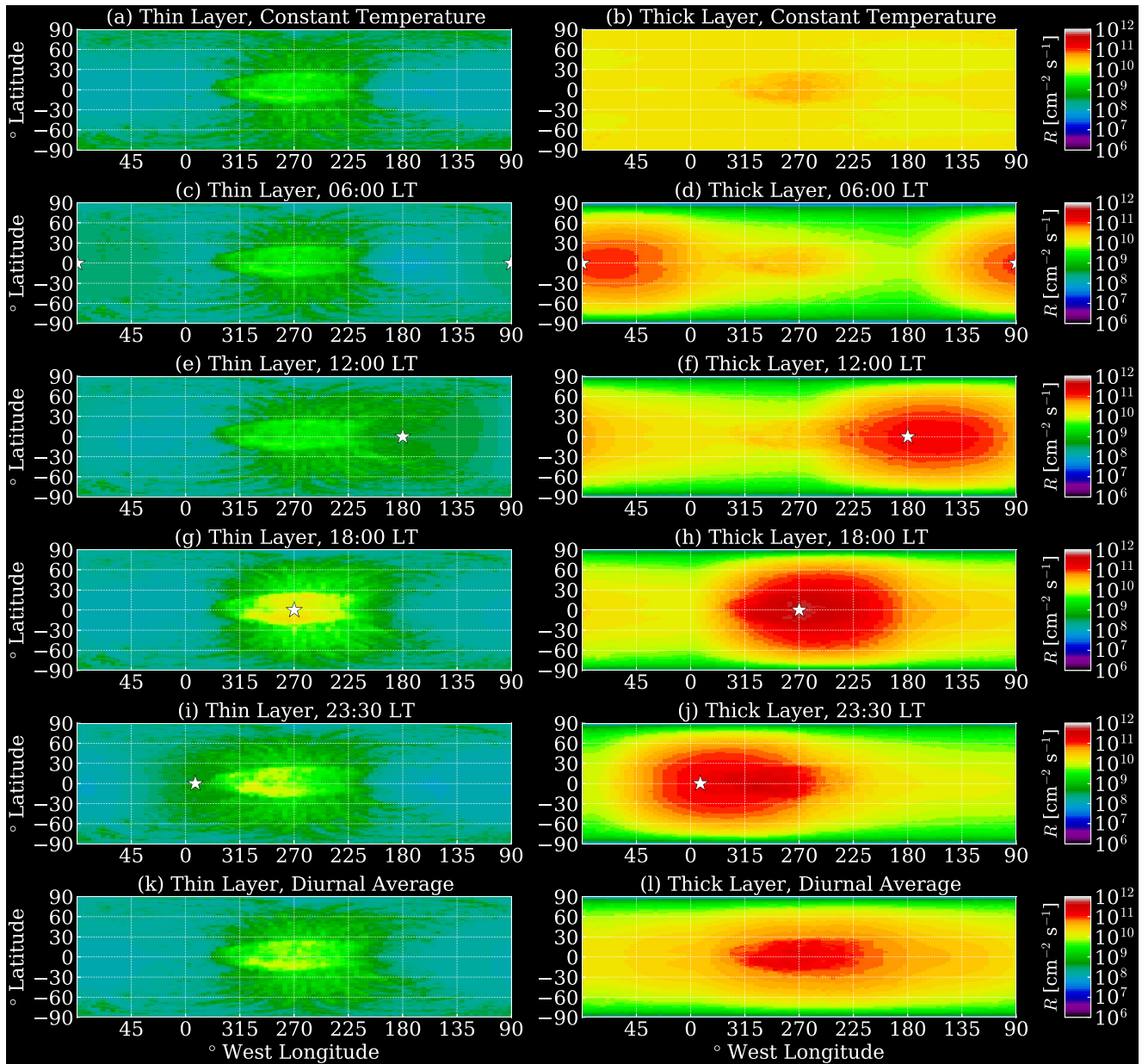


Figure 11. Maps of the total O_2 sputtering rates from all ion species and energies considered in this study, calculated with the perturbed electromagnetic fields from AIKEF and the actual incidence angles from GENTOO. In the first column (a), (c), (e), (g), (i), and (k) are presented the O_2 sputtering rates calculated with a “thin layer” model of the surface oxygen (Equation 5), while the second column (b), (d), (f), (h), (j), and (l) shows O_2 sputtering rates from a “thick layer” model (Equation 2). The rows represent different surface temperature profiles, following the layout of Figures 9 and 10.

hemisphere would have to be transported there from the upstream hemisphere through, for example, Coriolis or centrifugal forces (Oza et al., 2019). However, with the inclusion of the perturbed fields in our model, O_2 gas can be produced directly in the downstream hemisphere. As can be seen from the right column of Figure 11, this effect is amplified when the surface oxygen is assumed to occupy a thick layer (Plainaki et al., 2013).

In the thick layer picture, the energetic ions have substantial sputtering yields compared to a thin layer approach (right columns of Figures 9 and 10). This allows the energetic ions to become the dominant agents in determining the spatial distribution of the O_2 source rate at Europa. When the surface temperature is treated as constant (Figure 11b), the O_2 yields in a thick layer approach are simply the H_2O yields multiplied by the same, constant coefficient at every surface location (Equation 2). Therefore, if the surface temperature were uniform, the spatial

distribution of the O_2 sputtering rate would be largely homogeneous across Europa's surface, with the bullseye-like "surplus" of thermal ion influx near the upstream apex (red in Figure 5b) generating the only significant local enhancement.

When a non-uniform temperature profile is used to calculate the O_2 sputtering yields for a thick oxygen-bearing layer, the spatial distribution of the energetic ion O_2 sputtering rate demonstrates a quasi-elliptical enhancement by a factor of 5 around the sub-solar point (Figures 10d, 10f, 10h, and 10j). Since in this case the O_2 sputtering rates from energetic ions exceed those from thermal ions at nearly every surface point, this sub-solar augmentation is also clearly visible in the total O_2 rate maps (right column of Figure 11). At 06:00 LT (Figure 11d), this results in two distinct O_2 sputtering maxima on Europa's surface: the more pronounced one is centered near the sub-solar point at $90^\circ W$, whereas the fainter one (originating from the preferential precipitation of thermal ions near the upstream apex) is located near the upstream apex at $270^\circ W$. These two enhancements are still discernible, but also have substantial overlap at 12:00 and 23:30 LT (red regions in Figures 11f and 11j), since the sub-solar point is located only $\sim 90^\circ$ in longitude from the upstream apex. At 18:00 LT, the sub-plasma and sub-solar points are coincident, resulting in a single, quasi-elliptical enhancement by approximately an order of magnitude compared to the downstream apex. This enhancement ($R \approx 5 \times 10^{11} \text{ cm}^{-2} \text{ s}^{-1}$) is over an order of magnitude greater than the maximum sputtering rate calculated with a thin layer at 18:00 LT, and marks the maximum O_2 sputtering rate at any point along Europa's orbit.

If the sputtering maxima from a thick layer model directly translated into local enhancements of the exospheric column density, this would imply that there may be two distinct "bulges" in Europa's neutral gas envelope: a minor enhancement persistently located near the upstream apex, and a more pronounced increase that follows the region of greatest solar irradiation. This is in contrast to the results for a thin oxygen-bearing layer model, which predicts only one emission maximum for O_2 molecules, consistently located near the upstream apex. However, investigating any potential exospheric asymmetries requires to take into account all relevant influences on the dynamics of the emitted gas molecules (e.g., gravitational and fictitious forces, collisions, and ionization). Such an effort is beyond the scope of this study.

The total O_2 production rates P from ions of all species and energies considered in this study are presented in Figure 12 for each of the five non-uniform temperature profiles shown in Figure 11. We do not include the case of a uniform surface temperature profile, as we do not expect this approach to generate accurate sputtering rates for Europa's nightside hemisphere. Figure 12a displays production rates calculated with a thin O_2 -bearing surface layer (Equation 5). Averaged across all four local times shown in Figure 12a, oxygen ions produce roughly the same amount of O_2 as sulfur ions (the averaged rates differ by only $\approx 30\%$), whereas sulfur ions sputter nearly seven times more H_2O than oxygen ions (Figure 8). Regardless of the chosen sputtering model, the surface flux and O_2 sputtering yields of the two heavy ion species are very similar in the thermal regime. Since thermal ions dominate the O_2 sputtering rate in a thin layer model, the contributions of the two heavy ion species are nearly the same.

However, if the O_2 -bearing surface layer is assumed to be thick (Figure 10), energetic ions make the greatest contribution to the total O_2 sputtering rates at nearly every location on the surface. Hence, sulfur ions, which dominate the O_2 sputtering yields in the energetic regime by up to an order of magnitude over oxygen ions (solid lines in Figure 1b), surpass the production rates of oxygen ions by at least an order of magnitude regardless of the temperature profile (second vs. third block in Figure 12b). Sulfur ions in a thick layer configuration (Figure 12b) produce approximately two orders of magnitude more O_2 per second than when the O_2 -bearing layer is thin (Figure 12a), while the discrepancies for oxygen and hydrogen ions are roughly an order of magnitude and a factor of 2–5, respectively. Thus, the thickness of the oxygen-bearing layer beneath Europa's surface has a measurable impact on the production, and likely the resulting density, of the Moon's neutral gas envelope and the torus formed along its orbit.

This effect is particularly visible in the total O_2 production rates (rightmost blocks of Figures 12a and 12b), which differ drastically based upon the assumed thickness of the surface O_2 -bearing layer. For all five temperature profiles shown, the production rate calculated with a thick layer is nearly two orders of magnitude greater than that calculated with a thin layer. Depending upon the temperature profile used, the total O_2 production rate for a thin layer ranges from $P_T = (1.5 \times 10^{26} - 4.9 \times 10^{26}) \text{ s}^{-1}$, while the thick layer estimate ranges from $P_T = (8.1 \times 10^{27} - 2.1 \times 10^{28}) \text{ s}^{-1}$. Our modeled production rate for a thin layer agrees well with published estimates of the global

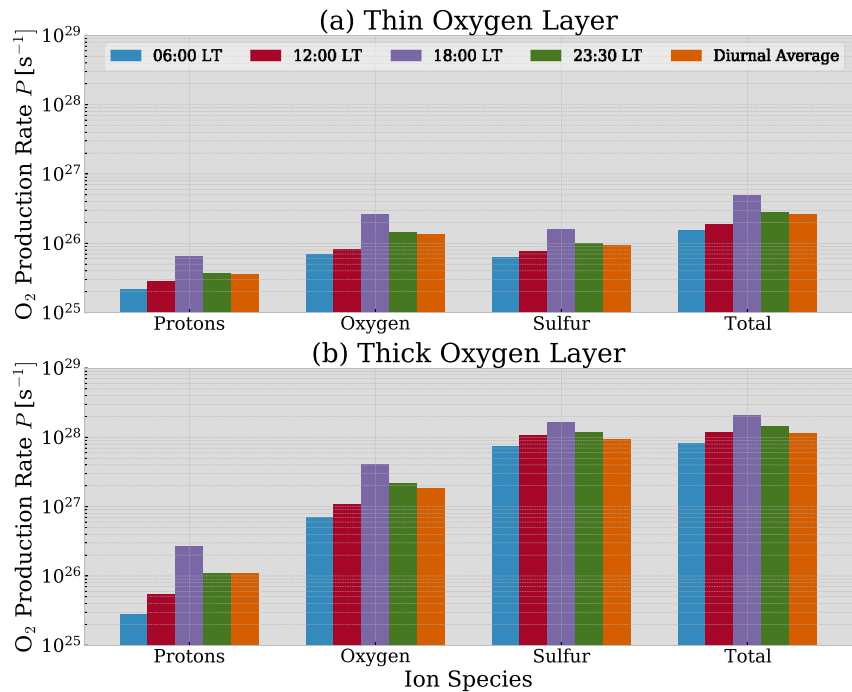


Figure 12. O_2 production rates from impinging magnetospheric protons, oxygen ions, sulfur ions, and all species combined at all energies, calculated with a thin layer model (a), and a thick layer model (b) of the oxygen concentration within Europa's surface. The different colors denote different orbital positions: 06:00 LT (blue), 12:00 LT (red), 18:00 LT (purple), and 23:30 LT (green). Rates calculated with a diurnally averaged temperature profile are shown in orange. The production rates of H_2 are exactly twice those of O_2 (see Equation 4).

neutral *escape* rate at Europa of $\approx 1 \times 10^{26} \text{ s}^{-1}$ (Vorburger & Wurz, 2018) and $\approx 2.7 \times 10^{26} \text{ s}^{-1}$ (Smyth & Marconi, 2006), which must be true for the exosphere to be in hydrostatic equilibrium. Dols et al. (2016) suggested that symmetric charge exchange reactions between picked-up O_2^+ ions and exospheric O_2 neutrals may increase the O_2 escape rate by up to an order of magnitude, arriving at a figure of $P \approx 4 \times 10^{27} \text{ s}^{-1}$. This value edges slightly closer to our thick layer estimate.

Cassidy et al. (2013) reported a global O_2 production rate of $P_T = 1.0 \times 10^{26} \text{ s}^{-1}$ using uniform electromagnetic fields and the same thin oxygen layer model applied here. Thus, the combination of the field perturbations (which reduce the surface flux) and the actual incidence angles (which enhance the sputtering yields) in our model results in a similar estimate of P as a model setup that treats the fields as uniform and assumes a constant incidence angle of $\theta = 0^\circ$ (Cassidy et al., 2013). When the field perturbations are included, the chosen treatment of the incidence angles does not substantially alter the *spatial distribution* of the sputtering rates. However, assuming normal incidence does reduce the rates to their minimum possible values at all surface locations (see also second vs. third column of Figure 6). Therefore, if our model was to utilize a constant incidence angle of $\theta = 0^\circ$ for all impinging ions, our estimate of the total O_2 production rate would fall below that of Cassidy et al. (2013), due to the shielding effect of the electromagnetic field perturbations. Regardless of the integrated production rates, using uniform electromagnetic fields (Cassidy et al., 2013) leads to vastly different estimates as to where the most exospheric material is being ejected compared to perturbed fields. In other words, careful treatment of Europa's perturbed electromagnetic environment is mandatory to constrain, for example, the location and extent of large-scale inhomogeneities in the Moon's exosphere. Precise knowledge on the properties of such exospheric inhomogeneities is critical for the ongoing search for transient water vapor plumes in plasma and magnetic field data (Arnold et al., 2019; Jia et al., 2018).

For both a thick and a thin oxygen-bearing layer the total production rate is affected by less than a factor of 5 when the surface temperature profile is altered (rightmost blocks of Figures 12a and 12b). In both cases, the O_2 production maximizes at 18:00 LT, when the surface temperature reaches its maximum and the sub-plasma point coincides with the sub-solar point. The minimum production rate occurs at 06:00 LT for both sputtering yield models,

since the surface is at its coolest and the dayside hemisphere is downstream (i.e., it is only weakly irradiated). For either model of the O₂-bearing surface layer thickness, the production rate at 18:00 LT exceeds that at 06:00 LT by a factor of ~3. Therefore, while the assumption of a thick O₂-bearing layer markedly increases the O₂ source rate compared to a thin layer, both assumptions result in a similar dependence of P on Europa's orbital position.

Sputtered O₂ remains in Europa's exosphere for only a finite residence time before it is lost due to ionization or Jeans escape into the neutral torus (Smith et al., 2019). The average residence time of sputtered O₂ in Europa's exosphere ($\approx 1.4 \times 10^5$ s, Smyth and Marconi (2006)) allows for an estimation of the globally averaged O₂ column density, namely by multiplying the production rate P with the residence time and dividing by Europa's surface area $4\pi R_E^2$. Using this method we estimate an O₂ column density of $(6.9 \times 10^{13} - 2.2 \times 10^{14})$ cm⁻² in a thin layer model, and $(7.6 \times 10^{15} - 1.9 \times 10^{16})$ cm⁻² for a thick layer. HST observations have assessed the column density of Europa's exosphere to be $(2 \times 10^{14} - 6 \times 10^{14})$ cm⁻² (Hall et al., 1998; Roth et al., 2016; Saur et al., 2011). Thus, our model indicates that a thick oxygen layer approach to O₂ sputtering overestimates the observed O₂ content of Europa's exosphere, whereas a thin oxygen layer approach is consistent with the observed exospheric column densities.

Since the sputtering yields (and resultant rates) of H₂ are exactly twice those of O₂ (Equation 4), the spatial distribution of the H₂ sputtering rates is the same as that of O₂, regardless of the surface layer thickness. The production rates of H₂ in a thin layer approach range from $P_T = (3.0 \times 10^{26} - 9.8 \times 10^{26})$ s⁻¹, depending upon the local time, while those in a thick layer approach vary from $P_T = (1.6 \times 10^{28} - 6.3 \times 10^{28})$ s⁻¹. Again combining our modeled production rates with the exospheric residence time of H₂ (1.2×10^4 s, Smyth & Marconi, 2006), we estimate an H₂ column density of $(2.9 \times 10^{12} - 9.6 \times 10^{12})$ cm⁻² with a thin layer, and $(1.6 \times 10^{14} - 3.9 \times 10^{14})$ cm⁻² with a thick layer. Although the column density of molecular hydrogen in Europa's exosphere has not yet been constrained through observations, our estimated H₂ column density calculated with a thin layer is in good agreement with exospheric modeling by Vorbürger and Würz (2018). These authors calculated a value of $\approx 2.0 \times 10^{12}$ cm⁻².

4. Summary and Concluding Remarks

In this study, we have presented the first model of magnetospheric ion sputtering at Europa which takes into account the perturbations to the electromagnetic fields near the Moon. To accomplish this, we have combined the electromagnetic fields from the AIKEF hybrid model (Addison et al., 2021; Arnold et al., 2019; Arnold, Liuzzo, & Simon, 2020; Arnold, Simon, & Liuzzo, 2020; Breer et al., 2019) with a variant of the GENTOO particle tracing model (Addison et al., 2021; Breer et al., 2019; Liuzzo et al., 2019a, 2019b, 2020) which has been expanded to calculate the contribution of impinging magnetospheric ions to surface sputtering. We have calculated maps of the sputtering rates of H₂O, O₂, and H₂, the major exospheric constituents at Europa (e.g., Roth, 2021; Roth et al., 2016; Vorbürger & Würz, 2018) from the three dominant ion species in the Moon's magnetospheric environment. To constrain the variations in the surface sputtering rate with solar orientation (European local time), we have examined the temperature-dependent O₂ and H₂ sputtering rates at four (near) equally spaced locations of Europa along its orbit, as well as with a diurnally averaged temperature profile. In addition, we have investigated how the thickness of the O₂-bearing layer within Europa's surface (Plainaki et al., 2013; Teolis et al., 2017) affects the spatial distribution of the sputtering rates. Finally, we have calculated the total H₂O, O₂, and H₂ production rates at Europa, as well as estimations of the corresponding exospheric O₂ column densities, which agree well with observations by HST and the Galileo spacecraft.

Our major results are as follows:

1. The inclusion of the electromagnetic field perturbations near Europa substantially modifies the spatial distribution of H₂O sputtering rates across the surface. Compared to a uniform field model, the deflection of the impinging ions by the draped fields reduces the sputtering rate by up to two orders of magnitude across much of the upstream hemisphere. Furthermore, substantial amounts of H₂O, O₂, and H₂ are sputtered from the downstream hemisphere when the field perturbations are taken into account, in contrast to a uniform field model which predicts zero sputtering in this region (Cassidy et al., 2013). Therefore, while a uniform field model would require redistribution of the sputtered gas in order to explain any substantial column density above the downstream hemisphere, deflection of the projectile ions by the perturbed fields allows for the direct generation of exospheric neutrals in this region. Thus, not only are the field perturbations affected by any asymmetries in Europa's neutral gas envelope (e.g., Arnold et al., 2019), but—due to their influence on

the trajectories of projectile ions—the field perturbations in turn play a key role in determining where such “bulges” in the Moon’s exosphere are located.

2. The spatial distribution of the temperature-dependent O₂ and H₂ sputtering rates is largely determined by the thickness of the oxygen-bearing layer within Europa’s surface. If the oxygen-bearing layer is thin compared to the penetration depths of energetic ions, thermal ions dominate the O₂ and H₂ sputtering rates everywhere except low latitudes on the downstream hemisphere. Thus, the highest sputtering rates with a thin layer are persistently located near Europa’s upstream apex, regardless of the Moon’s orbital position. However, if the oxygen-bearing surface layer is thick, the sputtering efficiency of energetic ions does not decrease with penetration depth, and energetic ions make the greatest contribution to the sputtering rate. The spatial distribution of the energetic ion sputtering rate is then determined almost exclusively by the surface temperature profile. Hence, with a thick oxygen-bearing layer the region of maximum O₂ and H₂ sputtering follows the sub-solar point as Europa orbits Jupiter. Therefore, depending on the Moon’s orbital position, two enhancements in the sputtering rates may be present if the O₂-bearing surface layer is thick: one located near the sub-solar point (which moves along Europa’s equator as the Moon orbits Jupiter), and a persistent, weaker enhancement near the upstream apex.
3. The total production rates of O₂ and H₂ vary as a function of Europa’s orbital position. The O₂ production rate maximizes at 18:00 LT, when the Sun is illuminating the Moon’s low-albedo, upstream hemisphere. The O₂ production rate minimizes at 06:00 LT, when the dayside hemisphere is located on the Moon’s brighter, downstream face. Regardless of the thickness of the oxygen-bearing surface layer, the production rate at 18:00 LT exceeds that at 06:00 LT by a factor of ~3.
4. Assuming the oxygen-bearing surface layer to be thin compared to the penetration depth of energetic ions reproduces the values of Europa’s exospheric column density, as observed by HST and the Galileo spacecraft. However, our estimated column densities do not take into account the redistribution of newly sputtered molecules due to, for example, gravitational and fictitious forces, nor the contribution of magnetospheric electrons to surface erosion.
5. The preferential ejection of H₂O molecules from a narrow region near the upstream apex, as revealed by our model, correlates well with the recent detection of a localized, persistent H₂O exosphere above Europa’s upstream apex by Roth (2021) using HST observations. In addition, particularly intense weathering of the upstream hemisphere in a quasi-ellipse centered near the upstream apex (see Section 3.2) matches the low concentrations of H₂O ice observed in that region by the Earth-based *Very Large Telescope* (Ligier et al., 2016).

The analytical exosphere model used in AIKEF to determine the field perturbations near Europa includes a upstream-downstream asymmetry (see Section 2.1; e.g., Addison et al., 2021). The upstream “bulge” in this model exosphere has a clearly discernible impact on the field perturbations near the Moon (Arnold et al., 2019). However, our results for the sputtering rates suggest that the draped fields themselves play a critical role in determining the regions on Europa’s surface that are exposed to particularly intense erosion by magnetospheric ions. To achieve self-consistency, it would therefore be necessary to develop an improved exosphere model based on our calculated maps of the sputtering rates, subsequently use AIKEF to assess the influence of this modified neutral gas envelope on the electromagnetic fields, and then again update the ion surface fluxes and sputtering rates with GENTOO. This cycle would have to be repeated until convergence is achieved. However, such an exhaustive modeling effort is beyond the scope of the present study. In addition, our model has not considered the contribution of magnetospheric electrons to surface sputtering, which was recently suggested to be equal to, or even exceed, that of the ions (Davis et al., 2021; Vorburger & Wurz, 2018). Modeling of electron surface bombardment requires treatment of the bounce motion of electrons between Europa’s local interaction region and Jupiter’s polar ionosphere (Paranicas et al., 2009), as well as inclusion of relativistic mass growth of the electrons. This effort will be the subject of a future publication.

Data Availability Statement

Results from both the AIKEF hybrid model and the GENTOO particle-tracing model can be downloaded at <https://doi.org/10.5281/zenodo.5708206>.

Acknowledgments

The authors are grateful to the NASA Solar System Workings 2018 Program (Grant No. #80NSSC20K0463) for financial support. The authors would also like to thank both referees for careful inspection of the manuscript and for valuable comments.

References

- Addison, P., Liuzzo, L., Arnold, H., & Simon, S. (2021). Influence of Europa's time-varying electromagnetic environment on magnetospheric ion precipitation and surface weathering. *Journal of Geophysical Research: Space Physics*, *126*(5), e2020JA029087. <https://doi.org/10.1029/2020JA029087>
- Arnold, H., Liuzzo, L., & Simon, S. (2019). Magnetic signatures of a plume at Europa during the Galileo E26 flyby. *Geophysical Research Letters*, *46*(3), 1149–1157. <https://doi.org/10.1029/2018GL081544>
- Arnold, H., Liuzzo, L., & Simon, S. (2020). Plasma interaction signatures of plumes at Europa. *Journal of Geophysical Research: Space Physics*, *125*(1), e2019JA027346. <https://doi.org/10.1029/2019JA027346>
- Arnold, H., Simon, S., & Liuzzo, L. (2020). Applying ion energy spectrograms to search for plumes at Europa. *Journal of Geophysical Research: Space Physics*, *125*, e2020JA028376. <https://doi.org/10.1029/2020JA028376>
- Bagenal, F., & Delamere, P. A. (2011). Flow of mass and energy in the magnetospheres of Jupiter and Saturn. *Journal of Geophysical Research: Space Physics*, *116*, A05209. <https://doi.org/10.1029/2010JA016294>
- Bagenal, F., & Dols, V. (2020). The space environment of Io and Europa. *Journal of Geophysical Research: Space Physics*, *125*(5), e27485. <https://doi.org/10.1029/2019JA027485>
- Bagenal, F., Sidrow, E., Wilson, R. J., Cassidy, T. A., Dols, V., Cray, F. J., et al. (2015). Plasma conditions at Europa's orbit. *Icarus*, *261*, 1–13. <https://doi.org/10.1016/j.icarus.2015.07.036>
- Bagenal, F., Wilson, R. J., Siler, S., Paterson, W. R., & Kurth, W. S. (2016). Survey of Galileo plasma observations in Jupiter's plasma sheet. *Journal of Geophysical Research: Planets*, *121*(5), 871–894. <https://doi.org/10.1002/2016JE005009>
- Baragiola, R., Vidal, R., Svendsen, W., Schou, J., Shi, M., Bahr, D., et al. (2003). Sputtering of water ice (Fifth International Symposium on Swift Heavy Ions in Matter). *Nuclear Instruments and Methods in Physics Research Section B: Beam Interactions with Materials and Atoms*, *209*, 294–303. [https://doi.org/10.1016/S0168-583X\(02\)02052-9](https://doi.org/10.1016/S0168-583X(02)02052-9)
- Bar-Nun, A., Herman, G., Rappaport, M. L., & Mekler, Y. (1985). Ejection of H₂O, O₂, H₂ and H from water ice by 0.5–6 keV H⁺ and Ne⁺ ion bombardment. *Surface Science*, *150*(1), 143–156. [https://doi.org/10.1016/0039-6028\(85\)90215-8](https://doi.org/10.1016/0039-6028(85)90215-8)
- Bierhaus, E. B., Zahnle, K., & Chapman, C. R. (2009). Europa's crater distributions and surface ages. In R. T. Pappalardo, W. B. McKinnon, & K. K. Khurana (Eds.), *Europa* (pp. 161–180). University of Arizona Press.
- Breer, B. R., Liuzzo, L., Arnold, H., Andersson, P. N., & Simon, S. (2019). Energetic ion dynamics in the perturbed electromagnetic fields near Europa. *Journal of Geophysical Research*, *124*, 7592–7613. <https://doi.org/10.1029/2019JA027147>
- Brown, W. L., Augustyniak, W. M., Simmons, E., Marcantonio, K. J., Lanzerotti, L. J., Johnson, R. E., et al. (1982). Erosion and molecule formation in condensed gas films by electronic energy loss of fast ions. *Nuclear Instruments and Methods in Physics Research*, *198*(1), 1–8. [https://doi.org/10.1016/0167-5087\(82\)90043-6](https://doi.org/10.1016/0167-5087(82)90043-6)
- Brown, W. L., Lanzerotti, L. J., Poate, J. M., & Augustyniak, W. M. (1978). "Sputtering" of ice by MeV light ions. *Physical Review Letters*, *40*, 1027–1030. <https://doi.org/10.1103/PhysRevLett.40.1027>
- Carlson, R. W., Anderson, M. S., Mehlman, R., & Johnson, R. E. (2005). Distribution of hydrate on Europa: Further evidence for sulfuric acid hydrate. *Icarus*, *177*(2), 461–471. <https://doi.org/10.1016/j.icarus.2005.03.026>
- Carlson, R. W., Calvin, W. M., Dalton, J. B., Hansen, G. B., Hudson, R. L., Johnson, R. E., et al. (2009). Europa's surface composition. In R. T. Pappalardo, W. B. McKinnon, & K. K. Khurana (Eds.), *Europa* (pp. 283). University of Arizona Press.
- Carnielli, G., Galand, M., Leblanc, F., Modolo, R., Beth, A., & Jia, X. (2020). Simulations of ion sputtering at Ganymede. *Icarus*, *351*, 113918. <https://doi.org/10.1016/j.icarus.2020.113918>
- Cassidy, T., Coll, P., Raulin, F., Carlson, R. W., Johnson, R. E., Loeffler, M. J., et al. (2010). Radiolysis and photolysis of icy satellite surfaces: Experiments and theory. *Space Science Reviews*, *153*(1–4), 299–315. <https://doi.org/10.1007/s11214-009-9625-3>
- Cassidy, T., & Johnson, R. (2005). Monte Carlo model of sputtering and other ejection processes within a regolith. *Icarus*, *176*(2), 499–507. <https://doi.org/10.1016/j.icarus.2005.02.013>
- Cassidy, T., Johnson, R. E., Geissler, P. E., & Leblanc, F. (2008). Simulation of Na D emission near Europa during eclipse. *Journal of Geophysical Research: Planets*, *113*(E2). <https://doi.org/10.1029/2007JE002955>
- Cassidy, T., Paranicas, C., Shirley, J., Dalton, J., III, Teolis, B., Johnson, R., et al. (2013). Magnetospheric ion sputtering and water ice grain size at Europa (Surfaces, atmospheres and magnetospheres of the outer planets and their satellites and ring systems: Part VIII). *Planetary and Space Science*, *77*, 64–73. <https://doi.org/10.1016/j.pss.2012.07.008>
- Clark, G., Mauk, B. H., Kollmann, P., Paranicas, C., Bagenal, F., Allen, R. C., et al. (2020). Heavy ion charge states in Jupiter's polar magnetosphere inferred from auroral megavolt electric potentials. *Journal of Geophysical Research: Space Physics*, *125*, e2020JA028052. <https://doi.org/10.1029/2020JA028052>
- Cooper, J. F., Johnson, R. E., Mauk, B. H., Garrett, H. B., & Gehrels, N. (2001). Energetic ion and electron irradiation of the icy Galilean satellites. *Icarus*, *149*(1), 133–159. <https://doi.org/10.1006/icar.2000.6498>
- Coustenis, A., Tokano, T., Burger, M. H., Cassidy, T. A., Lopes, R. M., Lorenz, R. D., et al. (2010). Atmospheric/exospheric characteristics of icy satellites. *Space Science Reviews*, *153*(1–4), 155–184. <https://doi.org/10.1007/s11214-009-9615-5>
- Dalton, J. B., Cassidy, T., Paranicas, C., Shirley, J. H., Prockter, L. M., & Kamp, L. W. (2013). Exogenic controls on sulfuric acid hydrate production at the surface of Europa. *Planetary and Space Science*, *77*, 45–63. <https://doi.org/10.1016/j.pss.2012.05.013>
- Davis, M. R., Meier, R. M., Cooper, J. F., & Loeffler, M. J. (2021). The contribution of electrons to the sputter-produced O₂ exosphere on Europa. *The Astrophysical Journal*, *908*(2), L53. <https://doi.org/10.3847/2041-8213/abe415>
- Dols, V. J., Bagenal, F., Cassidy, T. A., Cray, F. J., & Delamere, P. A. (2016). Europa's atmospheric neutral escape: Importance of symmetrical O₂ charge exchange. *Icarus*, *264*, 387–397. <https://doi.org/10.1016/j.icarus.2015.09.026>
- Eviatar, A., Bar-Nun, A., & Podolak, M. (1985). European surface phenomena. *Icarus*, *61*(2), 185–191. [https://doi.org/10.1016/0019-1035\(85\)90100-9](https://doi.org/10.1016/0019-1035(85)90100-9)
- Famá, M., Shi, J., & Baragiola, R. (2008). Sputtering of ice by low-energy ions. *Surface Science*, *602*(1), 156–161. <https://doi.org/10.1016/j.susc.2007.10.002>
- Feyerabend, M., Simon, S., Motschmann, U., & Liuzzo, L. (2015). Filamented ion tail structures at Titan: A hybrid simulation study. *Planetary and Space Science*, *117*, 362–376. <https://doi.org/10.1016/j.pss.2015.07.008>
- Feyerabend, M., Simon, S., Neubauer, F. M., Motschmann, U., Bertucci, C., Edberg, N. J. T., et al. (2016). Hybrid simulation of Titan's interaction with the supersonic solar wind during Cassini's T96 flyby. *Geophysical Research Letters*, *43*(1), 35–42. <https://doi.org/10.1002/2015GL066848>
- Gibbs, K. M., Brown, W. L., & Johnson, R. E. (1988). Electronic sputtering of condensed O₂. *Physical Review B: Condensed Matter*, *38*, 11001–11007. <https://doi.org/10.1103/PhysRevB.38.11001>
- Hall, D. T., Feldman, P. D., McGrath, M. A., & Strobel, D. F. (1998). The far-ultraviolet oxygen airglow of Europa and Ganymede. *The Astrophysical Journal*, *499*(1), 475–481. <https://doi.org/10.1086/305604>

- Hall, D. T., Strobel, D. F., Feldman, P. D., McGrath, M. A., & Weaver, H. A. (1995). Detection of an oxygen atmosphere on Jupiter's Moon Europa. *Nature*, 373(6516), 677–679. <https://doi.org/10.1038/373677a0>
- Harris, C. D. K., Jia, X., Slavin, J. A., Toth, G., Huang, Z., & Rubin, M. (2021). Multi-fluid MHD simulations of Europa's plasma interaction under different magnetospheric conditions. *Journal of Geophysical Research: Space Physics*, 126(5), e2020JA028888. <https://doi.org/10.1029/2020JA028888>
- Hendrix, A. R., Cassidy, T. A., Johnson, R. E., Paranicas, C., & Carlson, R. W. (2011). Europa's disk-resolved ultraviolet spectra: Relationships with plasma flux and surface terrains. *Icarus*, 212(2), 736–743. <https://doi.org/10.1016/j.icarus.2011.01.023>
- Hill, T. W., & Michel, F. C. (1976). Heavy ions from the Galilean satellites and the centrifugal distortion of the Jovian magnetosphere. *Journal of Geophysical Research*, 81(25), 4561–4565. <https://doi.org/10.1029/JA081i025p04561>
- Huybrighs, H. L. F., Roussos, E., Blöcker, A., Krupp, N., Futaana, Y., Barabash, S., et al. (2020). An active plume eruption on Europa during Galileo flyby E26 as indicated by energetic proton depletions. *Geophysical Research Letters*, 47(10), e2020GL087806. <https://doi.org/10.1029/2020GL087806>
- Jia, X., Kivelson, M. G., Khurana, K. K., & Kurth, W. S. (2018). Evidence of a plume on Europa from Galileo magnetic and plasma wave signatures. *Nature Astronomy*, 2(6), 459–464. <https://doi.org/10.1038/s41550-018-0450-z>
- Johnson, R. E. (1996). Sputtering of ices in the outer solar system. *Reviews of Modern Physics*, 68(1), 305–312. <https://doi.org/10.1103/RevModPhys.68.305>
- Johnson, R. E., Burger, M. H., Cassidy, T. A., Leblanc, F., Marconi, M., & Smyth, W. H. (2009). Composition and detection of Europa's sputter-induced atmosphere. In R. T. Pappalardo, W. B. McKinnon, & K. K. Khurana (Eds.), *Europa* (p. 507). University of Arizona Press.
- Johnson, R. E., Carlson, R. W., Cooper, J. F., Paranicas, C., Moore, M. H., & Wong, M. C. (2004). Radiation effects on the surfaces of the Galilean satellites. In F. Bagenal, T. E. Dowling, & W. B. McKinnon (Eds.), *Jupiter: The planet, satellites and magnetosphere* (Vol. 1, pp. 485–512). Cambridge University Press.
- Johnson, R. E., Cooper, P. D., Quickenden, T. I., Grieves, G. A., & Orlando, T. M. (2005). Production of oxygen by electronically induced dissociations in ice. *Journal of Chemical Physics*, 123(18), 184715. <https://doi.org/10.1063/1.2107447>
- Kabin, K., Combi, M. R., Gombosi, T. I., Nagy, A. F., DeZeeuw, D. L., & Powell, K. G. (1999). On Europa's magnetospheric interaction: A MHD simulation of the E4 flyby. *Journal of Geophysical Research*, 104(A9), 19983–19992. <https://doi.org/10.1029/1999JA900263>
- Kattenhorn, S. A., & Hurford, T. (2009). Tectonics of Europa. In R. T. Pappalardo, W. B. McKinnon, & K. K. Khurana (Eds.), *Europa* (p. 199). University of Arizona Press.
- Khurana, K. K., & Kivelson, M. G. (1993). Inference of the angular velocity of plasma in the Jovian magnetosphere from the sweepback of magnetic field. *Journal of Geophysical Research: Space Physics*, 98(A1), 67–79. <https://doi.org/10.1029/92ja01890>
- Kim, T. K., Ebert, R. W., Valek, P. W., Allegrini, F., McComas, D. J., Bagenal, F., et al. (2020). Survey of ion properties in Jupiter's plasma sheet: Juno JADE-I observations. *Journal of Geophysical Research: Space Physics*, 125(4), e2019JA027696. <https://doi.org/10.1029/2019JA027696>
- Kivelson, M. G., Khurana, K. K., Russell, C. T., Volwerk, M., Walker, R. J., & Zimmer, C. (2000). Galileo magnetometer measurements: A stronger case for a subsurface ocean at Europa. *Science*, 289(5483), 1340–1343. <https://doi.org/10.1126/science.289.5483.1340>
- Kivelson, M. G., Khurana, K. K., Stevenson, D. J., Bennett, L., Joy, S., Russell, C. T., et al. (1999). Europa and Callisto: Induced or intrinsic fields in a periodically varying plasma environment. *Journal of Geophysical Research*, 104(A3), 4609–4625. <https://doi.org/10.1029/1998JA900095>
- Kivelson, M. G., Khurana, K. K., & Volwerk, M. (2009). Europa's interaction with the Jovian magnetosphere. In R. T. Pappalardo, W. B. McKinnon, & K. K. Khurana (Eds.), *Europa* (p. 545). University of Arizona Press.
- Kollmann, P., Paranicas, C., Clark, G., Roussos, E., Lagg, A., & Krupp, N. (2016). The vertical thickness of Jupiter's Europa gas torus from charged particle measurements. *Geophysical Research Letters*, 43(18), 9425–9433. <https://doi.org/10.1002/2016GL070326>
- Krupp, N., Kotova, A., Roussos, E., Simon, S., Liuzzo, L., Paranicas, C., et al. (2020). Magnetospheric interactions of Saturn's Moon Dione (2005–2015). *Journal of Geophysical Research: Space Physics*, 125(6), e2019JA027688. <https://doi.org/10.1029/2019JA027688>
- Lagg, A., Krupp, N., Woch, J., & Williams, D. J. (2003). In-situ observations of a neutral gas torus at Europa. *Geophysical Research Letters*, 30(11), 1556. <https://doi.org/10.1029/2003GL017214>
- Ligier, N., Poulet, F., Carter, J., Brunetto, R., & Gourgeot, F. (2016). VLT/SINFONI observations of Europa: New insights into the surface composition. *The Astrophysical Journal*, 151(6), 163. <https://doi.org/10.3847/0004-6256/151/6/163>
- Liuzzo, L., Feyerabend, M., Simon, S., & Motschmann, U. (2015). The impact of Callisto's atmosphere on its plasma interaction with the Jovian magnetosphere. *Journal of Geophysical Research: Space Physics*, 120(11), 9401–9427. <https://doi.org/10.1002/2015JA021792>
- Liuzzo, L., Paty, C., Cochrane, C., Nordheim, T., Luspay-Kuti, A., Castillo-Rogez, J., et al. (2021). Triton's variable interaction with Neptune's magnetospheric plasma. *Journal of Geophysical Research: Space Physics*, 126(11), e2021JA029740. <https://doi.org/10.1029/2021JA029740>
- Liuzzo, L., Poppe, A. R., Halekas, J. S., Simon, S., & Cao, X. (2021). Investigating the moon's interaction with the terrestrial magnetotail lobe plasma. *Geophysical Research Letters*, 48(9), e2021GL093566. <https://doi.org/10.1029/2021GL093566>
- Liuzzo, L., Poppe, A. R., Paranicas, C., Nénon, Q., Fatemi, S., & Simon, S. (2020). Variability in the energetic electron bombardment of Gany-mede. *Journal of Geophysical Research: Space Physics*, 125, e2020JA028347. <https://doi.org/10.1029/2020JA028347>
- Liuzzo, L., Simon, S., & Feyerabend, M. (2018). Observability of Callisto's inductive signature during the JUPITER ICY moons Explorer mission. *Journal of Geophysical Research: Space Physics*, 123(11), 9045–9054. <https://doi.org/10.1029/2018JA025951>
- Liuzzo, L., Simon, S., Feyerabend, M., & Motschmann, U. (2016). Disentangling plasma interaction and induction signatures at Callisto: The Galileo C10 flyby. *Journal of Geophysical Research: Space Physics*, 121(9), 8677–8694. <https://doi.org/10.1002/2016JA023236>
- Liuzzo, L., Simon, S., Feyerabend, M., & Motschmann, U. (2017). Magnetic signatures of plasma interaction and induction at Callisto: The Galileo C21, C22, C23, and C30 flybys. *Journal of Geophysical Research: Space Physics*, 122(7), 7364–7386. <https://doi.org/10.1002/2017JA024303>
- Liuzzo, L., Simon, S., & Regoli, L. (2019a). Energetic electron dynamics near Callisto. *Planetary and Space Science*, 179, 104726. <https://doi.org/10.1016/j.pss.2019.104726>
- Liuzzo, L., Simon, S., & Regoli, L. (2019b). Energetic ion dynamics near Callisto. *Planetary and Space Science*, 166, 23–53. <https://doi.org/10.1016/j.pss.2018.07.014>
- Mauk, B. H., Mitchell, D. G., McEntire, R. W., Paranicas, C. P., Roelof, E. C., Williams, D. J., et al. (2004). Energetic ion characteristics and neutral gas interactions in Jupiter's magnetosphere. *Journal of Geophysical Research: Space Physics*, 109(A9), e2003JA010270. <https://doi.org/10.1029/2003JA010270>
- McEwen, A. S. (1986). Exogenic and endogenic albedo and color patterns on Europa. *Journal of Geophysical Research: Solid Earth*, 91(B8), 8077–8097. <https://doi.org/10.1029/JB091iB08p08077>
- Müller, J., Simon, S., Motschmann, U., Schüle, J., Glassmeier, K.-H., & Pringle, G. J. (2011). A.I.K.E.F.: Adaptive hybrid model for space plasma simulations. *Computer Physics Communications*, 182(4), 946–966. <https://doi.org/10.1016/j.cpc.2010.12.033>
- Nénon, Q., & André, N. (2019). Evidence of Europa neutral gas torii from energetic sulfur ion measurements. *Geophysical Research Letters*, 46(7), 3599–3606. <https://doi.org/10.1029/2019GL082200>
- Neubauer, F. M. (1980). Nonlinear standing Alfvén wave current system at Io: Theory. *Journal of Geophysical Research*, 85, 1171–1178. <https://doi.org/10.1029/JA085iA03p01171>

- Neubauer, F. M. (1998). The sub-Alfvénic interaction of the Galilean satellites with the Jovian magnetosphere. *Journal of Geophysical Research*, *103*, 19843–19866. <https://doi.org/10.1029/97JE03370>
- Neubauer, F. M. (1999). Alfvén wings and electromagnetic induction in the interiors: Europa and Callisto. *Journal of Geophysical Research*, *104*, 28671–28684. <https://doi.org/10.1029/1999JA900217>
- Nordheim, T. A., Hand, K. P., & Paranicas, C. (2018). Preservation of potential biosignatures in the shallow subsurface of Europa. *Nature Astronomy*, *2*, 673–679. <https://doi.org/10.1038/s41550-018-0499-8>
- Nordheim, T. A., Jasinski, J. M., & Hand, K. P. (2019). Galactic cosmic-ray bombardment of Europa's surface. *The Astrophysical Journal*, *881*(2), L29. <https://doi.org/10.3847/2041-8213/ab3661>
- Oza, A. V., Leblanc, F., Johnson, R. E., Schmidt, C., Leclercq, L., Cassidy, T. A., et al. (2019). Dusk over dawn O₂ asymmetry in Europa's near-surface atmosphere. *Planetary and Space Science*, *167*, 23–32. <https://doi.org/10.1016/j.pss.2019.01.006>
- Paganini, L., Villanueva, G. L., Roth, L., Mandell, A. M., Hurford, T. A., Retherford, K. D., et al. (2020). A measurement of water vapour amid a largely quiescent environment on Europa. *Nature Astronomy*, *4*, 266–272. <https://doi.org/10.1038/s41550-019-0933-6>
- Paranicas, C., Carlson, R. W., & Johnson, R. E. (2001). Electron bombardment of Europa. *Geophysical Research Letters*, *28*(4), 673–676. <https://doi.org/10.1029/2000GL012320>
- Paranicas, C., Cooper, J. F., Garrett, H. B., Johnson, R. E., & Sturmer, S. J. (2009). Europa's radiation environment and its effects on the surface. In R. T. Pappalardo, W. B. McKinnon, & K. K. Khurana (Eds.), *Europa* (p. 529). University of Arizona Press.
- Paranicas, C., Mauk, B. H., Khurana, K., Jun, I., Garrett, H., Krupp, N., & Roussos, E. (2007). Europa's near-surface radiation environment. *Geophysical Research Letters*, *34*, L15103. <https://doi.org/10.1029/2007GL030834>
- Paranicas, C., McEntire, R. W., Cheng, A. F., Lagg, A., & Williams, D. J. (2000). Energetic charged particles near Europa. *Journal of Geophysical Research: Space Physics*, *105*(A7), 16005–16015. <https://doi.org/10.1029/1999JA000350>
- Paranicas, C., Ratliff, J. M., Mauk, B. H., Cohen, C., & Johnson, R. E. (2002). The ion environment near Europa and its role in surface energetics. *Geophysical Research Letters*, *29*(5), 181–184. <https://doi.org/10.1029/2001GL014127>
- Paterson, W. R., Frank, L. A., & Ackerson, K. L. (1999). Galileo plasma observations at Europa: Ion energy spectra and moments. *Journal of Geophysical Research: Space Physics*, *104*(A10), 22779–22791. <https://doi.org/10.1029/1999JA900191>
- Pensionerov, I. A., Alexeev, I. I., Belenkaya, E. S., Connerney, J. E. P., & Cowley, S. W. H. (2019). Model of Jupiter's current sheet with a piecewise current density. *Journal of Geophysical Research: Space Physics*, *124*(3), 1843–1854. <https://doi.org/10.1029/2018JA026321>
- Petrik, N. G., Kavetsky, A. G., & Kimmel, G. A. (2006). Electron-stimulated production of molecular oxygen in amorphous solid water on Pt(111): Precursor transport through the hydrogen bonding network. *Journal of Chemical Physics*, *125*(12), 124702. <https://doi.org/10.1063/s1.2345367>
- Plainaki, C., Cassidy, T. A., Shematovich, V. I., Milillo, A., Wurz, P., Vorburger, A., et al. (2018). Towards a global unified model of Europa's tenuous atmosphere. *Space Science Reviews*, *214*(1), 40. <https://doi.org/10.1007/s11214-018-0469-6>
- Plainaki, C., Milillo, A., Massetti, S., Mura, A., Jia, X., Orsini, S., et al. (2015). The H₂O and O₂ exospheres of Ganymede: The result of a complex interaction between the Jovian magnetospheric ions and the icy moon. *Icarus*, *245*, 306–319. <https://doi.org/10.1016/j.icarus.2014.09.018>
- Plainaki, C., Milillo, A., Mura, A., Orsini, S., Massetti, S., & Cassidy, T. A. (2012). The role of sputtering and radiolysis in the generation of Europa exosphere. *Icarus*, *218*, 956–966. <https://doi.org/10.1016/j.icarus.2012.01.023>
- Plainaki, C., Milillo, A., Mura, A., Saur, J., Orsini, S., & Massetti, S. (2013). Exospheric O₂ densities at Europa during different orbital phases (Atmospheres, Magnetospheres and Surfaces of the outer planets, their satellites and ring systems: Part IX). *Planetary and Space Science*, *88*, 42–52. <https://doi.org/10.1016/j.pss.2013.08.011>
- Pospieszalska, M., & Johnson, R. (1989). Magnetospheric ion bombardment profiles of satellites: Europa and Dione. *Icarus*, *78*(1), 1–13. [https://doi.org/10.1016/0019-1035\(89\)90065-1](https://doi.org/10.1016/0019-1035(89)90065-1)
- Rathbun, J. A., Rodriguez, N. J., & Spencer, J. R. (2010). Galileo PPR observations of Europa: Hotspot detection limits and surface thermal properties. *Icarus*, *210*(2), 763–769. <https://doi.org/10.1016/j.icarus.2010.07.017>
- Regoli, L. H., Roussos, E., Feyerabend, M., Jones, G. H., Krupp, N., Coates, A. J., et al. (2016). Access of energetic particles to Titan's exobase: A study of Cassini's T9 flyby. *Planetary and Space Science*, *130*, 40–53. <https://doi.org/10.1016/j.pss.2015.11.013>
- Roth, L. (2021). A stable H₂O atmosphere on Europa's trailing hemisphere from HST images. *Geophysical Research Letters*, *48*(20), e2021GL094289. <https://doi.org/10.1029/2021GL094289>
- Roth, L., Retherford, K. D., Ivchenko, N., Schlatter, N., Strobel, D. F., Becker, T. M., et al. (2017). Detection of a hydrogen corona in HST Ly α images of Europa in transit of Jupiter. *The Astrophysical Journal*, *153*(2), 67. <https://doi.org/10.3847/1538-3881/153/2/67>
- Roth, L., Retherford, K. D., Saur, J., Strobel, D. F., Feldman, P. D., McGrath, M. A., et al. (2014). Orbital apocenter is not a sufficient condition for HST/STIS detection of Europa's water vapor aurora. *Proceedings of the National Academy of Sciences of the United States of America*, *111*(48), E5123–E5132. <https://doi.org/10.1073/pnas.1416671111>
- Roth, L., Saur, J., Retherford, K. D., Strobel, D. F., Feldman, P. D., McGrath, M. A., et al. (2016). Europa's far ultraviolet oxygen aurora from a comprehensive set of HST observations. *Journal of Geophysical Research: Space Physics*, *121*(3), 2143–2170. <https://doi.org/10.1002/2015JA022073>
- Rubin, M., Jia, X., Altwegg, K., Combi, M. R., Daldorff, L. K. S., Gombosi, T. I., et al. (2015). Self-consistent multifluid MHD simulations of Europa's exospheric interaction with Jupiter's magnetosphere. *Journal of Geophysical Research: Space Physics*, *120*(5), 3503–3524. <https://doi.org/10.1002/2015JA021149>
- Saur, J., Feldman, P., Roth, L., Nimmo, F., Strobel, D., Retherford, K., et al. (2011). Hubble space telescope/advanced camera for surveys observations of Europa's atmospheric ultraviolet emission at eastern elongation. *Acta Pathologica Japonica*, *738*, 153. <https://doi.org/10.1088/0004-637X/738/2/153>
- Saur, J., Strobel, D. F., & Neubauer, F. M. (1998). Interaction of the Jovian magnetosphere with Europa: Constraints on the neutral atmosphere. *Journal of Geophysical Research: Planets*, *103*(E9), 19947–19962. <https://doi.org/10.1029/97JE03556>
- Saur, J., Strobel, D. F., Neubauer, F. M., & Summers, M. E. (2003). The ion mass loading rate at Io. *Icarus*, *163*(2), 456–468. [https://doi.org/10.1016/S0019-1035\(03\)00085-X](https://doi.org/10.1016/S0019-1035(03)00085-X)
- Schenk, P. M., Chapman, C. R., Zahnle, K., & Moore, J. M. (2004). Ages and interiors: The cratering record of the Galilean satellites. In F. Bagnal, T. E. Dowling, & W. B. McKinnon (Eds.), *Jupiter: The planet, satellites, and magnetosphere* (pp. 427–456). Cambridge University Press.
- Schilling, N., Neubauer, F. M., & Saur, J. (2007). Time-varying interaction of Europa with the Jovian magnetosphere: Constraints on the conductivity of Europa's subsurface ocean. *Icarus*, *192*(1), 41–55. <https://doi.org/10.1016/j.icarus.2007.06.024>
- Seufert, M., Saur, J., & Neubauer, F. M. (2011). Multi-frequency electromagnetic sounding of the Galilean moons. *Icarus*, *214*(2), 477–494. <https://doi.org/10.1016/j.icarus.2011.03.017>
- Shematovich, V. I., Johnson, R. E., Cooper, J. F., & Wong, M. C. (2005). Surface-bounded atmosphere of Europa. *Icarus*, *173*(2), 480–498. <https://doi.org/10.1016/j.icarus.2004.08.013>

- Sieger, M. T., Simpson, W. C., & Orlando, T. M. (1998). Production of O₂ on icy satellites by electronic excitation of low-temperature water ice. *Nature*, 394(6693), 554–556. <https://doi.org/10.1038/29015>
- Sigmund, P. (1969). Theory of sputtering. I. Sputtering yield of amorphous and polycrystalline targets. *Physical Review*, 184, 383–416. <https://doi.org/10.1103/PhysRev.184.383>
- Simon, S., Addison, P., & Liuzzo, L. (2022). Formation of a displaced plasma wake at Neptune's moon Triton. *Journal of Geophysical Research: Space Physics*, 127(1), e2021JA029958. <https://doi.org/10.1029/2021JA029958>
- Simon, S., Kriegel, H., Saur, J., Wennmacher, A., Neubauer, F. M., Roussos, E., et al. (2012). Analysis of Cassini magnetic field observations over the poles of Rhea. *Journal of Geophysical Research: Space Physics*, 117(A7). <https://doi.org/10.1029/2012JA017747>
- Simon, S., Liuzzo, L., & Addison, P. (2021). Role of the ionospheric conductance profile in sub-Alfvénic Moon-magnetosphere interactions: An analytical model. *Journal of Geophysical Research: Space Physics*, 126(7), e2021JA029191. <https://doi.org/10.1029/2021JA029191>
- Simon, S., Saur, J., Neubauer, F., Motschmann, U., & Dougherty, M. (2009). Plasma wake of Tethys: Hybrid simulations versus Cassini MAG data. *Geophysical Research Letters*, 36(4), L04108. <https://doi.org/10.1029/2008GL036943>
- Smith, H. T., Mitchell, D. G., Johnson, R. E., Mauk, B. H., & Smith, J. E. (2019). Europa neutral torus confirmation and characterization based on observations and modeling. *The Astrophysical Journal*, 871(1), 69. <https://doi.org/10.3847/1538-4357/aad38>
- Smyth, W. H., & Marconi, M. L. (2006). Europa's atmosphere, gas tori, and magnetospheric implications. *Icarus*, 181(2), 510–526. <https://doi.org/10.1016/j.icarus.2005.10.019>
- Spencer, J. R., Lebofsky, L. A., & Sykes, M. V. (1989). Systematic biases in radiometric diameter determinations. *Icarus*, 78(2), 337–354. [https://doi.org/10.1016/0019-1035\(89\)90182-6](https://doi.org/10.1016/0019-1035(89)90182-6)
- Spencer, J. R., Tamppari, L. K., Martin, T. Z., & Travis, L. D. (1999). Temperatures on Europa from Galileo photopolarimeter-radiometer: Night-time thermal anomalies. *Science*, 284, 1514–1516. <https://doi.org/10.1126/science.284.5419.1514>
- Teolis, B. D., Jones, G. H., Miles, P. F., Tokar, R. L., Magee, B. A., Waite, J. H., et al. (2010). Cassini finds an oxygen-carbon dioxide atmosphere at Saturn's icy moon Rhea. *Science*, 330(6012), 1813–1815. <https://doi.org/10.1126/science.1198366>
- Teolis, B. D., Plainaki, C., Cassidy, T. A., & Raut, U. (2017). Water ice radiolytic O₂, H₂, and H₂O₂ yields for any projectile species, energy, or temperature: A model for icy astrophysical bodies. *Journal of Geophysical Research: Planets*, 122(10), 1996–2012. <https://doi.org/10.1002/2017JE005285>
- Teolis, B. D., Shi, J., & Baragiola, R. A. (2009). Formation, trapping, and ejection of radiolytic O₂ from ion-irradiated water ice studied by sputter depth profiling. *The Journal of Chemical Physics*, 130(13), 134704. <https://doi.org/10.1063/1.3091998>
- Teolis, B. D., Vidal, R. A., Shi, J., & Baragiola, R. A. (2005). Mechanisms of O₂ sputtering from water ice by keV ions. *Physical Review B*, 72(24), 245422. <https://doi.org/10.1103/PhysRevB.72.245422>
- Vance, S., Styczinski, M. J., Bills, B. G., Cochrane, C. J., Soderlund, K. M., Gómez-Pérez, N., et al. (2021). Magnetic induction responses of Jupiter's ocean moons including effects from adiabatic convection. *Journal of Geophysical Research*, 126(2), e06418. <https://doi.org/10.1029/2020JE006418>
- Vidal, R., Teolis, B., & Baragiola, R. (2005). Angular dependence of the sputtering yield of water ice by 100keV proton bombardment. *Surface Science*, 588(1), 1–5. <https://doi.org/10.1016/j.susc.2005.05.007>
- Vorburger, A., & Wurz, P. (2018). Europa's ice-related atmosphere: The sputter contribution. *Icarus*, 311, 135–145. <https://doi.org/10.1016/j.icarus.2018.03.022>
- Wiehle, S., Plaschke, F., Motschmann, U., Glassmeier, K.-H., Auster, H., Angelopoulos, V., et al. (2011). First lunar wake passage of ARTEMIS: Discrimination of wake effects and solar wind fluctuations by 3D hybrid simulations. *Planetary and Space Science*, 59(8), 661–671. <https://doi.org/10.1016/j.pss.2011.01.012>
- Ziegler, J., & Manoyan, J. (1988). The stopping of ions in compounds. *Nuclear Instruments and Methods in Physics Research Section B: Beam Interactions with Materials and Atoms*, 35(3), 215–228. [https://doi.org/10.1016/0168-583X\(88\)90273-X](https://doi.org/10.1016/0168-583X(88)90273-X)
- Zimmer, C., Khurana, K. K., & Kivelson, M. G. (2000). Subsurface oceans on Europa and Callisto: Constraints from Galileo magnetometer observations. *Icarus*, 147(2), 329–347. <https://doi.org/10.1006/icar.2000.6456>